ISSN number 0971 - 9709

The Journal of Indian Geophysical Union

AN OPEN ACCESS BIMONTHLY JOURNAL OF IGU

VOLUME 26, ISSUE 3, MAY 2022

EDITORIAL OFFICE
Indian Geophysical Union, NGRI Campus, Uppal Road, Hyderabad- 500 007
Telephone: 91-4027012739, 27012332; Telefax:+91-04-27171564
Email: jigu1963@gmail.com, website: http://iguonline.in/journal/

The Journal with six issues in a year publishes articles covering
Solid Earth Geosciences; Marine Geosciences; and Atmospheric, Space and Planetary Sciences.

Annual Subscription
Individual Rs -1000/- per issue and Institutional Rs- 5000/- for six issues
Payments should be sent by DD drawn in favour of "The Treasurer, Indian Geophysical Union", payable at Hyderabad,
Money Transfer/NEFT/RTGS (Inter-Bank Transfer), Treasurer, Indian Geophysical Union, State Bank of India, Habsiguda Branch, Habsiguda, Uppal Road, Hyderabad- 500 007
A/C: 52191021424, IFSC Code: SBIN0020087, MICR Code: 500002318, SWIFT Code: SBININBBHO9.
For correspondence, please contact, Hon. Secretary, Indian Geophysical Union, NGRI Campus, Uppal Road, Hyderabad - 500 007, India; Email: igu123@gmail.com; Ph: 040 27012332

ISSN: 0257-7968 (Clarivate Analytics)

ISSN: 0971-9709 (NISCAIR)

Approved as bimonthly ESCI journal by Clarivate Analytics

Cited in Indian Citation Index (ICI), New Delhi

Evaluated by NISCAIR, New Delhi

CONTENTS

Research Articles

J. Ind. Geophys. Union, 26(3) (2022), 165-181

Regional magnetic surveys in part of Delhi Fold Belt, Rajasthan (India) and implications for basement structure and mineralization

S. Bangaru Babu*[1], A.V. Kulkarni[2], M. Lakshmana[3] and Dinesh Gupta[4]

[1,3] Geophysics Division, Geological Survey of India Training Institue, Bandlaguda, Hyderabad, 500068, India
[2]Geophysics Division, Geological Survey of India, Seminary Hills, Nagpur, 440006, India
[4]Ex-Geological Survey of India, Kolkata, 700016, India
*Corresponding author: bangaru_geo@rediffmail.com

ABSTRACT

This paper presents the results of regional ground magnetic surveys carried out over an area of 4200 sq. km in parts of Ajmer and Bhilwara districts, Rajasthan, India. The study area falls in the Obvious Geological Potential (OGP) zone associated with economic mineral deposits of India. The survey was conducted for delineating the extension of various rock sequences within the Proterozoic Delhi Fold Belt (DFB). The survey brought out a strong NE-SW trending magnetic anomaly over the rocks of DFB and a mild anomaly in the northwestern part of the area, which is covered by the thick sediments of the Marwar Basin (MB) basin. The NE-SW trending anomaly in the area could be attributed to the exposed/near-surface Archaean basement that has come closer to the surface as a result of Delhi Fold Belt (DFB) tectonics. The anomaly trend brought out the clear picture of the magnetic basement within the Bhilwara Supergroup and their sub-surface structures and associated mineralization, if any. The qualitative analysis of the magnetic data delineated the contact of the significant litho units (Marwar Basin and Delhi Fold Belt). The Euler depth solutions also provided an idea about the magnetic source depths and a cluster of shallow depth solutions have been generated over the Delhi Fold Belt, which may be due to the weak susceptibility of the weathered layer. The amplitude power spectrum has been attempted for estimating the depth interfaces for each selected profile. The average depth to the basement of each profile is estimated as 1.5 km. The contacts between different litho units are also marked. The 2D modeling of a few representative profiles across the DFB reveals that the average magnetic basement depth is about 1.5 km. It is concluded that, the contact zone between Marwar Basin (MB) and Delhi Fold Belt (DFB) is structurally controlled. The results of this study has brought out significant structural features which can form favorable target areas.

Keywords: Magnetic basement, spectrum, Delhi Fold Belt, Euler solutions, Marwar basin, Aravalli craton

INTRODUCTION

The present study area (Figure 1) in South Delhi Fold Belt (SDFB) is located in the northwestern part of the Indian continent, which partly occupies Ajmer and Bhilwara districts of Rajasthan. This region in Rajasthan state comprises litho units ranging from Archaean to Cenozoic age, having a history of multiple deformation and geotectonics. The objective of the present study is to delineate the extensions of the various rock sequences within DFB and its basement interface. Further, attempts have been made to identify the potential areas favorable for mineralization, if any. The survey brought out strong NE-SW trending high magnetic zones in the area which trends along with the primary regional control of mineralization in the Delhi Fold Belt area (Tweto et al., 1968).

The high-resolution gravity surveys in the study area brought significant gravity features, which could be useful in identifying the favorable areas for mineralization (Bangaru Babu et al., 2015). The high gravity zones have been noticed in SW of Agucha Pd-Zn deposit, which delineated the framework of mineralization. The anomalous gold values were noticed near the Kalab-Kalan area from geochemical studies, which is well corroborated with the significant-high gravity zone. A massive sulphide zone with a total strike length of 910 m was identified at Boyo Ki Nandi block from 1090 m depth core drilling, discussed in an unpublished report of the Geological Survey of India. The current geophysical study presents the basement structures below Delhi Fold Belt from magnetic data analysis and the same can be witnessed by different techniques adopted for calculating the average depth of the magnetic interface. The rocks in Sandmata Granulite Gneiss (SGG) of Mangalwar Complex were materialized as tectonic silvers. In the central parts of the Mangalwar Complex, the basement has a number of meta-sedimentary basins (Sinha-Roy, 1995, 1998). In the present study, we provide average depth to the basement interface using magnetic data through different interpretation techniques. Further, boundaries/contacts of different litho units have been marked. These boundaries are indicative of possible faulting, which is favorable for identifying potential target areas for mineral exploration. These major faults have been marked by the interpretation of ground magnetic data.

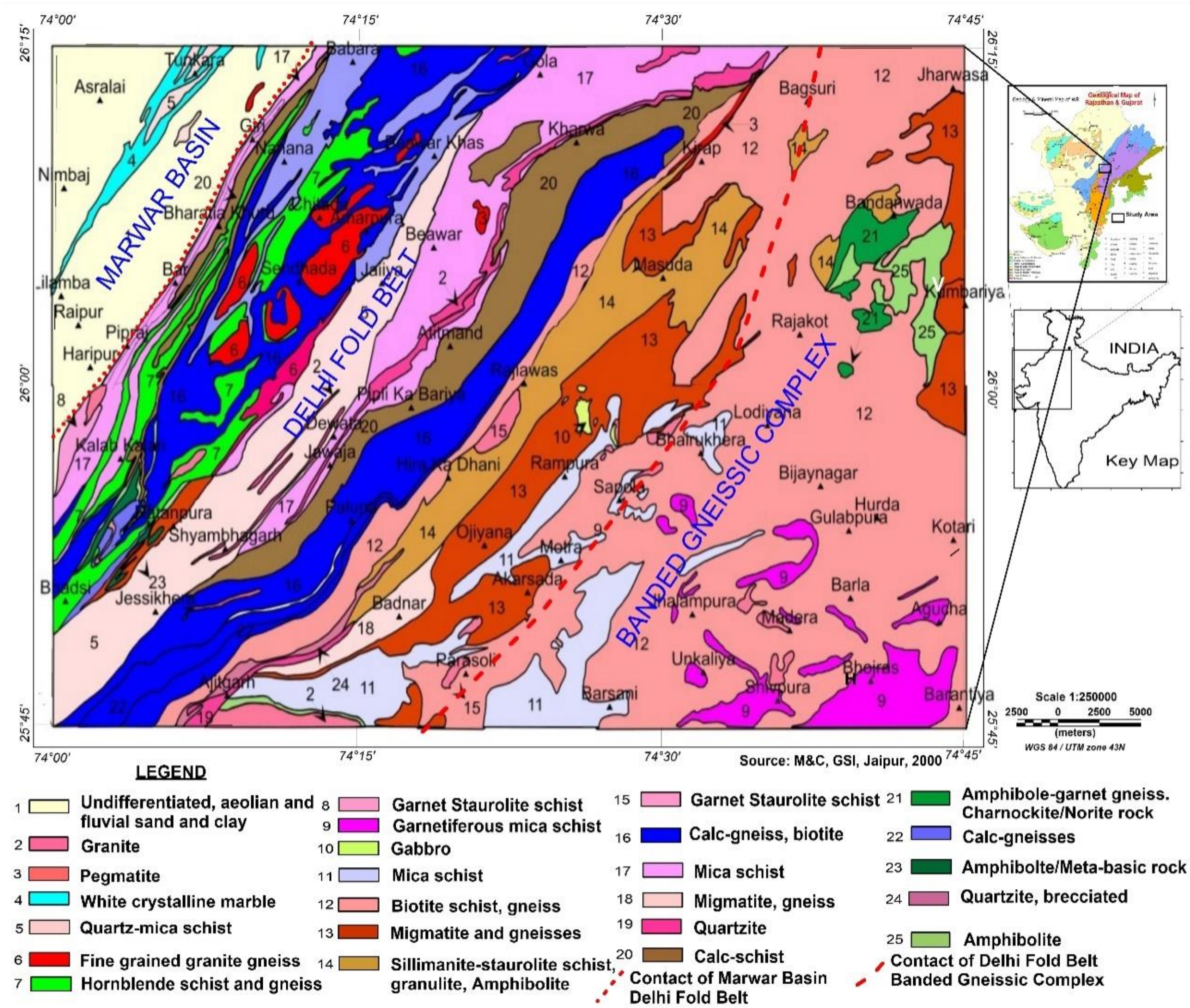

Figure 1. Location of the study area showing regional geology

PREVIOUS STUDIES

The regional gravity surveys conducted in the western Indian shield covering the states of Rajasthan and Gujarat revealed a number of prominent sub-surface regional features which are useful in studying the crustal architecture of the DFB (Reddi and Ramakrishna, 1988). A combined interpretation of deep reflection seismic and gravity data across the Aravali Delhi Fold Belt (ADFB), suggested a thick crust (45-46 km) having a high density (3.04 g/cm^3) domal-shaped body at the lower crustal level (Tiwari et al, 1997, 1998; Mishra et al., 1995, 2000). The high Bouguer gravity anomaly (about 80 mGal) observed between Delhi Fold Belt and Marwar Basin was explained as a deep horst-like feature (Qureshi, 1964). Similarly, the Aravali uplift was also found and associated with the positive isostatic anomalies (Qureshi, 1976). In comparison, the eastern part of DFB is occupied by gravity low due to a westerly dipping (45°) low-density body at the crustal level (Radhakrishna Murthy, 1998). The spectral analysis of ground magnetic data over Delhi Fold Belt (DFB) indicated an average basement depth at 1.5 km. Further, the deep seismic data across the ADFB found a deep penetrating crustal-scale thrust fault with 25 km wide, dipping reflections from the upper crust to a crust-mantle interface (Moho) and a divergent reflection fabric (Vijaya Rao et al., 2000). Magneto-telluric surveys were also conducted across the Nagaur-Kunjer, Rajasthan using the frequency range of 0.01-100 Hz with ~10 km station to station spacing. The geo-electrical structure of the area showed a 10 km thick conductor with an electrical resistivity of 50 ohm-m at a depth of 3 km near Jahazpur, extending up to a depth of about 25 km dipping towards the north-west direction (Gokaran et al., 1995).

GEOLOGY AND TECTONICS

The detailed geological map of the study area is shown in Figure 1. The study area consists of distinct lithological and tectonic units. The 3300-million-year-old Banded Gneissic Complex (BGC), consisting of the Sandmata and Maglawar Complex and Hindoli is the oldest cratonic nucleus of the region. Proterozoic Aravlli and Delhi sediments were deposited successively over this Archean basement (Tewari, et al, 2018 and Saibi et al., 2006).

The basement in the study area contains metamorphosed volcano-sedimentary sequence of Sandmata Complex (SC), Mangalwar Complex (MC) and Hindoli Group (HG) (Gupta, et al.,1997). The Sandmata Complex having the tectonic contact with the MC, covers the high-grade granulite facies rocks. The Rajasthan state located at the NW part of the Indian Craton, comprising different litho units ranging from Archaean to Cenozoic age, has a history of multiple deformation activities and tectonics. The Delhi Supergroup of rocks are situated at the western side of Aravali Delhi Fold belt having metasediments and basic volcanic rocks of Neoproterozoic (Heron, 1953). The MC has an igneous suite of rocks with a granite basement (Sinha-Roy, 1995). The NE-SW trending Delhi Supergroup of rocks has three phases of folding. The first and second phase of folding is present in Mesoscopic and macroscopic folds. The Marwar Supergroup (Neoproterozoic) of rocks comprises large sedimentary sequences bounded by Malani Volcanics in the western part. The intracratonic DFB rift basin contains ophiolite malange suite of rocks formed under the Oceanic environment by Ductile Shear Zone (Gupta et al, 1997).

MAGNETIC SURVEY

The regional ground magnetic survey has been carried out on a 1:50,000 scale with Proton Precession Magnetometer (PPM) under the project Geophysical Mapping Programme. In the present study area, the surveyed area is covered by six topo sheets of Survey of India measuring 4200 sq.km^2. A total of 1424 magnetic observations were occupied by keeping the one observation for every 2.5 sq. km, at roads, kilometer stones, and all such identifiable positions on the topo sheets. However, the data density was not maintained in areas that are not approachable due to very rugged terrain and also areas falling under reserve forest and water cover. The geographical coordinates of the magnetic stations were observed with Global Positioning System (GPS-Garmin, accuracy: 3-4 meter).

A magnetic base station has been established near to the camp area, which is free from magnetic disturbances and occupied every day at the starting and end of the survey for computing the diurnal correction. During the survey, four different magnetic bases have been established near the camp areas located at Barr and Jawaja in Ajmer district and Bijaya Nagar, Bhilwara district, Rajasthan. Proper care has been taken during the fieldwork for selecting the magnetic observations. At least five magnetic observations were made in the vicinity of every station. The average of three consistent readings was calculated and noted in the record book. Daily changes in the magnetic field due to changes in currents of charged particles in the ionosphere were removed through Diurnal correction by occupying the magnetic base station twice in a day (starting and ending of the survey). The normal correction is applied by using the IGRF-2010 module of Oasis Montaz-Geosoft software (Version 9.2) and IGRF-2010 has been subtracted from diurnal corrected filed data for computing the magnetic anomalies. The accuracy of the magnetometer reading is 0.1 nT.

QUALITATIVE APPRAISAL OF MAGNETIC DATA

The magnetic anomaly map has been prepared after removing the IGRF 2010 from diurnal corrected data, which is shown in Figure 2. The contour values vary from -310 to +200 nT. The regional trend of the anomalies is NE-SW direction and follows the general strike direction of the lithological units of the area. A series band of highs and lows of magnetic anomalies identified in the western part of the study area, demarcates the upliftment of basement rocks within the Delhi Fold Belt (DFB). The discontinuity of magnetic highs and lows are also observed over boundaries of older and younger formations within the Delhi Fold Belt. Based on the nature and continuity of the anomaly pattern six magnetic high anomaly axes are observed *viz.* (i). Jessikheda-Bharatiya Khurd (ii). Ratanpura-Gola (iii). Ajitgarh-Bagsuri (iv). Shambhugarh-Jharwasa trending NE-SW direction for several kilometres. (v). Hanotiya-Bhandanwara trending SW-NE and (vi). Shivpura-Gulabpura trending N-W direction (Figure 2). The variations in magnetic intensity is due to the presence of different litho units having different magnetic susceptibility and age of formation. Some bipolar magnetic anomalies of long-wavelength are also observed, which are indicative of intrusive within the DFB. Most of the intrusives follow the general trend of the geological formation. The intrusive complexes of the central and western parts of the study area are found as isolated bodies along NW-SE trending belts. The bi-polar nature of magnetic anomalies may be due to the intrusives consisting of pyroxene, hornblende, biotite and calcic-silicate in varying proportions.

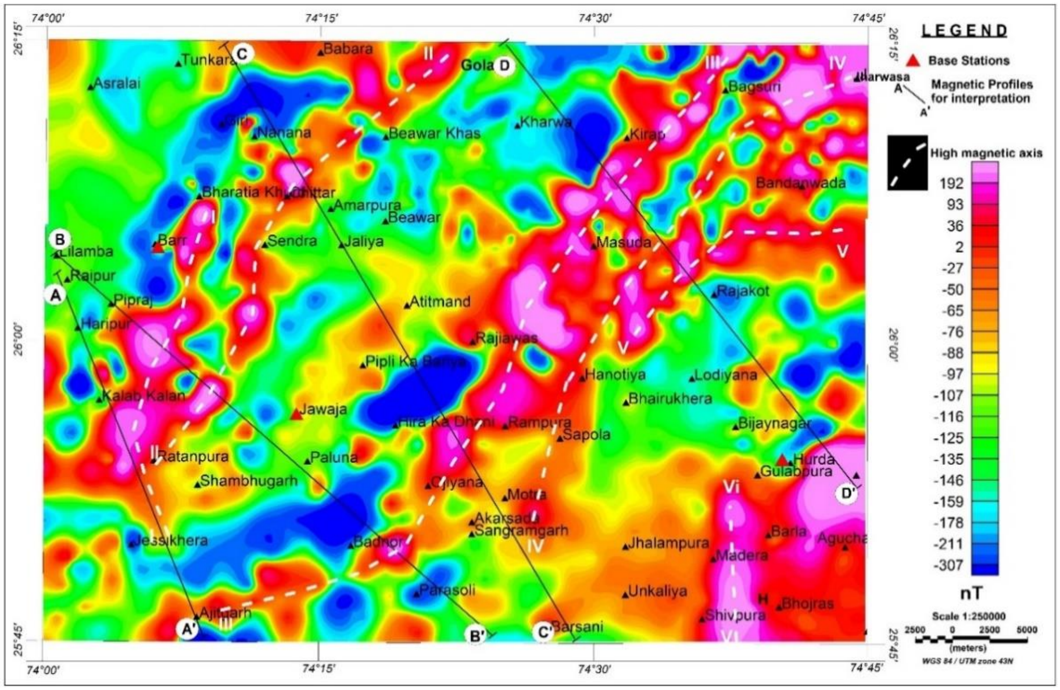

Figure 2. Magnetic contour map (IGRF-2010 corrected) showing high magnetic anomalies trending NE-SW direction and selected profiles for inversion ng. Prominent magnetic high axis (White hatched lines) AA´, BB´ CC´ and DD´ selected profiles for 2D modelling.

Elongated lows are found in the western portion of the area which may be due to the effect of intrusive in the South Delhi Fold Belt (SDFB). Another dominant high gradient feature from Kalabkalan- Babra is indicative of the faulted contact of the DFB and Marwar Basin (MB). This particular fault is well established and also explained by the many geoscientific investigations. Beyond that, the contour pattern takes a sudden turn along the E-W direction over biotite schist. Such magnetic trends in the DFB are interpreted as fault/contact-like structures. Further, the magnetic basement of the area is constituted by granite gneisses. Based on the basement configuration of the area, granite gneisses are located at shallow depth and exposed at a few locations along the NE-SW direction. The regional magnetic trends are well corroborated with the regional geological trend of the area. The tectonics of the DFB can be well explained by the basement configuration.

UPWARD CONTINUATION OF MAGNETIC DATA

In general, a low-pass filter can be used for enhancing the deep-seated sources. In the present study, the same type of filter, i.e. the upward continuation technique was applied to the magnetic data, the upward continuation can be used to enhance the regional magnetic anomalies, which are contributing to the sources at deeper depth (Hualin Zeng, 2007).

In the present study, the magnetic data was continued at four successive heights *viz.* (a) 500 m (b) 1000 m (c) 1500 m (d) 2000 m. The 3D view of continued maps has been presented in Figure 3. The characteristic signatures identified from the upward continuations are described below:

(i) Two broad high magnetic features are run in NE-SW direction from Ratanpura-Gola and Badnor-Jharwasa in all the four heights of continuation. The NW part of the study area shows low magnetic intensity over a thick alluvium/clay/sand of Marwar Basin (MB). The intrusive within country-rock of Delhi Fold Belt at the central part of the area was noticed in the form of discontinued weak magnetic anomalies. The weak magnetic response has been diminished at 2000 m level of upward continuation (Figure 3d) in the NW part. Whereas, the positive anomaly pattern in the DFB is still continued and it is inferred that the causative bodies (e.g. hornblende schist, granite gneiss, and amphibolites) in the DFB may have deeper roots than that of MB. The same type of study has been carried out by many workers (Thompson, 1982; Jacobsen, 1987; Reid, et al., 1990; Mushayandebvu et al.,2001; Radhakrishna Murthy and Rama Rao, 2001; Fitz Gerald, 2004). The high magnetic intensity has been noticed in the SE part of the study area (North of Agucha) in all four stages of continuation.

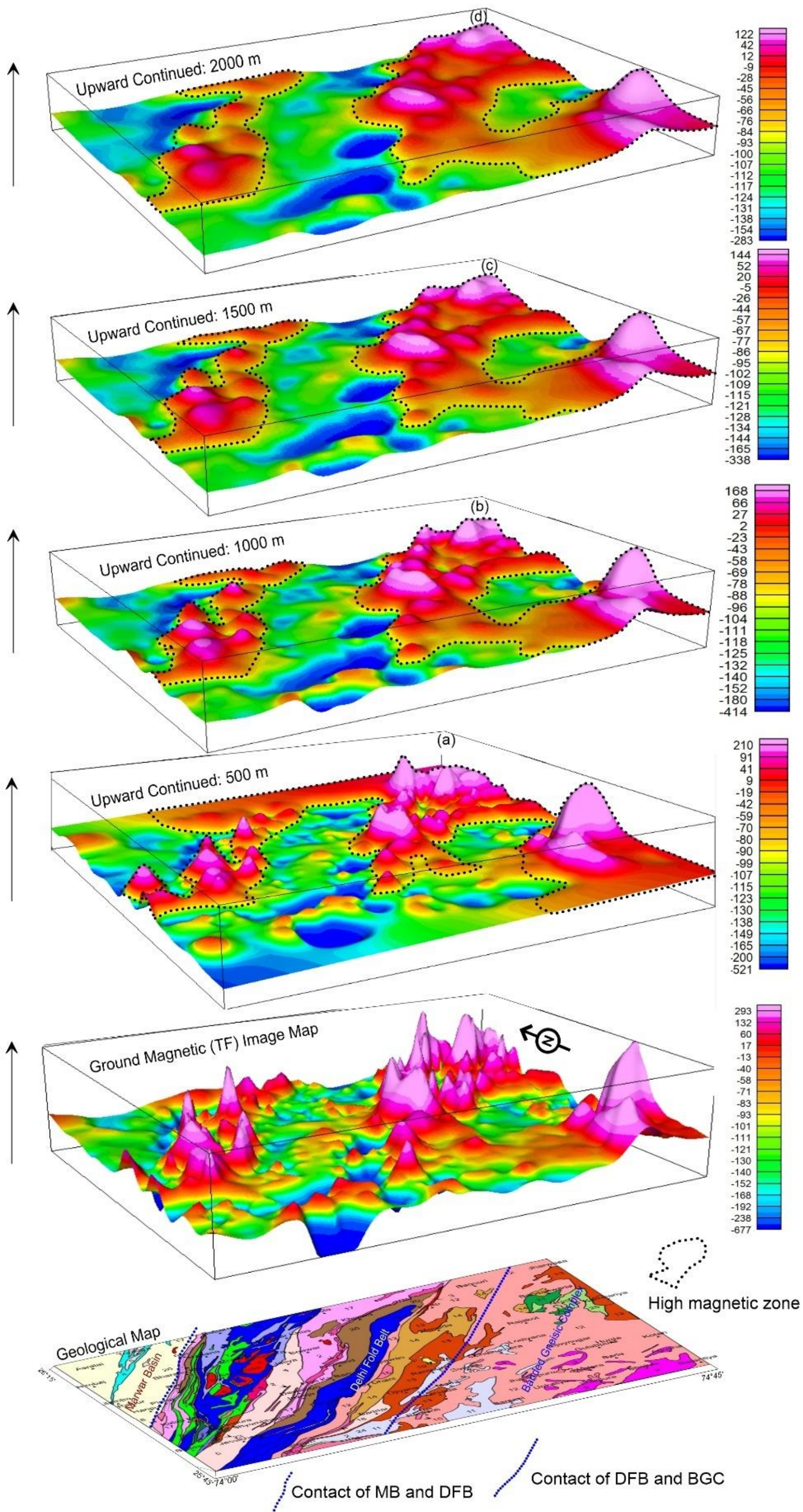

Figure 3. Upward continuation of the magnetic data at (a) 500, (b) 1000, (c) 1500 and (d) 2000 m levels and the same is superimposed on geological map of the study area. The dotted line is the trend of the high magnetic zone at all stages of observations.

J. Ind. Geophys. Union, 26(3) (2022), 165-181

(ii) It can be interpreted as a distinct high magnetic intensity body which is extending to deeper depths from the sub-surface level. There is a good correlation of geophysical and geochemical data over the Rampura-Agucha zinc-lead deposit forming a part of the pre-Aravalli Banded Gneissic Complex (Bangaru Babu et al., 2014). The high magnetic anomalies are due to the intrusives of acidic and basic igneous rocks, that predominantly occupy the southeastern plain of Ajmer and Bhilwara.

(iii) A high magnetic zone is recorded from Badnor to Bagsuri and Jassikhera to Gola, trending NE-SW direction over DFB gneiss. In addition to these two high magnetic zones, a low magnetic response was noticed on either side of the high magnetic intensity zone. The occurrence of low magnetic features appearing with high magnetic anomalies, can be seen in Figure 3a. The low magnetic responses disappear at the continuation level of 2000 m (Figure 3d). A number of low magnetic anomalies which appear in Figure 3a disappeared in Figure 3d, it indicating that the causative source body is of finite depth extent. The NE-SW trending peak magnetic anomalies are almost flat at the level of 1500 m to 2000 m. In this method, deeper features are very well separated, demarcating the tectonic contact of different litho units. The larger magnitude of the magnetic anomalies can be interpreted in terms of the magnetic basement extending deeper depth along with the source body (Figure 3d). The NW-SE trending high magnetic intensity from Badnor to Bagsuriare takes a sudden swing in the E-W direction in NE part of the study area. Hence, it can be concluded that the magnetic basement also changed its direction from NW-SE to E-W direction. Similar type of magnetic anomalies occurs over the Eastern Ghat Mobile Belt (EGMB) (Rahdakrishna Murthy and Rama Rao, 2001).

DEPTH ESTIMATION FROM THE POWER SPECTRUM

The Radially averaged power spectrum technique has been applied to magnetic data to estimate the depth interfaces, which reduces the noise from the (Telford et al, 1990 and Bhattacharyya and Leu, 1975). This technique can be used to determine the basement depth from the potential field data (Spector and Grant 1970). Here, we apply this method to the aquired magnetic data for estimating the magnetic depth interfaces. First, the radially averaged power spectrum was calculated using MAGMAP extension in Oasis Montaj (Geosoft) and then wave number (k) versus power spectral density ($\log_e P$) is plotted (Figure 4). The linear fit was applied to the different linear segments in the graph (Figure 4) and calculated the slope of each segment. A mean depth (z) of the anomaly source was obtained by utilizing the equation $z = -(\Delta \log_e P/\Delta k)/4\pi$. The depth of the causative source body has been calculated by simple formula i.e Slope of segment /4π. Three linear segments were observed in the radially averaged power spectrum of magnetic data (Figure 4). The calculated depths to the magnetic interfaces are 3 km (deeper layer), 2 km (middle layer), and 1 km (shallow layer) respectively.

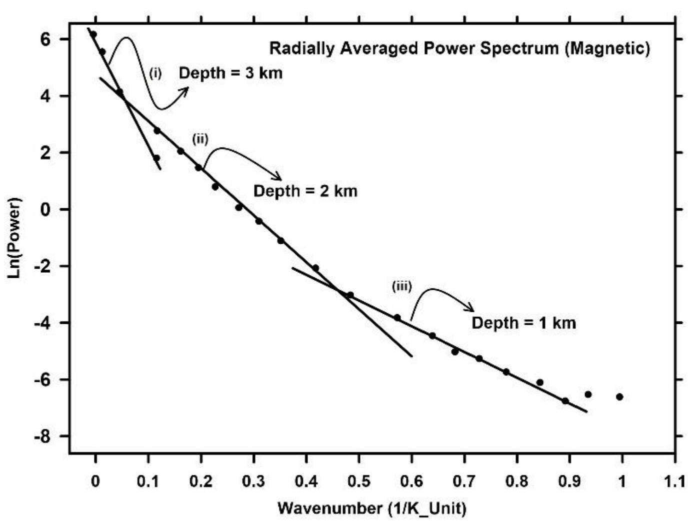

Figure 4. Radially averaged Power spectrum of the magnetic data showing three segments, i.e. (i) deeper sources, (ii) sub-surface and (iii) shallow depth which are computed from slope of segments.

ANALYTIC SIGNAL

The basic theories of the analytic signal method in 2D magnetic data interpretation is broadly explained by many workers (Nabighian, 1972, 1974, 1984; Green and Stanley, 1975). Similarly, the analytical signal of gravity data has been discussed by Klingele et al. (1991) and Gokaran et al. (1995). The analytic signal of the vertical magnetic gradient produced by a 3D source can be given as:

$$|A_m(x,y)| = \sqrt{\left(\frac{\partial m}{\partial x}\right)^2 + \left(\frac{\partial m}{\partial y}\right)^2 + \left(\frac{\partial m}{\partial z}\right)^2}$$

where $|A_m(x, y)|$ is the amplitude of the analytic signal at (x, y), m is the magnetic field at (x, y), and $\partial m/\partial x$, $\partial m/\partial y$ and $\partial m/\partial z$ are the two horizontal and one vertical derivative of the magnetic field. The analytic signal method is also known as the total gradient method. It is used for defining the edges/boundaries of lithological units. The analytic signal function is a very useful tool in the interpretation of magnetic data and to determine the location and depth of the magnetic sources. Analytic signal amplitude reaches its maximum value on its body or on the edge depending on the source (Shima, et al., 2015).

In this study, the analytic signal of magnetic data has brought out the picture of the aerial distribution of the high magnetic sources within DFB. The computer-generated analytic signal map of the present study area is shown in Figure 5. The high magnetic gradients are due to the magnetic sources at a depth. An attempt was made to map the intrusives within the DFB. The high magnetic gradients responses can be interpreted as intrusive within DFB, and they are mainly related to biotite schist. The magnetic sources, identified from the analytic signal map, are related to exhumed rocks of the high-grade granulites and schist rocks. A close look on the analytic signal map (Figure 5) shows a heavy concentration of magnetic sources in DFB that are trending NE-SW direction. The NE-SW trending belt of the schist rocks associated with the intrusives, is also picked up by the analytic signal map. It is interesting to note that there are no significant magnetic sources in the MB at the NW part of the study area. The same techniques have been applied to selected typical magnetic profiles for interpretation. The contacts of MB-DFB and DFB-BGC can be seen clearly marked in the form of the gradient in the analytical signal

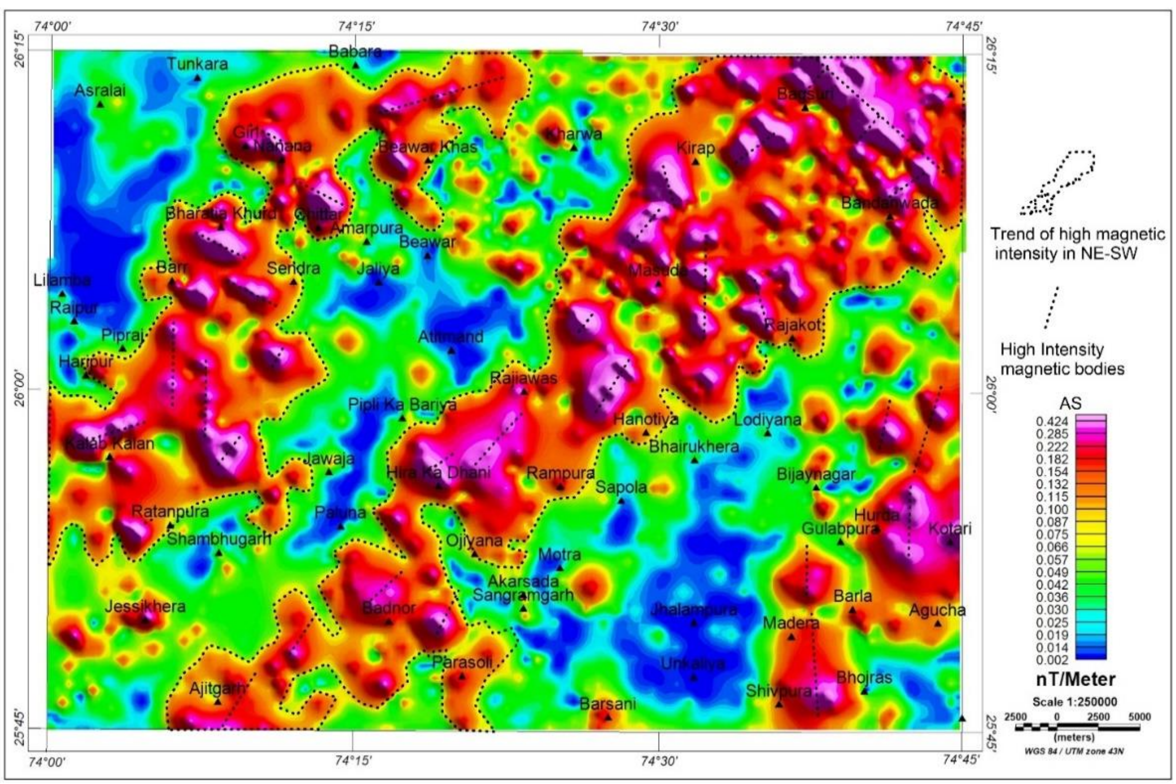

Figure 5. Analytic Signal (AS) map (magnetic data) of the part of the Delhi Fold Belt area showing high intensity magnetic bodies and their orientation.

3D-EULER DEPTH SOLUTIONS FROM MAGNETIC DATA

3D Euler deconvolution technique provides estimated geometrical parameters of elementary causative sources from the potential field data along with their derivatives along *X*, *Y* and *Z* directions. Initially, the Euler depth solution method assumes that anomaly is a homogeneous function of spatial coordinates. The technique (Thompson, 1982; Reid, et al., 1990) is initially used to detect the depth to the causative bodies that are calculated from the derivative analysis and analytical signal. it is a powerful technique for locating the anomalous source and its depth estimation from gravity and magnetic data (Blackely, 1995). The method is based on the Euler homogeneity equation and can be expressed for the potential field as follows

$$(x-x_0)\frac{\partial T}{\partial x}+(y-y_0)\frac{\partial T}{\partial y}+(z-z_0)\frac{\partial T}{\partial z}=-N(B-T)$$

Where (x_0, y_0, z_0) are the coordinates of the causative body, Total field T is measured at (x, y, z) and B is the background field; N indicates Structural Index (SI) of the source body and relates to the rating of change of potential with distance. It plays a crucial role in potential field depth estimation (Reid, et al., 2014). For obtaining reliable solutions, the structural index, the window size and depth tolerance need to be selected judiciously. Before generating the Euler depth solutions, the interpreter should have knowledge of geology and tectonics of the area. In general, selection of the proper structural index depends on the geological environment of the area. The user-defined depth tolerance controls the number of acceptable solutions. Although, the Euler method suffers from some theoretical limitations, but still provides useful results for practical purposes (Reid, et al., 2014). In the present study, the 3D Euler depth technique has been applied to the magnetic data with a structural index of 0.5 for generating the depth solutions. The cluster of depth solutions has been posted over the geological map of the study area for a better understanding of the sources of depth solutions (Figure 6).

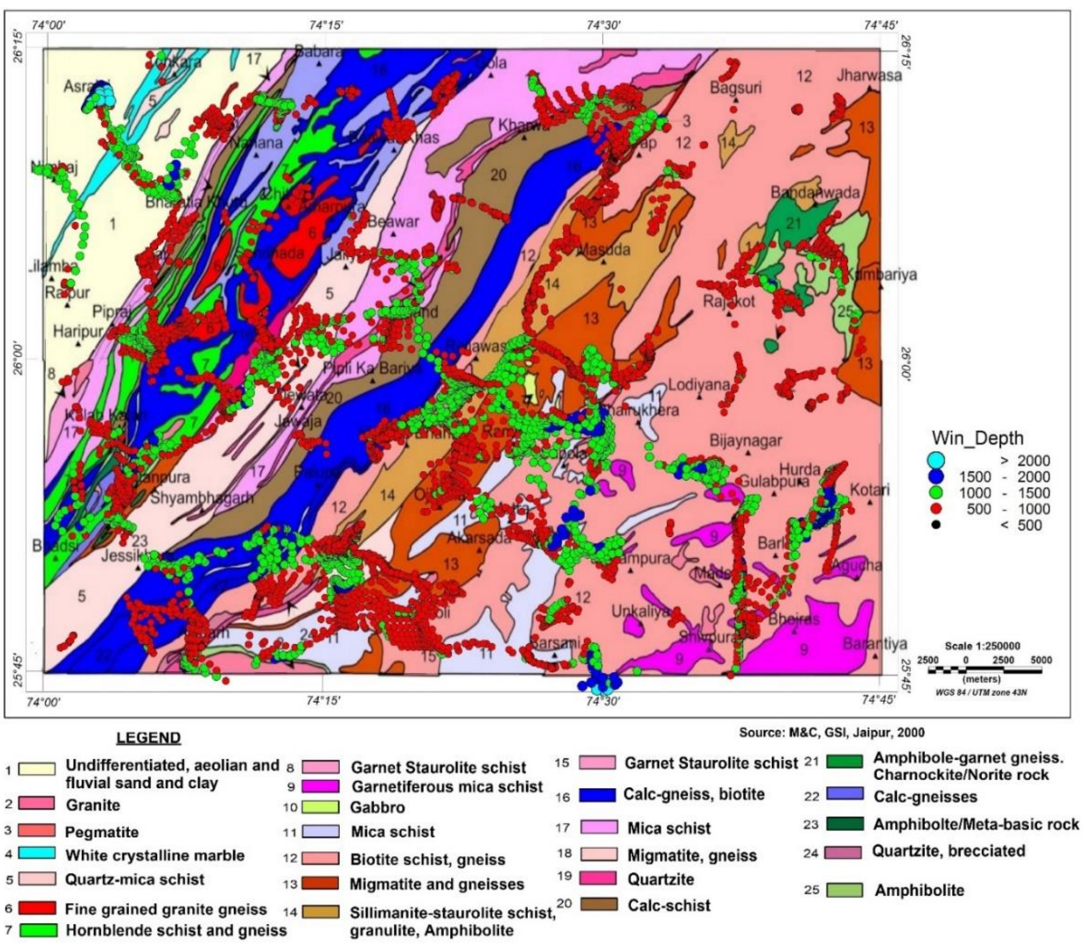

Figure 6. 3D Euler depth solutions superimposed on geology of the area. Structural Index = 1. shallow depth (500 m) and deeper depth (2 km).

The cluster of Euler depth solutions provides an idea about the depth of magnetic anomaly sources and locations. It is noticed that the shallow (500 to 1000 m) depth solutions have been generated over Delhi's sediments. It can be interpreted as magnetic anomaly are near to sub-surface level. The technique has generated the best solutions (tight clustering) along with the inferred contact of MB and DFB, with a depth ranging from 500 to 1500 m in NW part of the area. The most of the cluster of depth solutions were generated along regional strike of the area.

As mentioned earlier, in the Euler technique Structural Index (SI) and window size parameters play a key role generation of depth solutions. Thus, the depth solutions were generated with various Structural Indices and window sizes. Finally, the best SI (1) and window size (20x20) were selected for the generation of the Euler depth solutions. These were compared with the depth interfaces obtained from spectral analysis of magnetic data. The cluster of depth solutions was generated along the regional geological strike of the area (Figure 7). Most of the shallow depth solutions (500-1500 m) were generated over the DFB and very few deeper solutions (1500-2000 m) were found over the BGC. It means that, the magnetic source bodies are largely located near to sub-surface below DFB.

Similar type of clustering of solutions s also been reported over the Palaghat-Cauvery Shear zone from aeromagnetic studies (Anand and Rajaram, 2007). From the Euler depth solutions, many cluster depth trends are identified, indicating the locus of magnetic source points along structural lineaments. Such type of trends based on regional geophysical studies are also earlier reported by Bangaru Babu et al. (2015). We find that the magnetic depth sources over MB is deeper, compared to the DFB.

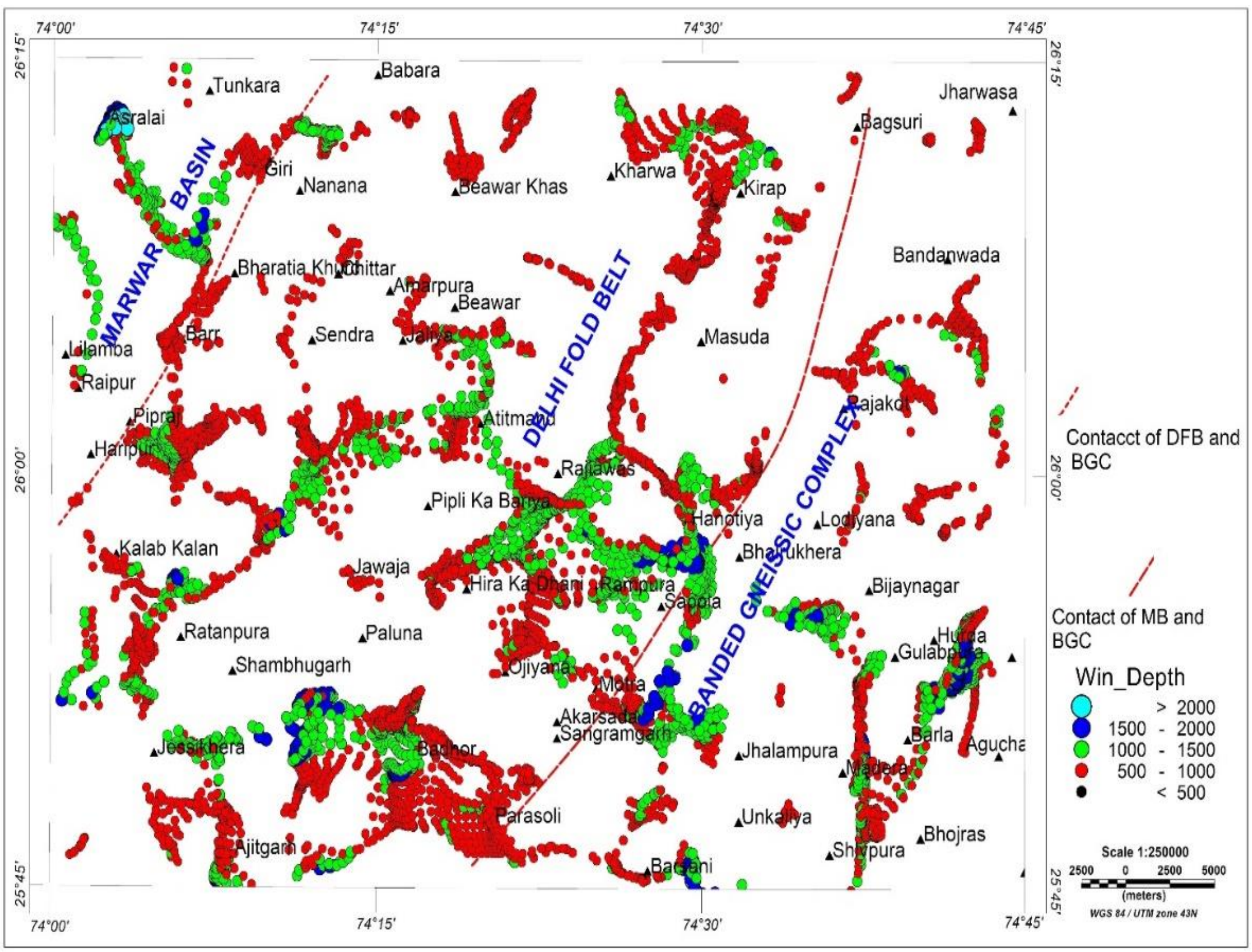

Figure 7. 3D Euler depth solutions in the present sudy area along with major geological boundaries (Red colour lines).

2D MODELLING AND INVERSION

Four profiles -AA´, BB´, CC´ and DD´ are selected across the Delhi Fold Belt (DFB). Initially, the profiles are inverted considering different geophysical models (Dyke and Sheet-like body) using the FORTRAN - based computer programs (Radhakrishna Murthy, 1998) (TDYKEIN and TSHEETIN). The adopted inversion works based on the Werner deconvolution technique and estimated the magnetic basement and intensity of magnetization. The model of juxtaposing prisms conveniently manages inversion (TMAG2DIN) of magnetic anomalies of two-dimensional basement structures. The material of the magnetic basement above and below are equated to a series of juxtaposed prisms one below each anomaly point. The depths to their tops (equal to the basement depth) are determined to give the continuous basement structure below the profile.

Profile-AA´

Profile-AA´ from Raipur to Ajitgarhwas cuts across part of the Marwar Basin (MB) and Delhi Fold Belt (DFB). The magnetic interface of the profile has been computed using the TMAG2DIN computer program in FORTRAN language based on the inversion method (Radhakrishna Murthy, 1998). The results of the inversion is plotted and displayed in Figure 8. The magnetic interface is undulating between 1.1 to 2.2 km. The shallow depth (~1.1 km) has been noticed in the NW portion of the profile over MB. The profile-AA´ has also been subjected to spectral analysis using 1D-FFT for calculating source depth. The mean depth of 1.3 km was calculated from spectral analysis. The sharp fall in magnetic anomaly around -200nT near Haripur –Kalab Kalan area has been interpreted as a contact of the Marwar Basin (MB) and Delhi Fold Belt (DFB) (Figure 7). Such a contact zone has also been picked up by Analytic Signal (AS), Reduction To Pole (RTP) and Horizontal Derivative (HD) of the profile. The role of the AS and HD helps in mapping the shallow structures (Fairhead, et al., 2011 and Marson and Klingele, 1993). The above said filter techniques have been applied to selected magnetic profiles by using 1D-Fast Fourier Transformations (1D-FFT) to study the nature and trend of contacts/lineaments and regional magnetic anomalies. These techniques played an important role in demarcating the contacts of MB-DFB and DFB-BGC (Banded Gneissic Complex) by showing a sharp fall in the magnitude of the anomalies. A high magnetic anomaly of -200nT has been observed near Kalab Kalan area. The contact zone of MB-DFB is well reflected in regional gravity surveys as well (BangaruBabu et al., 2014). The high values of Sulphide mineralization and high anomalous gold values (20-300 ppb) are studied from geochemical data. The above said mineralization is located between the contact of MB-DFB. In general, the Analytic Signal (AS) maxima occurs directly over the edges of the source bodies (Roest et al.,1992; Mac Leod et al., 1993). The Reduction to Pole (RTP) technique is also applied to Profile-AA´. In general, RTP is a theoretical solution, which normalizes the effect of induced magnetization and the strike. The RTP anomaly over an intrusive body near Kalab Kalan area has no remanence magnetization, Such type of features can be interpreted as intrusive/dyke like bodies (Rajagopalan, 2003).

Earlier, the complex homogeneity of lithological units between the MB and DFB has been interpreted in the form of the steep gravity gradient zone (Vijaya Rao et al., 2000), which suggests it to be a proterozoic collision boundary of two different litho units. The collision contacts, as revealed from regional geophysical studies, also support the rift environment over DFB (Sinha-Roy, 1998).

Profile BB´

This profile constructed along the Lambia-Lilamba-Badnor-Parasoli region is almost parallel to the profile AA´. The estimated magnetic interface below the profile vary from 1.0 to 2.5 km from the inversion method using the computer program TMAG2DIN. The mean depth of 2.1 km was calculated from 1D-FFT spectral analysis. The profile has been selected in such a way to cover the intrusives, which are well picked up showing alternating highs and lows in the analytic signal as well as in the horizontal derivative of the profile. The plot of the profile BB' is shown in Figure 9. In general, AS can be useful for demarcating the lithological boundaries/contacts of two different units (Nabighian, 1972, 1974, 1984; Green and Stanley, 1975, Fairhead, et al., 2004).

The first-order Horizontal Derivative (HDR) was applied to delineate the edges of magnetic bodies. It is commonly applied to the potential field data to delineate near-surface geological features and to enhance the high wavenumber components of the spectrum. The zero values of the derivative of the RTP commonly represent to the geological boundaries (Evjen, 1936). The zero value of HDR has been observed near Pipraj and Badnor villages along with this profile, which can be interpreted as contact between Delhi Fold Belt and Marwar Basin.

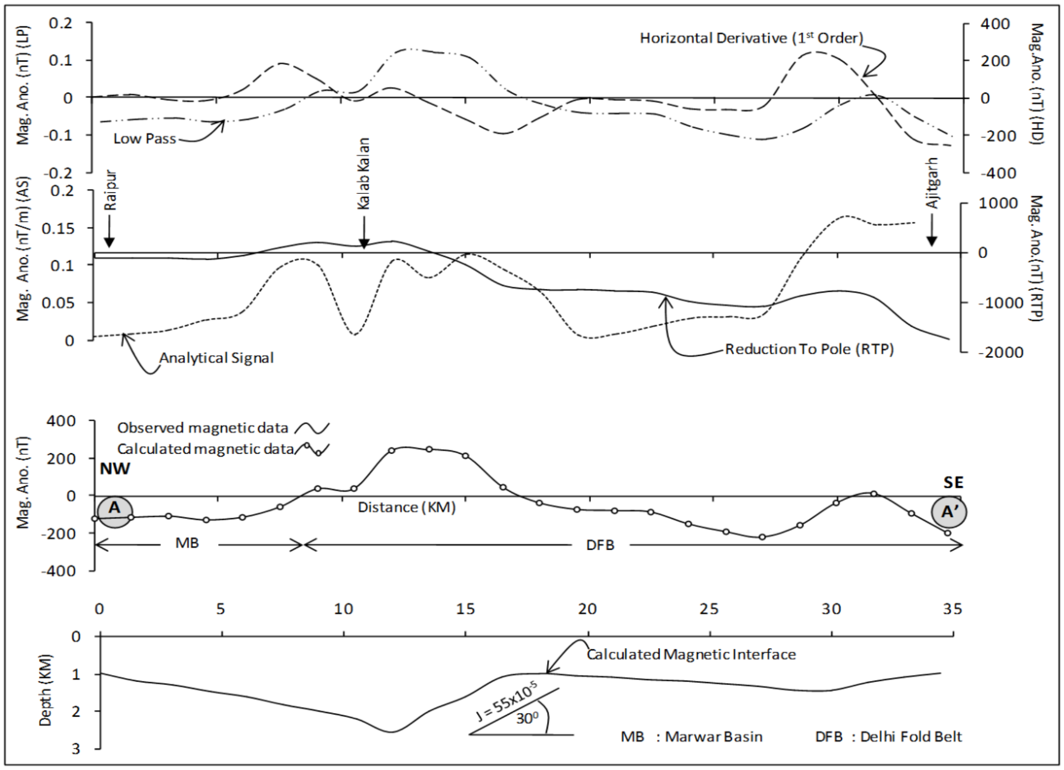

Figure 8. Probable 2D magnetic basement model of the profile AA´

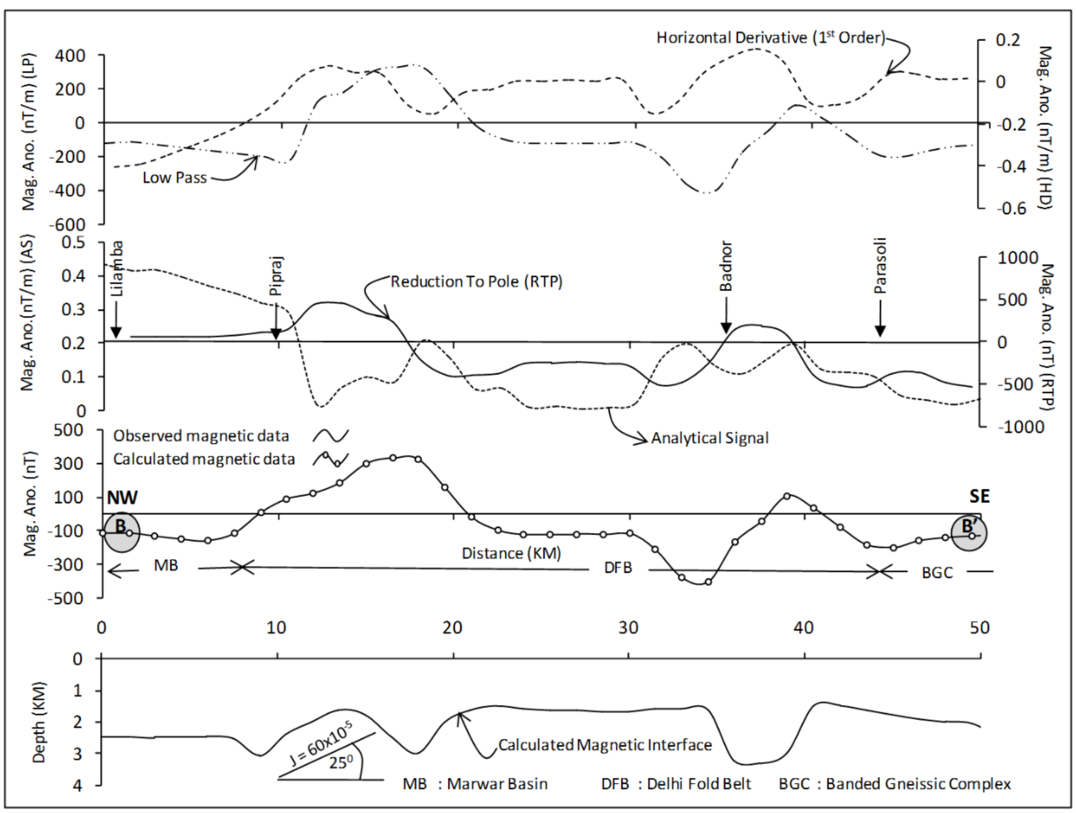

Figure 9. Probable 2D magnetic basement model along the profile BB´.

Profile CC´

This is another profile which runs from Tunkore to Barsoli which showthe total depth variation of 1.5 to 2.5 km after applying the inversion technique. The variation in amplitude of the analytic signal and its derivative is interpreted as an intrusive body at a depth of 2.0 km (Figure 10). The mean depth (1.82 km) along this profile was calculated from the spectrum of the profile. A sudden fall in analytical signal has been noticed and is interpreted as contact of MB and DFB, and beyond the DFB, the magnitude of anomalies varies from +100nT to -400 nT, which can be interpreted as a horst like a feature associated with intrusives within DFB. A close look at the nature and trend of the profile in the SE part, and also the gradient in the magnetic anomaly, can be interpreted as a contact between DFB and BGC.

Profile DD´

This profile runs from Babara to Bhojras, covering only DFB (Figure 11). The best suitable magnetic interface has been delineated by adjusting the input parameters in a computer program. Subsequently, the AS and HDR filters are also applied to magnetic profile data for marking the contacts/boundaries of DFB-BGC. A few intrusives like bodies are identified at Masuda and Rajakot. Based on the low pass filter of magnetic data, it is concluded that intrusive bodies are near to the sub-surface and not extend deep. The magnetic interface of the profile varies from 1.0 to 2.0 km. The mean depth of about 2.1 km was estimated from spectral analysis of the profile data. The contact/boundaries of DFB-BGC are clearly demarked in the HDR and AS near to Rajakot.

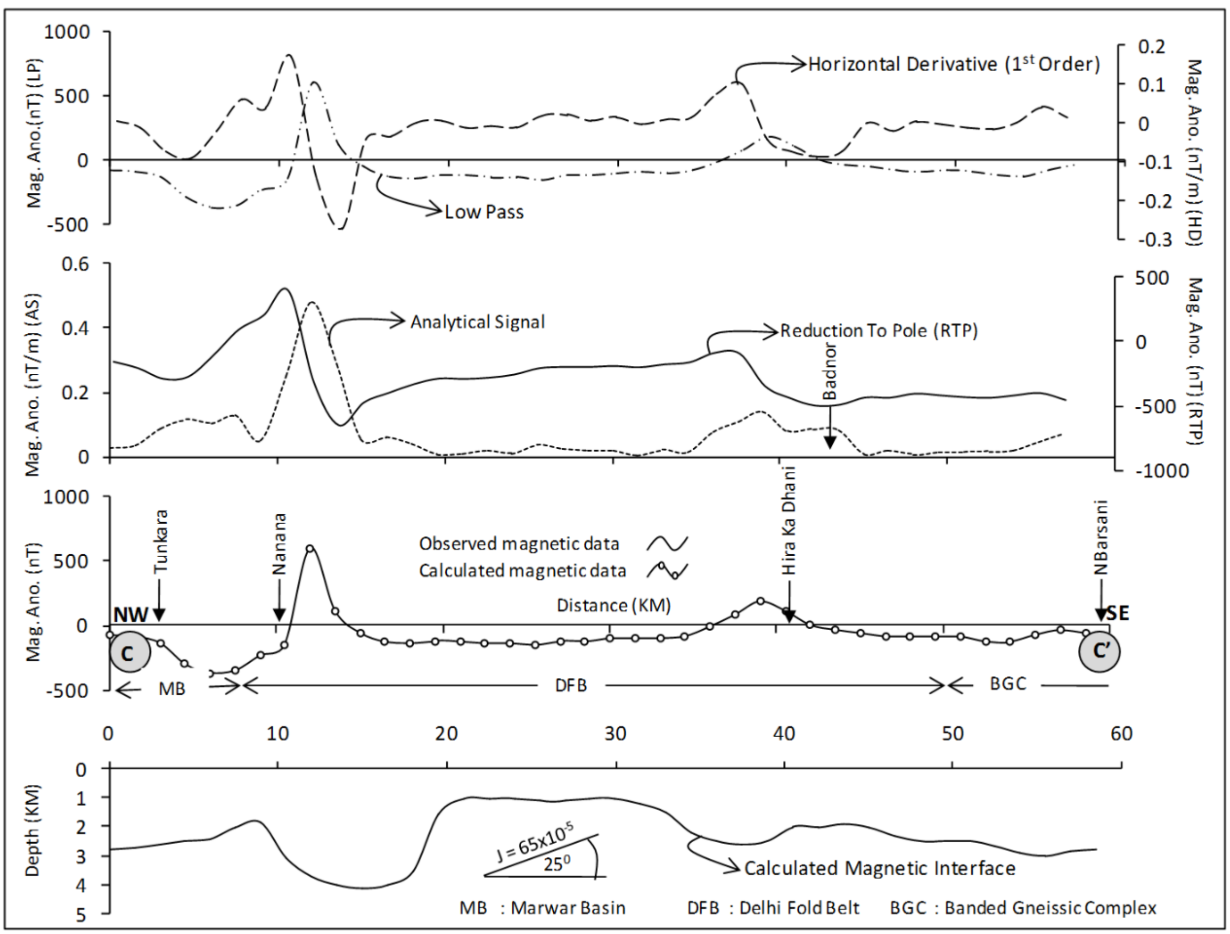

Figure 10. Probable 2D magnetic basement model along the profile CC´.

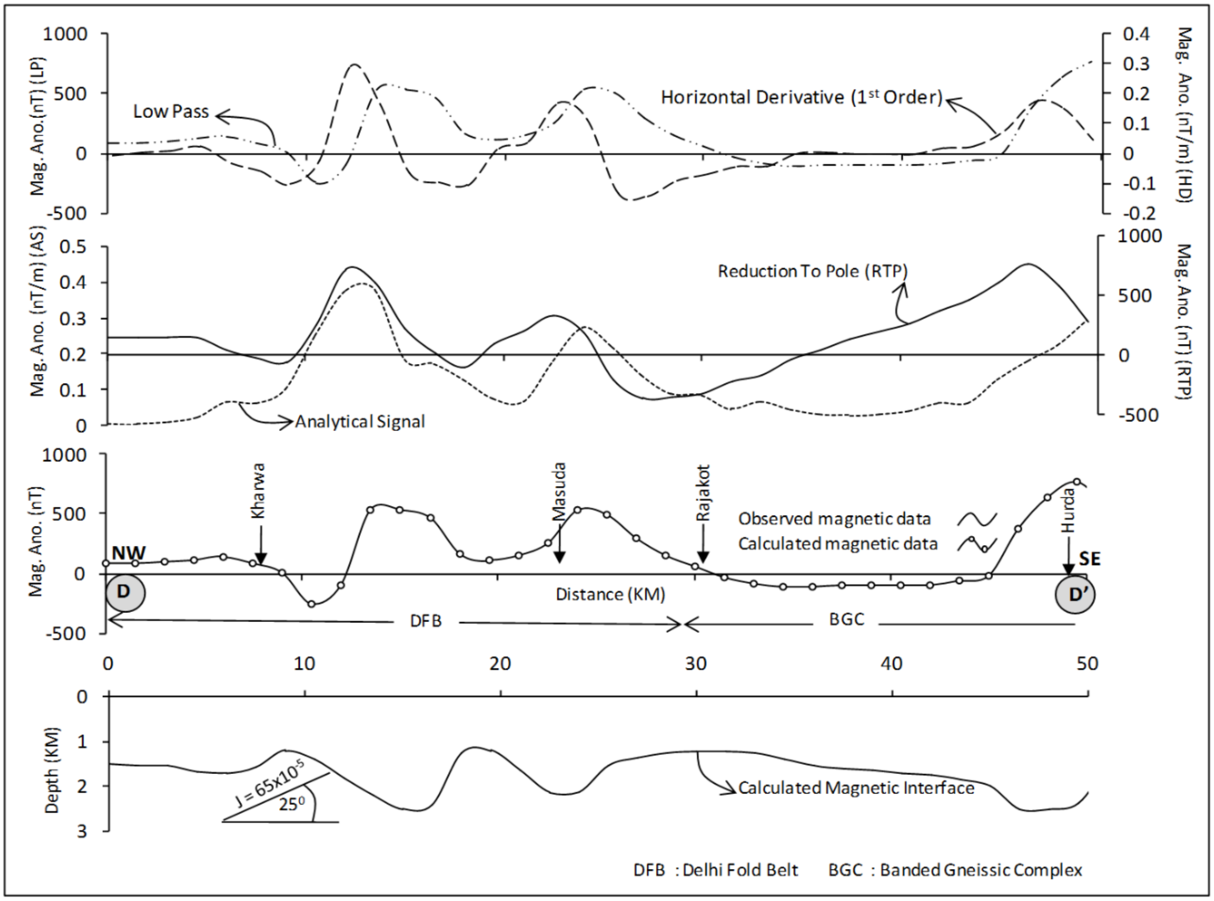

Figure 11. Probable 2D magnetic basement model along the profile DD´.

DISCUSSIONS

Spectral Analysis of Profile Data

Depth estimation from spectral analysis of potential field data provides a reasonable assumption of the depth to the anomalous source. It is a frequency domain approach that is capable of separating the information from anomalous sources at different depths. In this study, 1D Fast Fourier Transform (FFT) technique of Geosoft software has been used for generating the spectrums of magnetic profile data. The depths can be estimated from the slope of the line segment plotted between the log of power (*P*) and wavenumber. The power spectrum of the gridded potential data was computed using the method of Spector and Grant (Spector and Grant, 1970; Karner and Watts, 1983; Roest, et al., 1992) and a graph of the logarithm of the azimuthally averaged power spectrum against wavenumber.

Four typical magnetic profiles AA´, BB´ CC´ and DD´ have been constructed in the study area and subjected to spectral analysis using 1D-FFT for calculating the source depth of each profile. These profiles were selected in such a way to study the magnetic basement structure below DFB. The results obtained from the spectral analysis have been justified with depth calculated from the other depth estimation techniques. The corresponding power spectrum plots obtained for the profiles are presented in Figure 12. In general, the linear segment from the low-frequency portion of the spectrum represents contributions from the deep-seated causative bodies. The sedimentary rocks generally have very weak magnetic susceptibility compared to basement rocks. Therefore, variations within the magnetic intensities over sedimentary basins are considered to originate from (i) basement structure, (ii) intrusive and extrusive volcanic bodies within and beneath the basin, and (iii) susceptibility contrast (Behrendt and Klitgord,1980). Different methods have been adopted for estimating the depth from magnetic data (Peters, 1949; Vacquier et al., 1951). For this study, initially, the spectral analysis method was used because of its ability to filter all the noise from the data and no information is lost in the process. The average depth to the basement obtained ranges from 1.2 to 2.1 km. The average depths determined for each profile from the spectral analysis are given in Table 1.

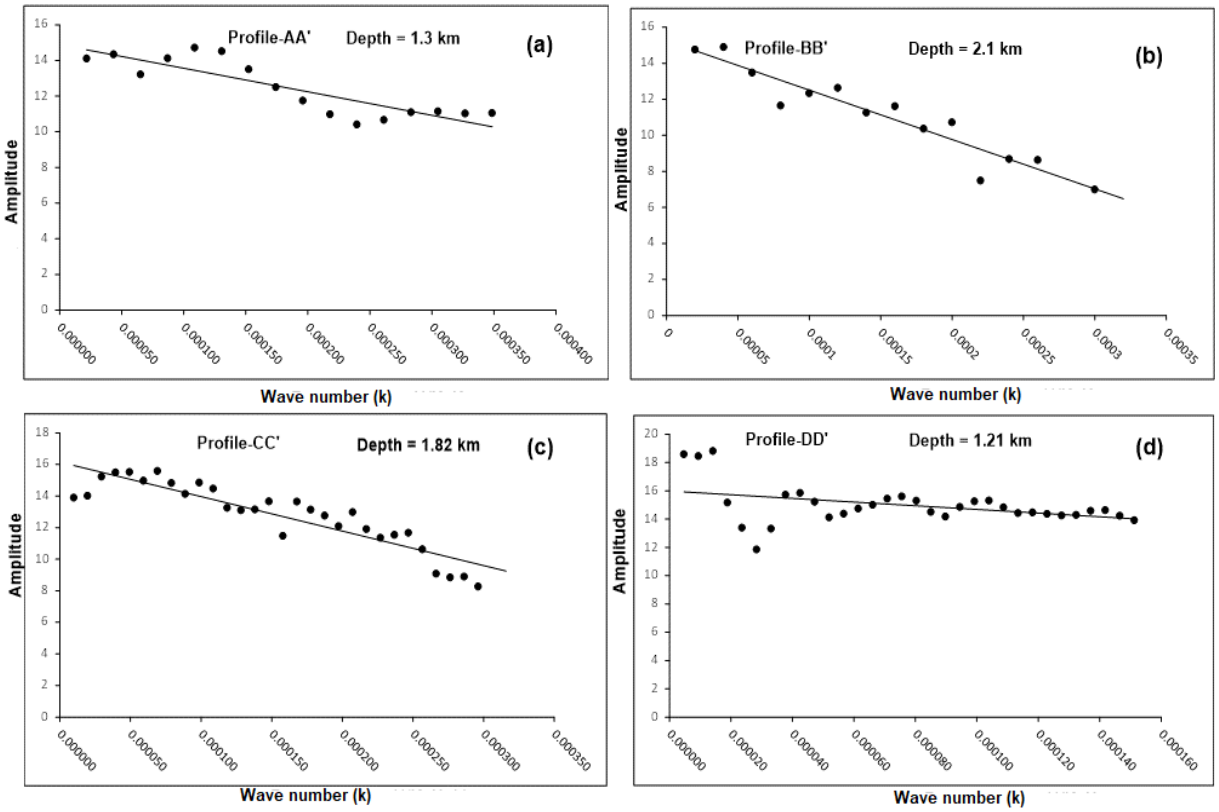

Figure 12. Power spectral plots corresponding to the profiles selected for interpretation and the corresponding adjustment line and estimated depth to the top of the basement.

Table 1. Depth obtained from spectral analysis of selected magnetic profiles

Name of the Profile	Direction of the Profile	Gradient Anomaly	Depth (km)
Profile AA´	NW-SE	2.25	1.30
Profile BB´	NW-SE	7.12	2.10
Profile CC´	NW-SE	4.21	1.82
Profile DD´	NW-SE	1.21	1.21

Structural Implications

The magnetic bipolar anomalies have been noticed and considered for the interpretation of four selected profiles. The average magnetic depth interface in the area range from 1.21 to 2.1 km. The tectonics of the region controls the different structural trends in the study area, and one can demarcate the boundaries/ contacts of DFB and MB. The interpretation of magnetic data helped to identify the magnetic sources and estimate the depth to the top of the magnetic sources. The prominent magnetic high anomalies in the study area are due to undulations in the magnetic basement. The results of this study, therefore suggest that the high magnetic zones observed in the area trend in the NE-SW direction, as most of the known structures are located in and around the DFB. The calculated magnetic interfaces obtained from the inversion is displayed in Figure 13. The surface contact of MB and DFB is not only marked from magnetic anomalies, but it also highlighted the magnetic interface. The calculated magnetic depth interface from inversion is well corroborated with the cluster of depth solutions generated from the 3D Euler depth technique. In the present case, different depth estimation techniques have been used for calculating the average magnetic basement depth. The average depth estimations were presented in Table 2.

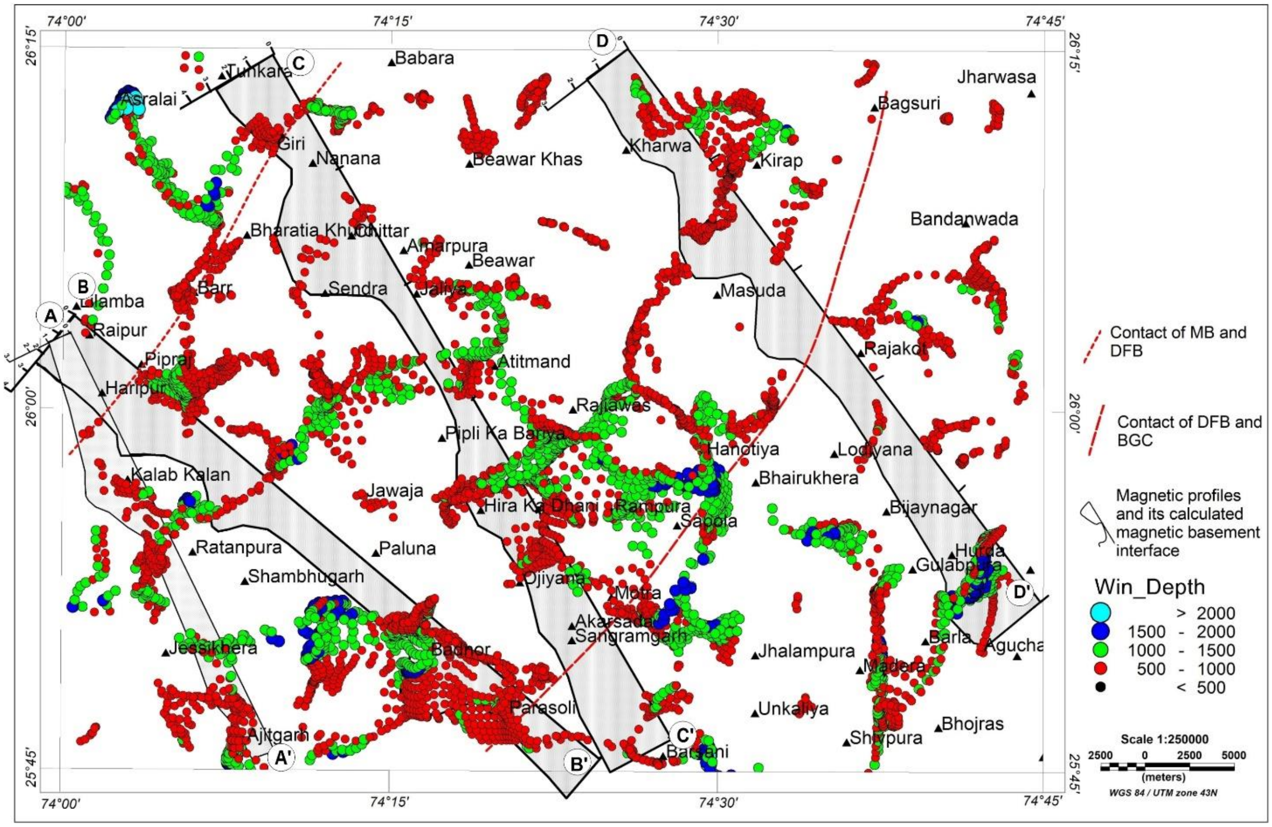

Figure 13. Magnetic basement along the profiles AA´, BB´, CC´ and DD´ derived from inversion superposed on 3D Euler depth solutions.

Table 2. Average basement estimated from different techniques

S.No	Name of the profile	Depth (km)			Average depth (km)
		Spectrum	Inversion	3D Euler	
1	Profile AA´	1.30	1.50	1.25	1.35
2	Profile BB´	2.10	2.50	2.00	2.11
3	Profile CC´	1.82	2.20	2.00	2.00
4	Profile DD´	1.21	1.30	1.25	1.55

CONCLUSIONS

The magnetic survey brought out a high magnetic trend along with the general trend of the geological formations in and around the Delhi Fold belt. The varying structural patterns within the study area is controlled by the tectonics of the region and one can identify three different litho units,i.e. Marwar Basin, Delhi Fold Belt and Banded Gneissic Complex. The inversion of the selected profiles helped to classify the magnetic sources and their depths to the top. The magnetic data brought out the primary contact of the significant lithounits, i.e.Marwar Basin (MB) and Delhi Fold Belt (DFB). The connection of MB and DFB is discussed in view of the calculated magnetic interfaces. It is concluded that, the geologic contact zones are structurally controlled and respective magnetic sources at depths.

ACKNOWLEDGEMENTS

The present work was carried out as a part of the National Geophysical Mapping Program of Geological Survey of India, Western Region, Jaipur. The authors are thankful to

Shri.R.S.Rana, Addl. Director General & HOD, Geological Survey of India, Western Region, Jaipur for allowing to carry out this investigation, for technical guidance during his field visit and for providing logistic support and kind approval of the report. The authors express their sincere gratitude to Officer In-charge for his keen interest in the successful completion of the investigation and technical discussions, valuable suggestions, guidance during fieldwork and scrutiny of the report. The authors express their sincere thanks to Regional Mission Head, Mission-I for going through the manuscript and offering valuable suggestions in finalizing the report. The authors also express their gratitude to drivers, technicians and surveyors for their sincere co-operation for the successful completion of fieldwork smoothly.

Compliance with Ethical Standards

The authors declare no conflict of interest and adhere to copyright norms.

REFERENCES

Anand, S.P. and Rajaram, M., 2007. Aeromagnetic signatures of the craton and mobile belts over India. Int. Assn. Gond. Res. Mem., 10, 233-242.

Bangaru Babu, S., Kulkarni, A.V., Lakshmana, M., Amar Singh, Singh, L.N., and Dinesh Gupta, 2014. Delineation of Delhi's Basement Interface in Sandmata Complex and South Delhi Fold Belt from Gravity studies., J. Geophys, 2, 59-66.

Bangaru Babu, S., Kulkarni. A.V., Lakshmana. M., Amar Singh and Dinesh Gupta, 2015. Regional gravity surveys under National Geophysical Mapping Programme (NGPM) and their significance in Mineral exploration, Recent developments in Metallogeny and Mineral exploration in Rajasthan, Geol. Sur. Ind. Spl. Publ., 101, 96-101.

Behrendt, J.C. and Klitgord, K.D., 1980. High-sensitivity aeromagnetic survey of the US Atlantic continental margin. Geophysics., 45, 1813–1846.

Bhattacharyya, B.K. and Leu, L.K., 1975. Spectral analysis of gravity and magnetic analysis due to two dimensionless structures, Geophysics, 40, 993-1013.

Blackely, R., 1995. Potential theory in Gravity and Magnetic applications, Cambridge University Press, New York.

Evjen, H.M., 1936. The place of the vertical gradient in gravitational interpretations, Geophysics., 1, 127–136.

Fairhead, D., Mackenzie, C., Green, C.M. and Verduzco,B., 2004. A new set of magnetic field derivatives for mapping mineral prospects, ASEG Ext, Abst., DOI: 10.1071/ASEG2004ab042.

Fairhead,D. J., Ahmed S. Salem, Liliana Cascone and Hammilli, M ., 2011. New developments of the magnetic tilt- depth method to improve structural mapping of sedimentary basins, Geophysical Prospecting, 59, 6, 1072 – 1086, DOI:10.1111/j.1365-2478.2011.01001

Fitz Gerald, D., Reid, A. and McInerney, P., 2004. New discrimination techniques for Euler deconvolution, Comp. Geosci.,30, 461–469.

Gokaran, S.G., Rao, C.K. and Singh, B.P., 1995. Crustal structure in southeast Rajasthan using Magnetotelluric techniques, In: Sinha-Roy, S., Gupta, K.R. (Eds.), Continental Crust of NW and Central India, Geol. Soc. India, Mem., 31, 373-381.

Green, R. and Stanley, J.M., 1975. Application of a Hilbert transform method to the interpretation of surface-vehicle magnetic data, J. Geophy. Pros., 23, 18–27.

Gupta, S.N., Arora, Y.K., Mathur, R.K., Iqballuddin, P.B., Sahai, T.N. and Sharma, S.B., 1997. The Precambrian Geology of the Aravalli Region, Southern Rajasthan and Northeastern Gujarat, Geol. Soc. of Ind.Mem., 123.

Heron, A.M, The Geology of Central Rajputana., 1953. Geol. Sur. Ind. Mem., 1-139.

Hualin Zeng , Xu, D. and Tan, H., 2007. A model study for estimating optimum upward-continuation height for gravity separation with application to a Bouguer gravity anomaly over a mineral deposit, Jilin province, northeast China, Geophy.,72, 4, I45-I50, DOI: 10.1190/1.2719497.

Jacobsen, B.H., 1987. A case for upward continuation as a standard separation filter for potential-field maps, Geophy.,52, 1138–1148.

Karner G. D. and Watts A. B., 1983. Gravity Anomalies and Flexure of the Lithospere at Mountain Ranges, Jour. Geophy Res., 88, 10449-10477.

Klingele, E. E., Marson, I. and Kahle, H. G. 1991. Automatic interpretation of gravity gradiometric data in two dimensions: vertical gradient, Geophy. Pros., 39, 407–434.

MacLeod, I.N.K. Jones and T.F, Dai., 1993. 3-D analytic signal in the interpretation of total magnetic field data at low magnetic latitudes, Exp. Geophy., 679-688.

Marson, I. and Klingele, E. E. 1993. Advantages of using the vertical gradient of gravity for 3-D interpretation, Geophy., 58, 1588–1595.

Mishra, D.C., Laxman, G., Rao, M.B.S.V., Gupta, S.B., 1995. Analysis of gravity- magnetic data around Nagaur-Jhalawar geotransect. In: Sinha-Roy, S., Gupta, K.R. (Eds.), Continental Crust of NW and Central India, Geol. Soc. India, Mem., 31, 345-352.

Mishra, D.C. Singh, B. Tiwari, V.M. Gupta, S.B. Rao, M.B.S.V., 2000. Two cases of continental collisions and related tectonics during the Proterozoic period in India - insights from gravity modeling constrained by seismic and magnetotelluric studies, Precam. Res., 99, 149–169.

Mushayandebvu, M.F., van Driel, P., Reid, A.B., Fairhead, J.D., 2001. Magnetic source parameters of two-dimensional structures using extended Euler deconvolution., Geophy., 66, 814–823.

Nabighian, M.N., 1972. The analytic signal of two-dimensional magnetic bodies with polygonal cross-section: its properties and use for automated anomaly interpretation, Geophy., 37, 507–517.

Nabighian, M.N., 1974. Additional comments on the analytical signal of two dimensional magnetic bodies with polygonal cross-section, Geophy., 39, 85–92.

Nabighian, M.N., 1984. Toward a three-dimensional automatic interpretation of potential field data via generalized Hilbert transforms: Fundamental relations, Geophy., 49, 780–786.

Peters, L., 1949. The direct approach to magnetic interpretation and its practical application, Geophy., 14, 290–320.

Qureshi, M.N., 1964. A geological analysis of Bouguer anomaly peninsular India, Proc. Nat. Inst. Sci. Ind.,30, 675-688.

Qureshi, M.N., 1976. Relation of gravity to elevation and rejuvenation of blocks in India, Jour. Geophy. Res., 76, 545-557.

Radhakrishna Murthy, I. V., 1998. Gravity and Magnetic Interpretation in Exploration Geophysics, Geo. Soc. Ind., Mem., 40.

Radhakrishna Murthy, I.V. and Rama Rao, P., 2001. Magnetic anomalies and basement structure around Vizianagaram, Visakhapatnam and Srikakulam districts of Andhra Pradesh, India, Gond. Res.,4, 443-454.

Rajagopalan, S., 2003. Analytic Signal vs. Reduction to Pole: Solutions for Low Magnetic Latitudes, 16th Geophy. Conf. Exhi. ASEG Ext. Abst., 1-4, DOI: 10.1071/ASEG2003ab136.

Reddi, A.G.B., Ramakrishna, T., 1988. Bouguer atlas of western India (Rajasthan and Gujarat) shield, GSI. Spl. Publ.

Reid, A.B., Allsop, J.M., Granser, H., Millett, A.J., Smerton, I.W., 1990. Magnetic interpretation in three dimensions using Euler deconvolution, Geophy., 55, 80–91.

Reid, A. B., J. Ebbing, and S. J. Webb., 2014. Avoidable Euler errors — The use and abuse of Euler deconvolution applied to potential fields, Geophy. Prospecting., DOI: 10.1111/1365-2478.12119.

Roest, W.R,. Verhoef, J. and Pilkington, M., 1992. Magnetic interpretation using 3-D analytical signal, Geophy., 57, 116-125.

Saibi,H., Nishijima,J., Ehara, S. and Aboud, E., 2006. Integrated gradient interpretation techniques for 2D and 3D gravity data interpretation, Ear. Pla. Sci., 58**,** 815–821.

Shima R.K, Mahmood Almasian, Mohsen Pourkermani., 2015. Review and Analysis of Geological Structural Model by Using Geomagnetic, Case study: Haji Abad Region in Iran's Zagros Zone, Open Jour. of Geology., 5, 39-54.

Sinha-Roy, S., 1995. Continental Crust of North western and central India, Geol. Soc. India. Mem. 31, 63-90.

Sinha-Roy, S, 1998. Proterozoic Wilson cycles in Rajasthan. In: Roy, A.B.(Ed.), Precanbrian of the Aravalli Mountain, Rajasthan, India. Geol. Soc. Ind. Mem., **7**, 95-108.

Spector, A., and Grant, F., 1970. Statistical models for interpreting aeromagnetic data, Geophy., 35, 2, 293-302.

Telford, W.M., Geldart, L.P., and Sheriff, R. E., 1990. Applied geophysics, Cambridge University Press,

Thompson, D.T., 1982. EULDPH: a new technique for making depth estimates from magnetic data., Geophy., 47, 31–37.

Tiwari, H.C., Dixit, M.M., Madhava Rao, N., Venkateshwarlu, N. and Vijaya Rao, V., 1997. Crustal thickening under the Palaeo-meso-Proterozoic Delhi Fold Belt in Northwestern India: evidence from deep reflection profiling., Geophy., J. Int., 129, 657- 668.

Tiwari, H.C, Rao, V.D. et al., 1998. Nagaur-Jhalawar Geotransect across the Delhi Fold Belt in the Northwest India, Jour. Geol. Soc. Ind., 52, 153-161.

Tewari, H.C., Rajendra Prasad, B. and Prakash Kumar., 2018. Structure and Tectonics of the Indian Continental Crust and Its Adjoining Region, Deep Seismic Studies, Second Edition. Elsevier Inc. 57-78. https://doi.org/10.1016/C2016-0-04281-X,

Tweto, Ogden and Sims, P. K., 1968. Precambrian ancestry of the Colorado mineral belt, Geol. Soc. America Bull.,74, 991-1014.

Vacquier, V., Steenland, N.C., Henderson, R.G and Zietz, I., 1951. Interpretation of aeromagnetic maps, Geol. Soc. America. Mem., 47, 151.

Vijaya Rao, V., Rajendra Prasad, B., Reddy, P.R. and Tiwari H.C., 2000. Evolution of Proterozoic Aravlli Delhi Fold Belt in the north western shield from seismic studies, Tectono phy., 327, 109-130.

Received on: 08.02.2022; Revised on: 16.03.2022; Accepted on: 16.04.2022

J. Ind. Geophys. Union, 26(3) (2022) , 182-194

Hydrogeochemical investigations of arsenic-rich groundwater using multivariate statistical analysis

N. M. Refat Nasher[1,2,*] and Sharmin Zaman Emon[3]
[1]Department of Geography and Environment, Jagannath University, Dhaka-1100, Bangladesh
[2]Graduate School of Human Development and Environment, Kobe University, Hyogo-657-0011, Japan
[3]Centre for Advanced Research in Sciences (CARS), University of Dhaka, Dhaka-1000, Bangladesh
*Corresponding author: refat@geography.jnu.ac.bd

ABSTRACT

Multivariate statistical analysis has been applied to assess the chemical characteristics of high arsenic groundwater from central-southern part of Bangladesh. A total of 43 shallow groundwater samples were collected and analyzed. The groundwater is almost neutral. The results of cations and anions trends are Na>Ca>Mg>K and HCO_3>Cl>SO_4>NO_3, respectively. Alkalinity has significant positive correlation with Mg, Ca and K, which suggest silicate weathering as the major processes of controlling groundwater geochemistry. The significant positive correlation between Na and Cl indicates the seawater intrusion into groundwater. R-mode cluster allows variables into four groups. Alkalinity, Mg, K in the first, Ca in the second and Na and Cl in the third cluster, indicate silicate weathering, carbonate dissolution and seawater intrusion, respectively. R-mode factor analysis allows variables into four components having eigen values more than 1 which represent 72.5% of total variances. Component 1 is positively loaded with K, Mg, P and Alkalinity suggesting the silicate weathering. Component 2 positively loaded with Na and Cl, suggests seawater influences into groundwater. Component 3 positively loaded with Ca, suggest the carbonate dissolution. The Q-mode cluster analysis indicates that the as shows highest concentrations with highest Fe concentrations and lowest Mn concentration, suggesting the relatively high anoxic conditions of aquifer.

Key words: Arsenic, Weathering; Dissolution; Principal component analysis (PCA); Hierarchical cluster analysis (HCA), Bangladesh

INTRODUCTION

Bangladesh is rich in surface and groundwater. The microbiological contamination of surface water cause diarrhea among infant; people depend on groundwater for drinking purposes (Mukherjee and Bhattacharya, 2001). Since 1960s, UNICEF installed about 4.5 million shallow tube well in Bangladesh to provide pure drinking water (Black, 1990). After several decades of abstraction, in 1993s the groundwater was chemically tested after observing skin liaison, and As was detected (Chowdhury et al., 1999a). There are several anthropogenic (i,e, wooden pole treated by arsenic, pesticides) and natural sources that are responsible for groundwater As contamination, although anthropogenic sources are not prominent (Survey and Ltd, 1999; Welch et al., 2000). The sedimentary succession during late quaternary to Holocene having fine silt and clay aquifer shows arsenic contaminated groundwater (Bhattacharya et al., 1997). These facies also contain high organic matter (Nickson et al., 1998) with arsenic rich material (Chowdhury et al., 1999b).

The geochemical characteristics of As-rich groundwater in Bangladesh have been studied by various investigators (Nickson et al., 1998; Mukherjee and Bhattacharya, 2001; Swartz et al., 2004). The primary focus of those studies was to explore the sources and mechanisms of arsenic release into groundwater. To reveal the understanding of As release mechanisms and sources, the investigators have analyzed the geochemical properties of As-rich groundwater using dissolution ratios of different elements. These studies primarily focused on dissolution properties, ratios of different elements and some conventional statistical methods. Such methods are widely used to identify the geochemical processes in aquifers (Kumar et al., 2006; Nasher and Ahmed, 2021). There are several suggestions regarding As release mechanisms; Fe-oxyhydroxide reduction (McArthur et al., 2001; Ravenscroft et al., 2005); pyrite oxidation (Chowdhury et al., 1999b); entry of new organic carbon for Fe-oxyhydroxides reduction (Harvey et al., 2002) and silicate weathering (Akai et al., 2004; Shamsudduha et al., 2008) etc.

Multivariate statistical analysis is widely used to study the geochemical properties of groundwater. Factor analysis (FA) and Hierarchical Cluster Analysis (HCA) have been used by various researchers to know the geochemical process in aquifers (Etikala et al., 2019; Igibah and Tanko, 2019; Paul et al., 2019; Umarani et al., 2019; Awomeso et al., 2020; Chai et al., 2020; Elumalai et al., 2020; Nguyen et al., 2020; Panghal and Bhateria, 2020; Ravish et al., 2020; Saleh et al., 2020; Xiang et al., 2020; Farzaneh et al., 2021; Hui et al., 2021; Kale et al., 2021; Sheikhi et al., 2021; Silva et al., 2021; Zahra et al., 2021). These methods have also been used for hydrogeochemical investigations in various regions of Bangladesh (i.e.Molla et al., 2015; Bhuiyan et al., 2016; Islam et al., 2018a,b; Bodrud-Doza et al., 2019;). The high as groundwater (As concentration more than 10 ppb) is considered for the present study. The main objective of this study is to classify the geochemical processes in high as groundwater. Factor Analysis (FA) and Hierarchical Cluster Analysis (HCA) have been used in the analysis of hydro chemical data studying the hydrogeochemical characteristics of groundwater. Both R-mode and Q-mode FA and HCA are applied in this study.

STUDY AREA

The study is confined to Munshiganj district, located in the central southern part of Bangladesh (Figure 1). Munshiganj is situated on the mighty Padma River, 30 km away from the capital of Bangladesh, Dhaka. The subsurface geology of Munshiganj has been studied by Harvey et al. (2002). They found a 100 m of aquifer grey sand (Holocene aquifer) below 3 m surficial clay. A 40 m Pleistocene aquiterd is located below the Holocene aquifer. The aquitered is characterized by marine clay with deep burnt-orange sandy aquifer. This aquifer composed of quartz and feldspar (about 85% by weight).

METHODOLOGY

Forty-three hand held tube well water have been collected randomly from the study area. pH was measured on site using portable meter (PH-6011A CUSTOM). The samples were filtered by 0.45μm cellulose membrane filter and stored in an acid washed 1L polyethylene bottles. The samples were stored in ice state to reduce any biological and chemical transformation. Alkalinity was measured by titration with 0.02N sulfuric acid to 4.8 pH and ionic balance. The anions have been measured by HPLC (Hitachi LaChrome). The cations (Ca, Mg, Na and K) are measured by AAS (Hitach Z-2010) from acidified aliquots. Sr has been used as suppressor for cation measurement. Similarly, the concentrations of Fe, Mn, Ba, Sr, Si, S and P are measured by ICP-OES (SP-100) and arsenic concentrations by hydride generator HYD-10 linked with AAS.

Multivariate statistical approaches are the best technique for interpreting hydrochemical properties with multiple constituents (Eljamassi and El Amassi, 2016). Multivariate statistics techniques have been employed to determine the distinct hydrochemical groups. Factor analysis (FA) and cluster analysis (CA), both multivariate statistical techniques, have been widely used to resolve hydrochemical components (Locsey and Cox, 2003) and identifying geochemical controls (Alberto et al., 2001).

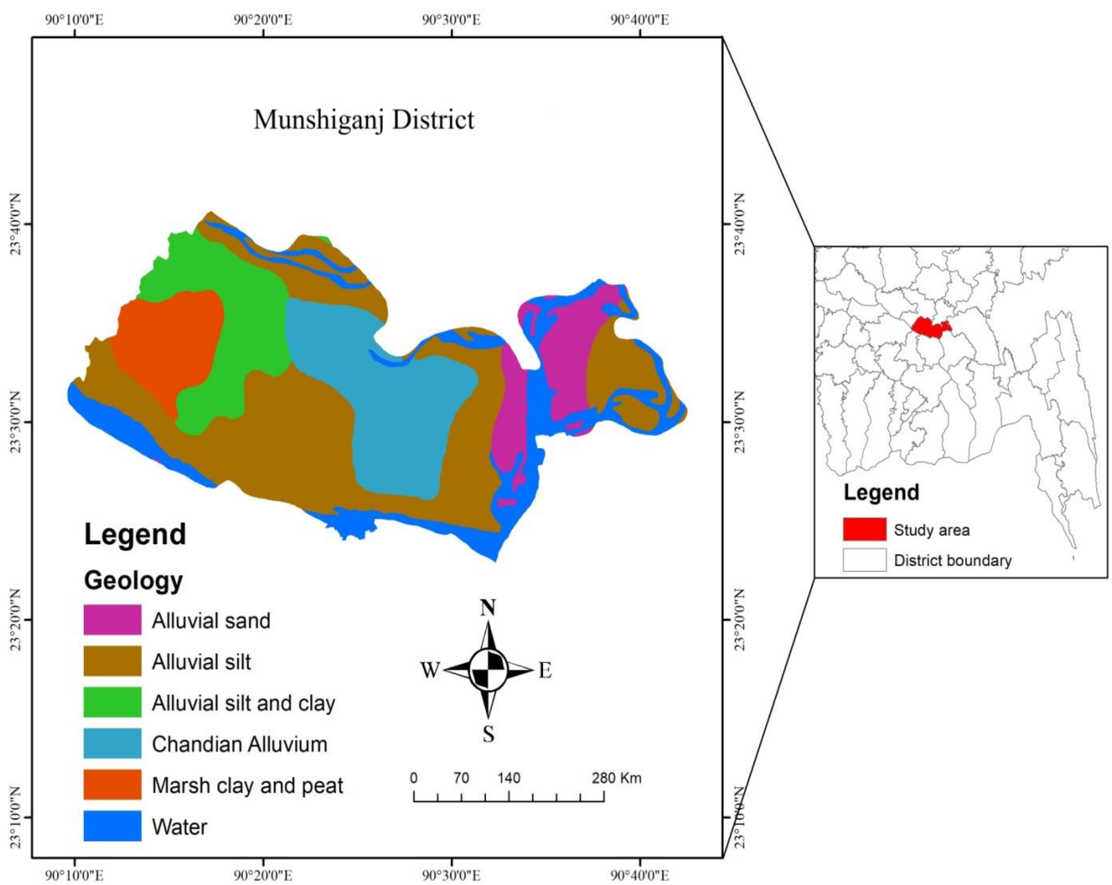

Figure 1. Map of the study area in Munshiganj district of Bangladesh, showing the surficial geology.

RESULTS AND DISCUSSIONS

The statistical summary for all the parameters is presented in Table 1. This data are similar to those of previous studies (Nickson et al., 2000; Anawar et al., 2003; Swartz et al., 2004 ; Shamsudduha et al., 2008; Terakado et al., 2015; Asagoe et al., 2017). The data that have been used in this study are given in Nasher and Terakado (2019). Arsenic concentrations above 10 ppb have been used in the present study. The range of pH is very low (6.92 to 7.24). The groundwater is near neutral in the study area. Alkalinity is relatively high; up to 1195 meq/L. Average sodium (Na) concentration is 89.93 ppm. A few numbers of samples contain relatively high Na concentrations which indicate the seawater influence to groundwater. Average potassium (K) concentration is 4.65 ppm. Magnesium (Mg) concentrations reached up to 49.34 ppm, and the average concentration is 33.42 ppm. Calcium (Ca) concentrations are relatively high in the study area. The highest Ca concentration is 143.38 ppm, and average concentration is 80.42 ppm. Average manganese (Mn) concentration is 0.78 ppm. Iron (Fe) concentrations reached up to 13.39 ppm. Arsenic (As) concentrations are relatively very high up to 711 ppb. Average As concentration is 192.64 ppb. Chloride (Cl) concentrations are relatively high for few samples. These samples indicated the seawater influences into groundwater. Average Cl concentration is 102 ppm. Nitrate (NO3) concentrations are relatively low. Few samples contain relatively high sulphate (SO4) concentration, whereas most of the samples show bellow detection level. Average concentrations of Barium (Ba), Strontium (Sr), Silicon (Si), Sulphur (S) and phosphate (p) are 0.16 ppm, 0.45 ppm, 14.31 ppm, 0.074 ppm and 1.25 ppm, respectively.

Table 2 represents the correlations matrix among the groundwater chemical parameters. pH, NO3 and SO4 have not been considered for correlation analysis due to a smaller number of observations. K, Mg and Ca show significant positive correlation with alkalinity. Na presents significant positive correlation with Cl. K shows significant positive correlation with Mg whereas significant negative correlation with Mn. Ca shows significant positive correlation with Sr. Mn denotes significant positive correlation with Cl whereas significant negative correlation with Fe. Fe shows significant positive correlation with Ba. Arsenic shows no significant correlations with other components. Figure 2 represents the scatter-matrix among the groundwater parameters

Table 1. Statistical summary of groundwater chemical parameters (Nasher and Terakado, 2019).

	N	Minimum	Maximum	Mean	Std. Deviation	Variance	Skewness	Kurtosis
pH	6	6.92	7.24	7.0950	0.13050	0.017	-0.290	-2.068
Alkalinity	27	4.12	11.95	8.1212	1.90766	3.639	0.106	-0.510
Na	27	13.80	401.14	89.9309	96.33244	9279.939	1.991	3.708
K	27	0.84	8.84	4.6586	2.01722	4.069	-0.249	-0.474
Mg	27	19.07	49.34	33.4250	8.08082	65.300	-0.063	-0.799
Ca	27	44.25	143.38	80.4283	25.90714	671.180	0.807	0.462
Mn	27	0.08	2.85	0.7782	0.81031	0.657	1.314	0.633
Fe	27	0.03	13.39	5.9811	3.68064	13.547	0.032	-0.677
As	27	12.37	711.16	192.6377	169.35299	28680.435	1.520	2.355
Cl	27	4.96	582.80	102.0098	162.02003	26250.491	2.116	3.447
NO3	6	0.11	2.70	0.6025	1.02788	1.057	2.436	5.951
SO4	6	0.17	40.10	8.9894	15.63400	244.422	2.196	4.940
Ba	27	0.03	0.33	0.1602	0.08084	0.007	0.233	-0.670
Sr	27	0.242	0.758	0.45136	0.117691	0.014	0.524	0.599
Si	27	7.14	31.11	14.3142	5.62566	31.648	1.647	2.389
S	27	0.02	0.76	0.0738	0.14293	0.020	4.685	23.013
P	27	0.14	4.57	1.2568	1.01022	1.021	1.697	3.746

.

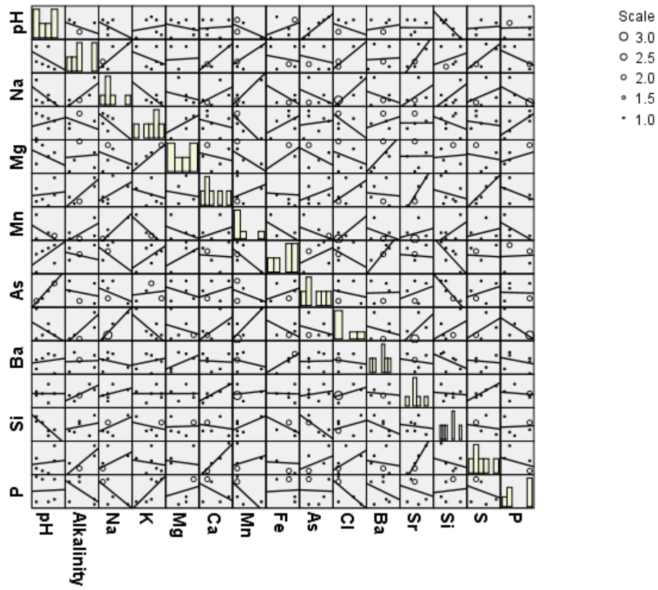

Figure 2. Scatter matrix for groundwater chemical parameters from the studied area in Munshiganj district of Bangladesh.

Table 2. Correlation matrix of Pearson's correlation of coefficient.

	pH	Alkalinity	Na	K	Mg	Ca	Mn	Fe	As	Cl	NO3	SO4	Ba	Sr	Si	S	P
pH	1																
Alkalinity	-0.437	1															
Na	-0.61	-0.115	1														
K	0.213	.528**	-0.156	1													
Mg	-0.306	.552**	0.027	.768**	1												
Ca	0.091	.505**	-0.026	0.167	0.343	1											
Mn	-0.511	-0.28	.499**	-.719**	-0.362	0.067	1										
Fe	0.521	0.3	-0.328	.423*	0.313	0.321	-.585**	1									
As	.948**	0.247	-.404*	0.223	-0.065	.419*	-0.292	0.317	1								
Cl	-0.45	-0.284	.942**	-0.188	0.047	0.108	.519**	-0.26	-0.35	1							
NO_3	.[b]	-0.368	.982**	0.23	0.227	-0.471	.965**	-0.522	-0.689	.984**	1						
SO_4	.[b]	-0.154	-0.332	0.123	0.307	0.238	-0.288	0.307	0.512	-0.227	-0.252	1					
Ba	0.151	0.246	-0.045	.429*	.398*	0.12	-0.299	.571**	0.078	-0.039	-0.671	0.507	1				
Sr	-0.003	.406*	0.289	0.211	0.378	.674**	0.126	0.205	0.09	0.348	0.151	-0.092	0.141	1			
Si	-.935**	-0.183	-0.202	-0.199	-0.222	-.381*	-0.002	-0.155	-0.123	-0.246	-0.432	-0.172	-0.187	-0.328	1		
S	0.095	0	-0.042	0.13	0.185	0.017	-0.177	0.203	0.036	-0.02	-0.05	.996**	0.365	-0.149	-0.128	1	
P	0.033	0.212	-0.32	.453*	0.184	-0.196	-.584**	0.298	-0.083	-.398*	-0.525	0.108	0.307	-0.274	0.069	0.081	1

**. Correlation is significant at the 0.01 level (2-tailed).

*. Correlation is significant at the 0.05 level (2-tailed).

b. Cannot be computed because at least one of the variables is constant.

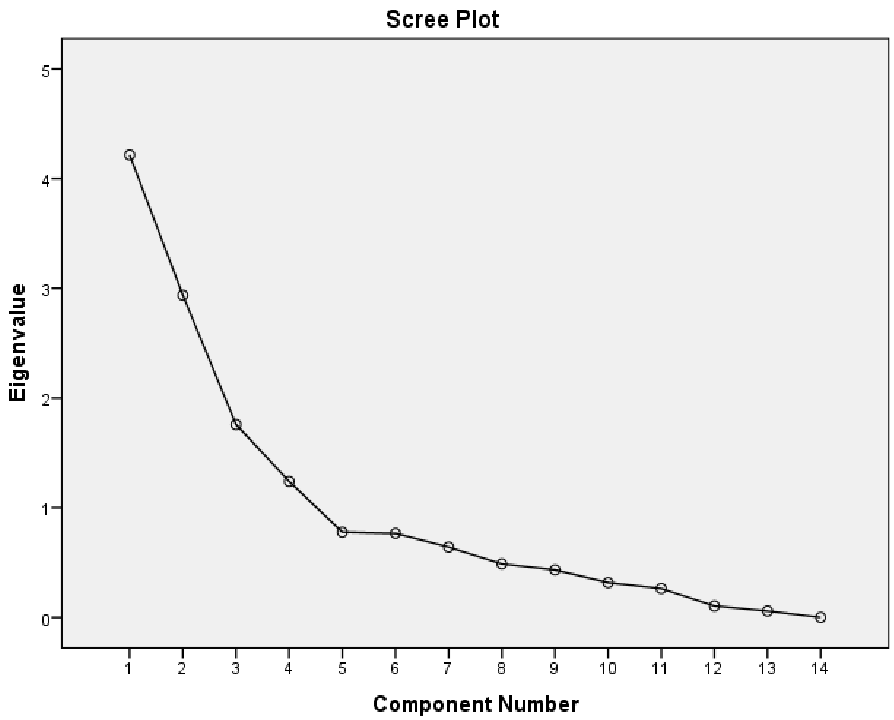

Figure 3. Scree plot showing eigen values.

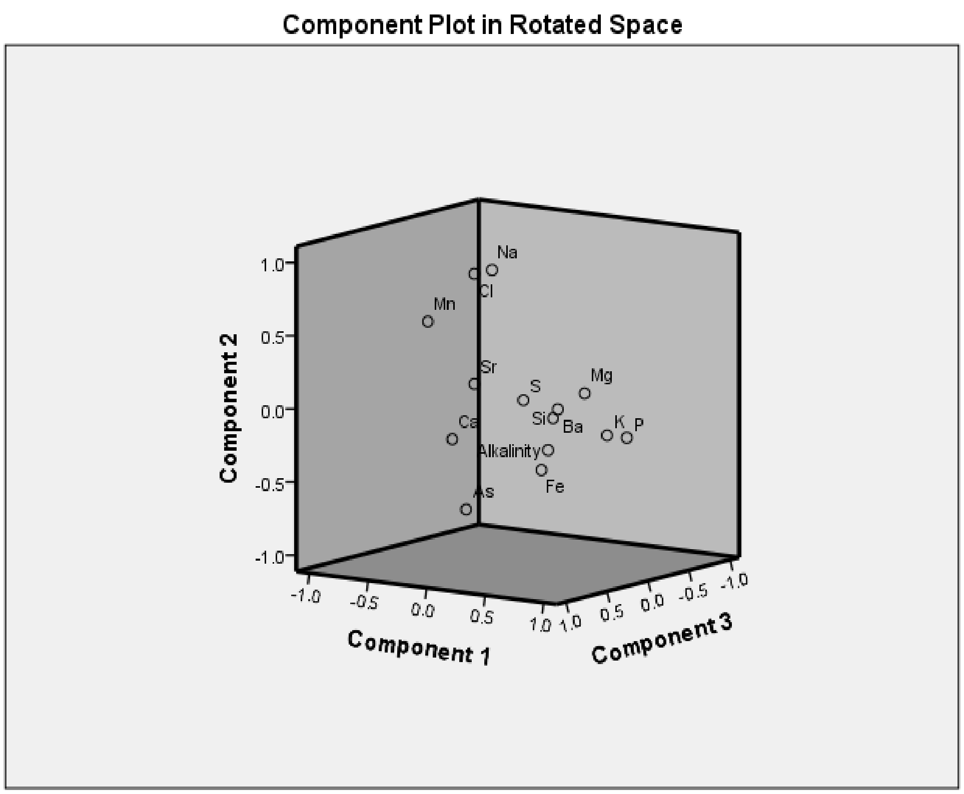

Figure 4. Component plot in rotate space for groundwater geochemical parameters.

Table 3. Factor analysis of groundwater parameters

Component	Initial Eigenvalues			Extraction sums of squared loadings			Rotation sums of squared loadings		
	Total	% of Variance	Cumulative %	Total	% of Variance	Cumulative %	Total	% of Variance	Cumulative %
1	4.21	30.11	30.11	4.216	30.11	30.11	3.02	21.57	21.57
2	2.93	20.97	51.08	2.93	20.97	51.08	2.75	19.64	41.21
3	1.75	12.56	63.65	1.75	12.56	63.65	2.67	19.11	60.33
4	1.23	8.85	72.50	1.23	8.85	72.50	1.70	12.17	72.50
5	.77	5.55	78.05						
6	.76	5.47	83.53						
7	.64	4.58	88.11						
8	.48	3.48	91.59						
9	.43	3.09	94.69						
10	.31	2.26	96.95						
11	.26	1.88	98.83						
12	.10	.74	99.58						
13	.05	.41	100.00						
14	3.84E-5	.00	100.00						
Extraction Method: Principal Component Analysis.									

Factor Analysis (FA)

Table 3 represents the results of factor analysis using principal components and varimax rotation (Gotelli and Ellison, 2004). The Kaiser criterion has been applied for principal component analysis (Kaiser, 1960), thus the eigenvalues greater than 1 have been included for factor analysis. The positive and negative score in PCA indicate the significant control of water quality by that parameter (Bhuiyan et al., 2010). The scree plot shows the structures of the factors (Figure 3). Four components have been accounted from R-mode factor analysis. The component plot of rotated space is presented in Figure 4. These four components comprise for 72.5% of the total variance in the hydrochemistry in the present study. The loaded elements in the first component generally control the hydrochemistry of the groundwater (Yidana et al., 2010). The first component accounted for 30.1% of total variance and eigenvalue of 4.2. Alkalinity, K, Fe and Mg have positively loaded for component 1. Component 2 accounts for 20.9% of total variance with eigenvalue of 2.9. Highly positive loading elements are Sr, Na, Cl and Ca. There is no highly loading element for component 3 which accounts for 12.5% of the total variables with 1.76 eigenvalue. Sulfur is highly loaded element in component 4. This factor accounts for 8.85% of the total variance with 1.24 eigenvalue.

The four components resulted from the R-mode factor analysis presented in Table 4. K, alkalinity, Fe, and Mg are positively correlated in component 1. Alkalinity and Fe have different sources in Bangladesh groundwater (Nasher and Terakado, 2019). The sources of alkalinity are carbonate weathering, reverse ion exchange or from microbial activities (Bahar and Reza, 2010). The sources of Fe in groundwater are reduction of Fe-oxyhydroxides (Nickson et al., 2000; Anawar et al., 2002) . Component one represents the silicate weathering in the aquifers (Mackenzie and Garrels, 1965; Stallard and Edmond, 1983; Datta and Tyagi, 1996; Nosrati and Van Den Eeckhaut, 2012; Nasher and Ahmed, 2021)). The second component correlates positively with Sr, Na, Cl and Ca. This is the mixed processes, probably represents the seawater influences (Cloutier et al., 2006) and/or anthropogenic pollution into groundwater (Yidana, 2010). The strong positive significant correlation suggests seawater intrusion. The excess Na over Cl concentrations probably come from silicate weathering (Stallard and Edmond, 1983; Meybeck, 1987; Selvam et al., 2016) and the concentrations of Cl over Na probably introduce by anthropogenic imputes (Jiang et al., 2009; Valdes et al., 2007) or by cation exchanges processes (Kumar, 2014; Yidana, 2010). The result of Q-mode factor analysis presented in Table 5.

Table 4. Extracted components from factor analysis.

	Component			
	1	2	3	4
K	.821	.122	.270	-.265
Mn	-.785	.373	-.143	.061
Fe	.733	.027	-.022	.317
Alkalinity	.651	.313	-.191	-.356
Mg	.644	.421	.322	-.286
Ba	.579	.151	.387	.386
P	.520	-.434	.392	-.210
Sr	.212	.802	-.235	-.156
Cl	-.491	.712	.372	.080
Na	-.484	.660	.439	-.045
Ca	.374	.644	-.516	.080
Si	-.213	-.541	-.001	-.282
As	.418	-.043	-.669	.295
S	.253	-.015	.349	.676

Extraction Method: Principal Component Analysis.

Table 5. Q-mode factor analysis.

	Component			
	1	2	3	4
Sample 1	.969	.220	-.087	.028
Sample 2	.944	.280	-.128	-.113
Sample 3	.982	-.177	.019	.051
Sample 4	.463	.575	.567	.363
Sample 5	.509	.406	.724	.208
Sample 6	.926	-.371	-.043	.044
Sample 7	.986	.053	-.128	.084
Sample 8	.971	.020	-.169	.165
Sample 9	.924	-.364	-.101	.058
Sample 10	.281	.896	-.340	-.014
Sample 11	.934	-.344	.002	.066
Sample 12	.522	.791	-.174	.264
Sample 13	.901	-.398	-.161	.050
Sample 14	.964	-.152	.161	.138
Sample 15	.360	.855	-.359	.097
Sample 16	.417	.847	-.325	.048
Sample 17	.732	.291	.585	-.143
Sample 18	.961	-.271	.006	-.044
Sample 19	.836	.184	.387	-.329
Sample 20	.734	.475	-.018	-.482
Sample 21	.870	.437	-.203	-.093
Sample 22	.869	.322	.207	-.274
Sample 23	.927	-.343	.071	.017
Sample 24	.925	-.359	.055	.028
Sample 25	.867	-.459	-.194	.023
Sample 26	.910	-.392	-.131	.026
Sample 27	.885	-.431	-.177	.001

Extraction Method: Principal Component Analysis.

Hierarchical Cluster Analysis (HCA)

The Hierarchical Cluster Analysis (HCA) is widely employed in earth science for clustering cases or variables (Davis and Sampson, 1986), specifically hydrogeochemical data clustering (Güler et al., 2002). Ward's cluster methods have been used for HCA in this study. Ward's method resulted the best combination for clustering in HCA for hydro-chemical data (Cloutier et al., 2008). The Q-mode HCA is used to classify the samples into different groups. The resulted dendrogram visually represents six classes from 27 samples (Figure 5). The basic statistical summary presents in Table 6. Cluster 1 and 2 include the samples 23, 24, 14, 11, 18, 7, 8, 3, 6 and samples 5, 17, 4, 1, 2, 19, 22, 20, respectively. The mean for most of the parameters of these two clusters are almost similar. Therefore, the geochemical properties of these two clusters are also similar. The chemical properties suggest a combination of various geochemical processes instead of single processes controlling the geochemistry of groundwater. Cluster 3 (sample 12 and 21) has moderate Na, Cl and Ca concentrations. Such moderate cation concentrations suggest the silicate weathering. Cluster 4 (sample 25, 26, 9, 27) has the highest As and Fe concentrations with lowest Mn concentration. Fe and Mn have insignificant correlation with As. Such conditions probably suggest the relatively high reducing conditions in the aquifer, where the Fe-oxyhydroxides have been started to dissolute and release Fe and As into groundwater (Nickson et al., 2000). Cluster 5 has only one sample (sample 13). This sample contains highest As concentrations which is probably an outlier. Cluster 6 (sample 15, 16, 10) has the highest mean for Na and Cl concentration. This cluster of samples is influenced by seawater intrusion.

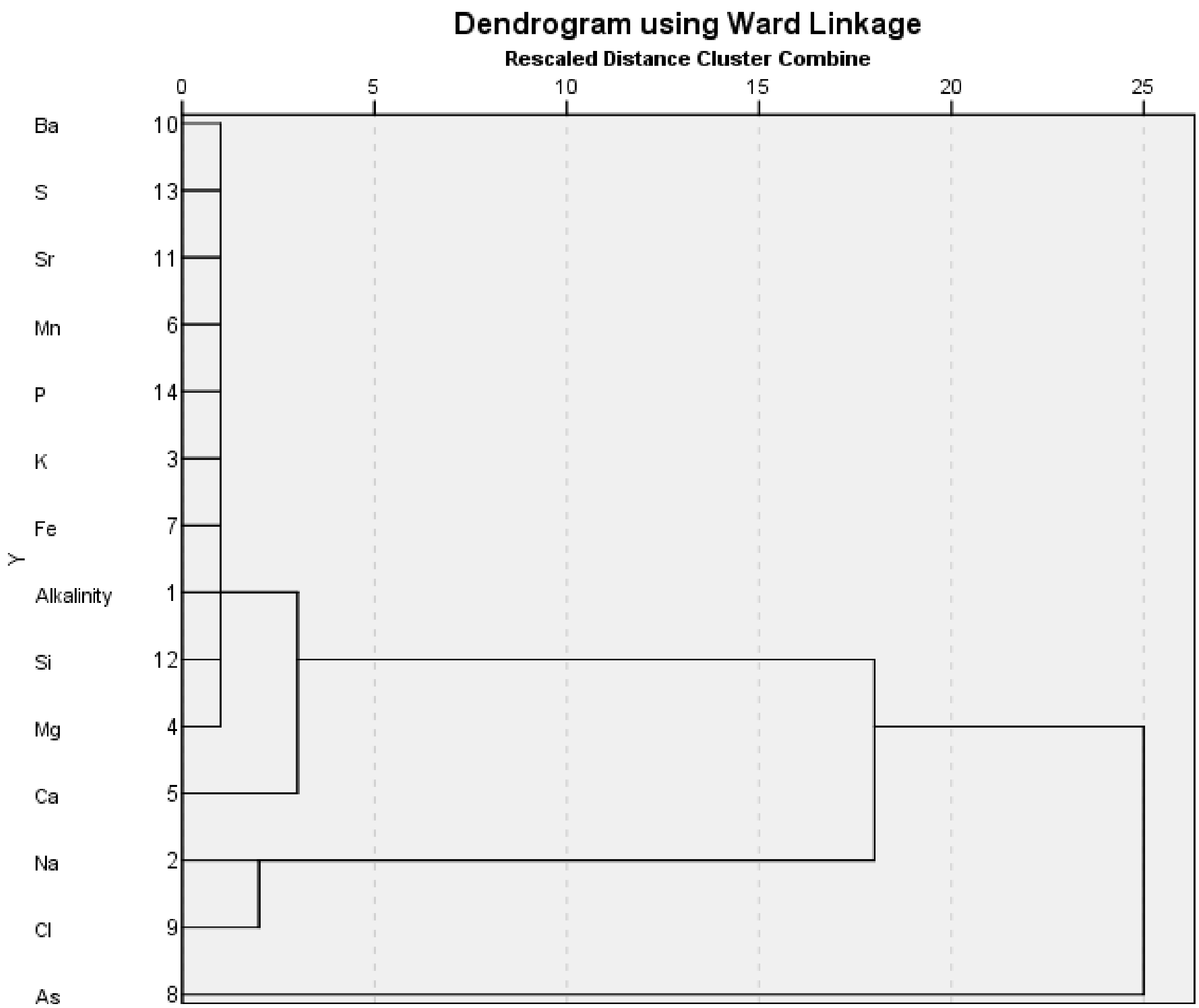

Figure 5. Q-mode Hierarchical cluster analysis showing four separate clusters of geochemical parameters.

Table 6. Q-mode cluster analysis of geochemical parameters.

	Minimum					Maximum					Mean					Std. Deviation				
	cluster1	cluster 2	cluster 3	cluster 4	cluster 6	cluster 1	cluster 2	cluster 3	cluster 4	cluster 6	cluster1	cluster 2	cluster 3	cluster 4	cluster 6	cluster 1	cluster 2	cluster 3	cluster 4	cluster 6
pH	6.98	6.92		7.18		7.05	6.92		7.24		7.02	6.92		7.21		0.05	.		0.03	
Alkalinity	5.85	6.09	8.67	5.75	4.12	10.76	11.95	10.54	10.07	7.28	8.00	8.42	9.60	7.85	6.10	1.34	2.11	1.32	2.27	1.73
Na	20.58	24.88	151.60	13.80	281.17	76.90	147.69	170.50	42.93	401.14	40.99	76.21	161.05	28.55	324.11	21.20	42.95	13.36	12.66	66.86
K	1.89	1.16	4.68	3.16	0.84	6.92	8.84	6.27	6.52	7.14	5.17	4.21	5.47	4.83	3.11	1.70	2.29	1.13	1.38	3.49
Mg	19.07	22.83	35.82	20.25	24.02	41.69	49.34	46.60	38.97	42.52	35.92	30.86	41.21	30.87	31.11	6.78	9.32	7.62	8.01	9.98
Ca	52.37	44.25	86.63	47.37	57.31	106.21	103.04	140.12	108.40	86.98	78.95	67.77	113.37	81.18	74.67	18.51	19.70	37.83	29.14	15.46
	0.08	0.11	0.65	0.21	0.72	1.63	2.34	1.56	0.65	2.85	0.47	0.81	1.11	0.37	1.96	0.53	0.92	0.65	0.20	1.11
Fe	0.75	0.03	3.30	3.69	0.77	13.39	12.64	7.78	9.91	8.56	6.62	4.97	5.54	7.91	3.75	3.57	4.37	3.16	2.86	4.21
As	140.83	12.37	82.90	336.34	13.08	268.39	125.47	187.21	507.25	76.69	198.28	69.84	135.06	431.53	50.19	46.34	45.32	73.76	83.51	33.10
Cl	4.96	9.01	162.05	5.22	432.19	114.79	74.49	318.40	27.44	582.80	35.74	40.31	240.22	15.62	509.45	41.50	26.10	110.55	10.30	75.38
NO3	0.15	0.11			2.70	0.24	0.19			2.70	0.21	0.15			2.70	0.05	0.05			.
SO4	0.23	0.17			4.12	40.10	9.05			4.12	20.17	3.16			4.12	28.19	5.10			.
Ba	0.03	0.03	0.06	0.06	0.12	0.33	0.29	0.12	0.19	0.24	0.18	0.16	0.09	0.15	0.17	0.09	0.10	0.04	0.06	0.06
Sr	0.31	0.24	0.66	0.28	0.44	0.57	0.56	0.76	0.51	0.55	0.44	0.40	0.71	0.40	0.49	0.09	0.10	0.07	0.10	0.06
Si	8.38	11.30	10.95	10.35	10.66	25.87	31.11	10.98	19.03	13.06	14.66	16.03	10.96	15.49	11.75	6.37	6.82	0.02	3.91	1.21
S	0.03	0.02	0.04	0.02	0.03	0.76	0.18	0.06	0.05	0.16	0.12	0.05	0.05	0.04	0.08	0.24	0.05	0.01	0.01	0.07
P	0.27	0.20	0.14	0.84	0.17	2.36	4.57	1.22	1.72	0.75	1.24	1.81	0.68	1.27	0.43	0.66	1.52	0.76	0.43	0.30

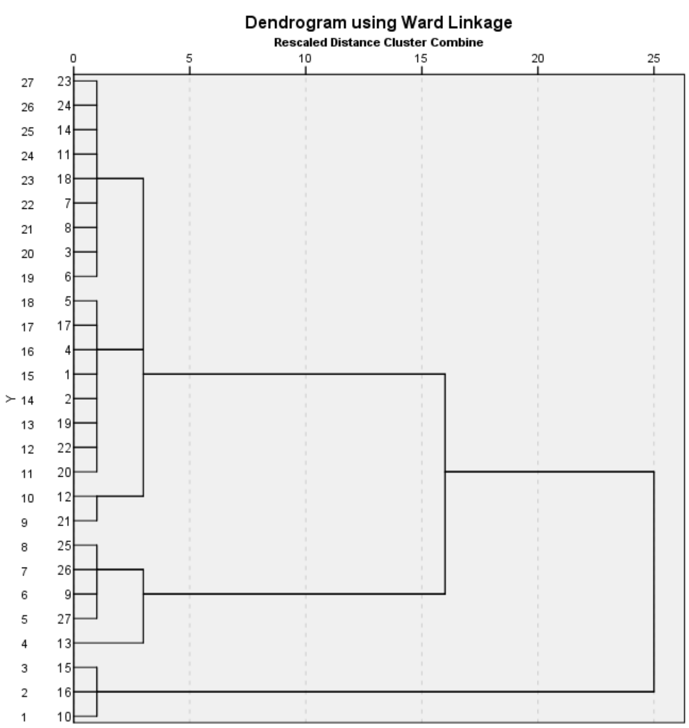

Figure 6. R-mode cluster analysis separating the total 27 samples into six different groups.

The R-mode cluster analysis is used to classify variables into possible similar groups. There are four groups that are identified by R-mode HCA (Figure 6). The first cluster is highly correlated with Ba, S, Sr, Mn, P, K, Fe, Alkalinity, Si and Mg. This group is probably corresponding to the component 1, although Mn shows highly negative loading in factor 1 and Sr shows high positive loading in component 2. This cluster is probably associated with silicate weathering (Mackenzie and Garrels, 1965). The second cluster have only one element; Ca. The primary source of Ca in groundwater is carbonate weathering (Nasher and Ahmed, 2021). Cluster 3 comprises with Na and Cl. Combination of different geochemical processes with anthropogenic imputes.

CONCLUSIONS

The chemical properties of arsenic-rich groundwater are controlled by various geochemical processes. Silicate weathering, carbonate dissolution, seawater intrusion, ion exchange are the prominent geochemical processes in high-As groundwater. Arsenic does not load significantly from any of four components from factor analysis. Although, arsenic is loaded with K, Fe alkalinity and Mg. The R-mode cluster analysis represents six clusters where arsenic showed highest concentration with Fe concentration. Arsenic is linked with high alkalinity and Fe concentrations. The Fe-oxyhydroxides reduction control Fe and As concentrations in the study area. The nitrate and sulfates are also important in As-rich groundwater study; however, these two are excluded in FA and HCA. Q-mode cluster analysis showed four major groups of geochemical processes. The first two groups indicated combination of various geochemical processes. The third group specified the silicate weathering of the groundwater aquifers. The forth group showed higher concentration of As and Fe. Such relatively high concentrations of As and Fe suggest reducing condition of the aquifers which controlled the dissolved arsenic in the study area.

ACKNOWLEDGEMENTS

I am extremely grateful to my supervisor Professor Yasutaka Terakado for his enormous support for analyzing and understanding groundwater geochemistry. Special thanks to the reviewers for their comments and suggestion to improve the quality of the manuscript. I am thankful to the editor for considering my work to publish.

Compliance with Ethical Standards

The authors declare no conflict of interest and adhere to copyright norms.

REFERENCES

Akai, J., Izumi, K., Fukuhara, H., Masuda, H., Nakano, S., Yoshimura, T., Ohfuji, H., Anawar, H.M. and Akai, K., 2004. Mineralogical and geomicrobiological investigations on groundwater arsenic enrichment in Bangladesh. Appl. Geochem., 19, 215–230.

Alberto, W.D., del Pilar, D.M., Valeria, A.M., Fabiana, P.S., Cecilia, H.A. and de Los Ángeles, B.M., 2001. Pattern recognition techniques for the evaluation of spatial and temporal variations in water quality. a case study:: Suquía River Basin (Córdoba–Argentina). Water Res., 35, 2881–2894.

Anawar, H., Komaki, K., Akai, J., Takada, J., Ishizuka, T., Takahashi, T., Yoshioka, T. and Kato, K., 2002. Diagenetic control on arsenic partitioning in sediments of the Meghna River delta, Bangladesh. Environ. Geol., 41, 816–825.

Anawar, H.M., Akai, J., Komaki, K., Terao, H., Yoshioka, T., Ishizuka, T., Safiullah, S. and Kato, K., 2003. Geochemical occurrence of arsenic in groundwater of Bangladesh: sources and mobilization processes. J. Geochem. Explor., 77, 109–131.

Asagoe, Y., Terakado, Y., Kishibe, K. and Nasher, N., 2017. Geochemical study of major and trace elements in the arsenic contaminated groundwaters in Bangladesh. 神戸大学大学院人間発達環境学研究科研究紀要 10, 141–149.

Awomeso, J.A., Ahmad, S.M. and Taiwo, A.M., 2020. Multivariate assessment of groundwater quality in the basement rocks of Osun State, Southwest, Nigeria. Environ. Earth Sci., 79, 1–9.

Bahar, M.M. and Reza, M.S., 2010. Hydrochemical characteristics and quality assessment of shallow groundwater in a coastal area of Southwest Bangladesh. Environ. Earth Sci. 61, 1065–1073.

Bhattacharya, P., Chatterjee, D. and Jacks, G., 1997. Occurrence of arsenic-contaminatedgroundwater in alluvial aquifers from delta plains, eastern India: Options for safe drinking water supply. Int. J. Water Resour. Dev., 13, 79–92.

Bhuiyan, M.A.H., Islam, M.A., Dampare, S.B., Parvez, L. and Suzuki, S., 2010. Evaluation of hazardous metal pollution in irrigation and drinking water systems in the vicinity of a coal mine area of northwestern Bangladesh. J. Hazard. Mater., 179, 1065–1077. https://doi.org/10.1016/j.jhazmat.2010.03.114

Bhuiyan, M.A.H., Bodrud-Doza, M., Islam, A.T., Rakib, M.A., Rahman, M.S. and Ramanathan, A.L., 2016. Assessment of groundwater quality of Lakshimpur district of Bangladesh using water quality indices, geostatistical methods, and multivariate analysis. Environ. Earth Sci., 75, 1–23.

Black, M., 1990. From handpumps to health: the evolution of water and sanitation programmes in Bangladesh, India and Nigeria. United Nations Children's Fund.

Bodrud-Doza, M., Bhuiyan, M.A.H., Islam, S.D.U., Rahman, M.S., Haque, M.M., Fatema, K.J., Ahmed, N., Rakib, M.A. and Rahman, M.A., 2019. Hydrogeochemical investigation of groundwater in Dhaka City of Bangladesh using GIS and multivariate statistical techniques. Groundw. Sustain. Dev., 8, 226–244.

Chai, Y., Xiao, C., Li, M. and Liang, X., 2020. Hydrogeochemical Characteristics and Groundwater Quality Evaluation Based on Multivariate Statistical Analysis. Water, 12, 2792.

Chowdhury, T. R., Biswas, B.K., Chowdhury, U.K., Samanta, G., Mandal, B.K. and Chakraborti, D., 1999a. Toxicological effects of geogenic contamination with special reference to arsenic, in: Abstract Volume of Abstracts. 2nd International Conference on Contaminants in the Soil Environment in the Australasia. 12–17.

Chowdhury, T. R., Basu, G.K., Mandal, B.K., Biswas, B.K., Samanta, G., Chowdhury, U.K., Chanda, C.R., Lodh, D., Roy, S.L. and Saha, K.C., 1999b. Arsenic poisoning in the Ganges delta. Nature, 401, 545–546.

Cloutier, V., Lefebvre, R., Savard, M.M., Bourque, É. and Therrien, R., 2006. Hydrogeochemistry and groundwater origin of the Basses-Laurentides sedimentary rock aquifer system, St. Lawrence Lowlands, Québec, Canada. Hydrogeol. J., 14, 573–590.

Cloutier, V., Lefebvre, R., Therrien, R. and Savard, M.M., 2008. Multivariate statistical analysis of geochemical data as indicative of the hydrogeochemical evolution of groundwater in a sedimentary rock aquifer system. J. Hydrol., 353, 294–313.

Datta, P.S. and Tyagi, S.K., 1996. Major ion chemistry of groundwater in Delhi area: chemical weathering processes and groundwater flow regime. J. Geol. Soc. India, 47, 179–188.

Davis, J.C. and Sampson, R.J., 1986. Statistics and data analysis in geology. Wiley New York.

Eljamassi, A. and El Amassi, K., 2016. Assessment of groundwater quality using multivariate and spatial analysis in Gaza, Palestine.

Elumalai, V., Nethononda, V.G., Manivannan, V., Rajmohan, N., Li, P. and Elango, L., 2020. Groundwater quality assessment and application of multivariate statistical analysis in Luvuvhu catchment, Limpopo, South Africa. J. Afr. Earth Sci., 171, 103967.

Etikala, B., Golla, V., Adimalla, N. and Marapatla, S., 2019. Factors controlling groundwater chemistry of Renigunta area, Chittoor District, Andhra Pradesh, South India: a multivariate statistical approach. Hydro Research, 1, 57–62.

Farzaneh, G., Khorasani, N., Ghodousi, J. and Panahi, M., 2021. Assessment of Surface and Groundwater Resources Quality Close to Municipal Solid Waste Landfill Using Multiple Indicators and Multivariate Statistical Methods. Int. J. Environ. Res., 15, 383–394.

Gotelli, N.J. and Ellison, A.M., 2004. A primer of ecological statistics. Sinauer Associates Sunderland.

Güler, C., Thyne, G.D., McCray, J.E. and Turner, K.A., 2002. Evaluation of graphical and multivariate statistical methods for classification of water chemistry data. Hydrogeol. J., 10, 455–474.

Harvey, C.F., Swartz, C.H., Badruzzaman, A.B.M., Keon-Blute, N., Yu, W., Ali, M.A., Jay, J., Beckie, R., Niedan, V., and Brabander, D., 2002. Arsenic mobility and groundwater extraction in Bangladesh. Science, 298, 1602–1606.

Hui, T., Jizhong, D., Shimin, M., Zhuang, K. and Yan, G., 2021. Application of water quality index and multivariate statistical analysis in the hydrogeochemical assessment of shallow groundwater in Hailun, northeast China. Hum. Ecol. Risk Assess. Int. J., 27, 651–667.

Igibah, C.E. and Tanko, J.A., 2019. Assessment of urban groundwater quality using Piper trilinear and multivariate techniques: a case study in the Abuja, North-central, Nigeria. Environ. Syst. Res., 8, 1–14.

Islam, A.T., Shen, S., Haque, M.A., Bodrud-Doza, M., Maw, K.W. and Habib, M.A., 2018a. Assessing groundwater quality and its sustainability in Joypurhat district of Bangladesh using GIS and multivariate statistical approaches. Environ. Dev. Sustain., 20, 1935–1959.

Islam, M.A., Rahman, M.M., Bodrud-Doza, M., Muhib, M.I., Shammi, M., Zahid, A., Akter, Y. and Kurasaki, M., 2018b. A study of groundwater irrigation water quality in south-central Bangladesh: a geo-statistical model approach using GIS and multivariate statistics. Acta Geochim., 37, 193–214.

Jiang, Y., Wu, Y., Groves, C., Yuan, D and, Kambesis, P., 2009. Natural and anthropogenic factors affecting the groundwater quality in the Nandong karst underground river system in Yunan, China. J. Contam. Hydrol., 109, 49–61. https://doi.org/10.1016/j.jconhyd.2009.08.001

Kaiser, H.F., 1960. The application of electronic computers to factor analysis. Educ. Psychol. Meas., 20, 141–151.

Kale, A., Bandela, N., Kulkarni, J., Sahoo, S.K. and Kumar, A., 2021. Hydrogeochemistry and multivariate statistical analysis of groundwater quality of hard rock aquifers from Deccan trap basalt in Western India. Environ. Earth Sci., 80, 1–24.

Kumar, M., Ramanathan, A.L., Rao, M.S. and Kumar, B., 2006. Identification and evaluation of hydrogeochemical processes in the groundwater environment of Delhi, India. Environ. Geol., 50, 1025–1039.

Kumar, P.J.S., 2014. Evolution of groundwater chemistry in and around Vaniyambadi Industrial Area: Differentiating the natural and anthropogenic sources of contamination. Geochemistry, 74, 641–651. https://doi.org/10.1016/j.chemer.2014.02.002

Locsey, K.L. and Cox, M.E., 2003. Statistical and hydrochemical methods to compare basalt-and basement rock-hosted groundwaters: Atherton Tablelands, north-eastern Australia. Environ. Geol., 43, 698–713.

Mackenzie, F.T. and Garrels, R.M., 1965. Silicates: reactivity with sea water. Science, 150, 57–58.

McArthur, J.M., Ravenscroft, P., Safiulla, S. and Thirlwall, M.F., 2001. Arsenic in groundwater: testing pollution mechanisms for sedimentary aquifers in Bangladesh. Water Resour. Res., 37, 109–117.

Meybeck, M., 1987. Global chemical weathering of surficial rocks estimated from river dissolved loads. Am. J. Sci., 287, 401. https://doi.org/10.2475/ajs.287.5.401

Molla, M.M.A., Saha, N., Salam, S.M.A. and Rakib-uz-Zaman, M., 2015. Surface and groundwater quality assessment based on multivariate statistical techniques in the vicinity of Mohanpur, Bangladesh. Int. J. Environ. Health Eng., 4, 18.

Mukherjee, A.B. and Bhattacharya, P., 2001. Arsenic in groundwater in the Bengal Delta Plain: slow poisoning in Bangladesh. Environ. Rev., 9, 189–220.

Nasher, N.M. and Terakado, Y., 2019. Sources of some major and minor elements in arsenic-rich groundwaters of Bangladesh. 神戸大学大学院人間発達環境学研究科研究紀要 12, 113–120.

Nasher, N.R. and Ahmed, M.H., 2021. Groundwater geochemistry and hydrogeochemical processes in the Lower Ganges-Brahmaputra-Meghna River Basin areas, Bangladesh. J. Asian Earth Sci., X 100062.

Nguyen, B.T., Nguyen, T.M.T. and Bach, Q.V., 2020. Assessment of groundwater quality based on principal component analysis and pollution source-based examination: a case study in Ho Chi Minh City, Vietnam. Environ. Monit. Assess., 192, 1–13.

Nickson, R., McArthur, J., Burgess, W., Ahmed, K.M., Ravenscroft, P. and Rahmann, M., 1998. Arsenic poisoning of Bangladesh groundwater. Nature, 395, 338–338.

Nickson, R.T., McArthur, J.M., Ravenscroft, P., Burgess, W.G. and Ahmed, K.M., 2000. Mechanism of arsenic release to groundwater, Bangladesh and West Bengal. Appl. Geochem., 15, 403–413.

Nosrati, K. and Van Den Eeckhaut, M., 2012. Assessment of groundwater quality using multivariate statistical techniques in Hashtgerd Plain, Iran. Environ. Earth Sci., 65, 331–344.

Panghal, V. and Bhateria, R., 2020. A multivariate statistical approach for monitoring of groundwater quality: a case study of Beri block, Haryana, India. Environ. Geochem. Health, 1–15.

Paul, R., Brindha, K., Gowrisankar, G., Tan, M.L. and Singh, M.K., 2019. Identification of hydrogeochemical processes controlling groundwater quality in Tripura, Northeast India using evaluation indices, GIS, and multivariate statistical methods. Environ. Earth Sci., 78, 1–16.

Ravenscroft, P., Burgess, W.G., Ahmed, K.M., Burren, M. and Perrin, J., 2005. Arsenic in groundwater of the Bengal Basin, Bangladesh: distribution, field relations, and hydrogeological setting. Hydrogeol. J., 13, 727–751.

Ravish, S., Setia, B. and Deswal, S., 2020. Groundwater Quality Analysis of Northeastern Haryana using Multivariate Statistical Techniques. J. Geol. Soc. India, 95, 407-416.

Saleh, H.N., Valipoor, S., Zarei, A., Yousefi, M., Asghari, F.B., Mohammadi, A.A., Amiri, F., Ghalehaskar, S., and Khaneghah, A.M., 2020. Assessment of groundwater quality around municipal solid waste landfill by using Water Quality Index for groundwater resources and multivariate statistical technique: a case study of the landfill site, Qaem Shahr City, Iran. Environ. Geochem. Health, 42, 1305–1319.

Selvam, S., Venkatramanan, S., Chung, S.Y. and Singaraja, C., 2016. Identification of groundwater contamination sources in Dindugal district of Tamil Nadu, India using GIS and multivariate statistical analyses. Arab. J. Geosci., 9, 407.

Shamsudduha, M., Uddin, A., Saunders, J.A., and bLee, M.K., 2008. Quaternary stratigraphy, sediment characteristics and geochemistry of arsenic-contaminated alluvial aquifers in the Ganges–Brahmaputra floodplain in central Bangladesh. J. Contam. Hydrol., 99, 112–136.

Sheikhi, S., Faraji, Z. and Aslani, H., 2021. Arsenic health risk assessment and the evaluation of groundwater quality using GWQI and multivariate statistical analysis in rural areas, Hashtroud, Iran. Environ. Sci. Pollut. Res., 28, 3617–3631.

Silva, M.I., Gonçalves, A.M.L., Lopes, W.A., Lima, M.T.V., Costa, C.T.F., Paris, M., Firmino, P.R.A. and De Paula Filho, F.J., 2021. Assessment of groundwater quality in a Brazilian semiarid basin using an integration of GIS, water quality index and multivariate statistical techniques. J. Hydrol., 598, 126346.

Stallard, R.F. and Edmond, J.M., 1983. Geochemistry of the Amazon: 2. The influence of geology and weathering environment on the dissolved load. J. Geophys. Res. Oceans, 88, 9671–9688.

Survey, B.G. and Ltd, M.M.I., 1999. Groundwater Studies for Arsenic Contamination in Bangladesh: Phase I: Rapid Investigation Phase, Final Report. British Geological Survey.

Swartz, C.H., Blute, N.K., Badruzzman, B., Ali, A., Brabander, D., Jay, J., Besancon, J., Islam, S., Hemond, H.F. and Harvey, C.F., 2004. Mobility of arsenic in a Bangladesh aquifer: Inferences from geochemical profiles, leaching data, and mineralogical characterization. Geochim. Cosmochim. Acta, 68, 4539–4557.

Terakado, Y., Asagoe, Y., KogA, T. and NM, R., 2015. Preliminary report on arsenic and some related components in tube-well waters from the high and low arsenic groundwater areas near Dhaka, Bangladesh. Bull. Grad. Sch. Hum. Dev. Environ., Kobe Univ. 9, 73–80.

Umarani, P., Ramu, A. and Kumar, V., 2019. Hydrochemical and statistical evaluation of groundwater quality in coastal aquifers in Tamil Nadu, India. Environ. Earth Sci., 78, 1–14.

Valdes, D., Dupont, J.-P., Laignel, B., Ogier, S., Leboulanger, T. and Mahler, B.J., 2007. A spatial analysis of structural controls on Karst groundwater geochemistry at a regional scale. J. Hydrol., 340, 244–255. https://doi.org/10.1016/j.jhydrol.2007.04.014

Welch, A.H., Westjohn, D.B., Helsel, D.R. and Wanty, R.B., 2000. Arsenic in ground water of the United States: occurrence and geochemistry. Groundwater, 38, 589–604.

Xiang, J., Zhou, J., Yang, J., Huang, M., Feng, W., Li, Q., Xue, D., Zhao, Y. and Zhu, G., 2020. Applying multivariate statistics for identification of groundwater chemistry and qualities in the Sugan Lake Basin, Northern Qinghai-Tibet Plateau, China. J. Mt. Sci., 17, 448–463.

Yidana, S.M., 2010. Groundwater classification using multivariate statistical methods: Southern Ghana. J. Afr. Earth Sci., 57, 455–469.

Yidana, S.M., Banoeng-Yakubo, B. and Akabzaa, T.M., 2010. Analysis of groundwater quality using multivariate and spatial analyses in the Keta basin, Ghana. J. Afr. Earth Sci., 58, 220–234.

Zahra, T., Tiwari, A.K., Chauhan, M.S. and Singh, D., 2021. Evaluation of Groundwater Quality Using Multivariate Analysis: Rae Bareli District, Ganga Basin, Uttar Pradesh, in: The Ganga River Basin: A Hydrometeorological Approach. Springer, 37–52.

Received on: 14.04.2022; Revised on: 11.05.2022; Accepted on: 12.05.2022

J. Ind. Geophys. Union, 26(3) (2022), 195-206

Interpretation of the backscattering coefficient for distinct Indian lakes using Sentinel-1 SAR imagery

Anand S. Joshi [*1] and **Ashish B. Itolikar** [2]

[*1]Department of Basic Sciences and Humanities, MKSSS's Cummins College of Engineering for Women, Pune - 411052, India
[2]Applied Science Department, Jawaharlal Nehru Engineering College, MGM University, Aurangabad - 431003, India
[*]Corresponding author: anand.joshi@cumminscollege.in

ABSTRACT

Active Microwave Remote Sensing (MWRS) is used to monitor the ecological imbalances in the lake. The MWRS uses the C- band Synthetic Aperture Radar (SAR) sensor to transmit a vertically polarized signal and either receive it in vertically or horizontally polarized (VV or VH) form. The SAR sensor records the interaction of its transmitted signal with surface water in the form of the backscattering coefficient (σ0), which is the monitoring parameter. In the present work, 14 distinct surface water of lakes are monitored with the SAR data from Sentinel –1. All downloaded Sentinel–1 SAR datasets are for the post-monsoon month i.e., October 2021. Pre-processing and image processing of the Sentinel–1 SAR dataset were performed for the retrieval of the maximum, minimum, and mean σ0 values in VV and VH polarization for the distinct lakes. The comparative study of maximum and minimum σ0 for the VV and VH polarization shows that the VV polarization mode is more sensitive to surface water changes. The maximum and minimum mean σ0 values in the VV polarization mode among the distinct lakes are found to be -17.08 dB and -24.18 dB, respectively. The present work analyzes the σ0 values for these lakes and provides **a new** light on the causes in their fluctuations.

Keywords: Microwave Remote Sensing (MWRS), Backscattering coefficient, C–band, Lakes, SAR imagery, Sentinel–1.

INTRODUCTION

The existence of human civilization has always been greatly dependent on the surface water bodies that surround it. The lake, forming water bodies influence the climate in its area and plays an important role in maintaining and balancing its ecosystem. Measures to protect the lakes and our natural resources are of prime concern. To keep our lakes healthy and unpolluted by natural and human activities, it is important to monitor them (Balasubramanian, 2013).

Active microwave remote sensing (MWRS) is widely used to monitor the earth's surface as it provides data day and night and in all weather conditions. The Synthetic Aperture Radar (SAR) mounted on spacecraft or aircraft is a significant tool in active microwave remote sensing. The SAR sensor transmits a vertically polarized signal and either receives it in vertically or horizontally (VV or VH) polarized form. The SAR sensor records the interaction of its transmitted signal with earth terrain in terms of the backscattering coefficient. The parameter to be 'monitor' is the backscattering coefficient, also known as sigma0 (σ0).

The backscattering coefficient (σ0) is a dimensionless quantity representing the radar cross-section (m^2) of a given pixel on the ground per unit physical area of that pixel (m^2) and expressed in decibels dB (Ulaby et al., 1986). The backscattering coefficient σ0 depends upon the sensor property that is the frequency, the polarization state, the angles of incidence of the transmitted signal, and the surface properties, that is the complex dielectric constant of the target (water in the present case) and the surface roughness.

The detection and seasonal monitoring of the backscattering coefficient of various terrain entities such as soil, urban and rural area vegetation, lakes and wetlands, etc., for C-band microwave frequency has been carried out by various researchers (Guccione et. al., 2016; Huang et al., 2018; Carreño Conde and De Mata Muñoz, 2019; Chen et al., 2020; Desai et. al., 2020; Barasa and Wanyama, 2020; Abazaj and Hasko, 2020; Kumar, 2021). Instead of monitoring a lake over a seasonal period, a novel attempt is made in the present study to monitor the backscattering coefficient of the 14 distinct lakes for a specific period i.e., in the post-monsoon month of October 2021 using the C-band Sentinel-1 data.

From the classification methods of lakes, lakes are classified as freshwater, brackish, or saline lakes based on their water chemistry (salinity). The exchange between geological forces and climate leads to natural lakes. Most of the natural lakes are in the mountains of northern-eastern India. The glacial precipitation provides an adequate supply of water to overcome evaporative and seepage losses and keep the water in the lake year-round. Natural and freshwater lakes are with a low concentration of dissolved salt and other minerals. The concentration of dissolved salts and minerals is significantly high in the saline/Salt Lake. The concentration of dissolved salt in brackish lakes is in between freshwater and saline lakes. Artificial lakes are man-made lakes primarily built for industrial use and hydroelectric power generation (Bhateria and Jain, 2016).

The lakes in the present study are categorized as saline/brine lakes, brackish lakes, natural and fresh water lakes, and artificial lakes (Reddy and Char, 2004; Bhateria and Jain, 2016). The present study aims to (i) process Sentinel – 1 SAR dataset for retrieval of the backscattering coefficient sigma0 in VV and VH polarization for the distinct lakes during the post-monsoon month i.e., October 2021, (ii) make comparative study of the backscattering coefficient σ0 in VV and VH polarization mode, (iii) interpret the backscattering coefficient σ0 in VV polarization mode for distinct lake types, and (iv) analyse the possible causes of the fluctuation of the backscattering coefficient σ0 in the VV polarization mode.

METHODOLOGY

The Study Area

The 14 lakes selected for this study are Chilika Lake, Pangong Tso Lake, Pulicat lake, Sambhar Salt Lake, Nainital Lake, Loktak lake, Govind Ballabh Pant Sagar Lake, Bhopal Upper Lake, Wular Lake, Pichola Lake, Tso Moriri Lake, Lonar Lake, Manasarovar Lake, and Stanely Reservoir. The Chilika lake, stretches to three districts of Odisha, India i.e., Puri on the East, Khurda on the North, and Ganjam on the South. One-third of the Pangong Lake lies in Leh district of Lakadh and rest two-thirds, in China. At the border of the states of Andhra Pradesh and Tamil Nadu, lies Pulicat lake. The Sambhar Salt Lake and Pichola Lake are respectively situated in Jaipur district and Udaipur district of Rajasthan. Lake Nainital (also called Lake Naini) is located in the Nainital district of the Uttarakhand state. Loktak lake is located in Moirang Manipur. Govind Ballabh Pant Sagar is located in the Sonbhadra district of Uttar Pradesh, while Bhojtal, also known as Bhopal Upper Lake, is located in the capital city Bhopal in Madhya Pradesh. Wular lake is located in the Bandipora district of Jammu and Kashmir and lake Tso Moriri is located in the Changthang region of Ladakh. Lonar Lake is located in the Buldhana district of Maharashtra. Manasarovar Lake (also known as mTsho Mapham) is located near Mount Kailash in Burang country, Ngari Prefecture, Tibetan Autonomous Region. Similary, the Stanley reservoir is located in the Salem district of the state of Tamil Nadu. The type of lake, coordinates, lake surface area and surface elevation of these lakes are given in Table 1, the pictorial representation of these lakes is shown in Figure 1 (Google map).

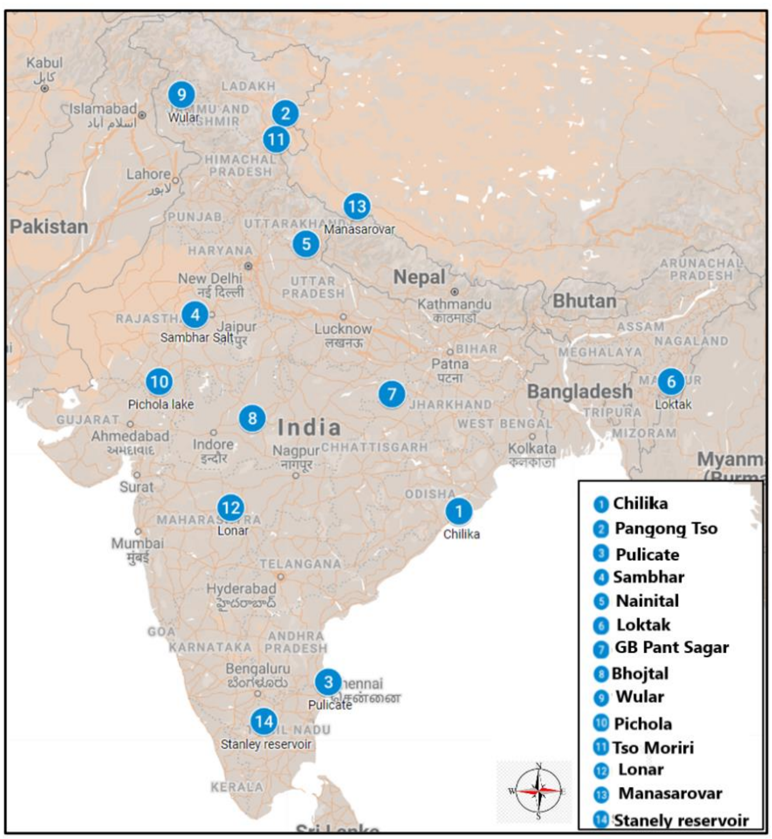

Figure 1. Pictorial representation of various studied lakes (Source: Google Map)

Data Acquisition

The European Commission's Earth observation programme, Copernicus, provides comprehensive information of the Earth's environment and security; using the Copernicus satellites and that from the ground, air, and sea-based measuring systems. Sentinel -1 is the first of the seven Copernicus satellite missions that the European Space Agency (ESA) is developing.

The Sentinel -1 is composed of a set of two identical C-band synthetic-aperture radar imagery satellites sharing the same orbital plane with 180˚ orbital phasing difference, providing Earth's surface images in all-weather conditions, day and night. Each Sentinel – 1 satellite is in a near-polar (98.18˚) Sun – Synchronous orbit at 693 km (431 mi) altitude with a 12- day repeat cycle and 175 orbits per cycle. The Sentinel – 1 operates in four exclusive acquisition modes, namely Stripmap (SM), Interferometric Wide Swath (IW), Extra-Wide Swath (EW), and Wave (WV).

In the present study, the acquisition of data product is done in Interferometric Wide Swath (IW) mode, as IW aims to study and monitor land cover. Interferometric Wide (IW) Swath maps global land cover once every 12 days and provides a swath of coverage of 250 km, with a spatial resolution of 5 x 5 meters.

The data product is available with single or double polarization i.e. (HH or VV) or (HH + HV or VV + VH). A total of 14 data products are downloaded from the Copernicus Open Access Hub [scihub.copernicus.eu]. The data product downloaded is the Interferometric Wide Swath (IW) mode Level – 1 Ground Range Detected (GRD) mode for October 2021, which is the post-monsoon period in India. Ground Range Detection (GRD) Level – 1 data with a multi-looked intensity only (systematically distributed) are given in Table 2.

Pre-processing

The Sentinel Application Platform (SNAP), is a common architecture for all Sentinel toolboxes. The architecture developed by Brockmann Consult, Skywatch, Sensar, and C-S is ideal for processing and analyzing earth observations. The Copernicus programme provides free and open access to data acquired by Sentinel satellites. Sentinel–1 GRD Synthetic Aperture Radar (SAR) datasets we use in the present study require a few correction steps. The pre-processing i.e., application of standard correction steps to Sentinel – 1 GRD data set to extract information from the processed data is created within the Sentinel Application Platform (SNAP). The processed sentine –1 GRD level–1 SAR data (image) corresponds to backscatter coefficient σ0, the information in which we are interested. The steps (i) – (vi) for pre-processing the data set and image processing (Veci, 2016; Filipponi, 2019; Kumar, 2021) to extract the backscatter coefficient σ0 using the Sentinel Application Platform (SNAP) is presented in Figure 2 and discussed below:

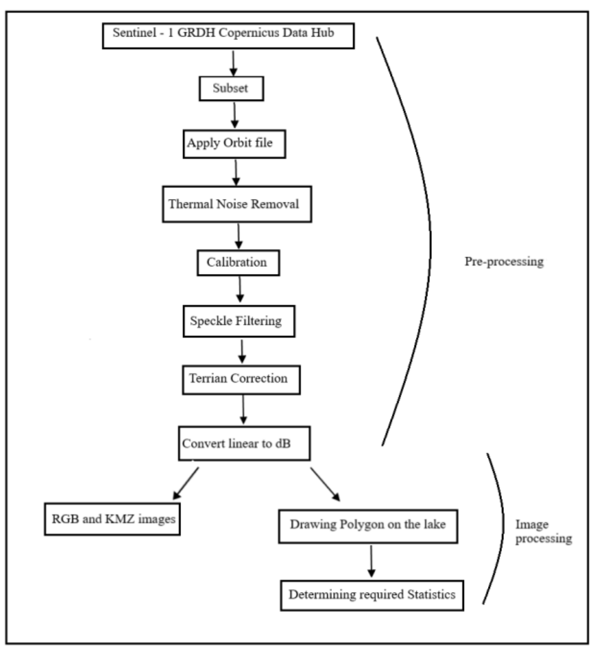

Figure 2. Sentinel- Ground Range Detected (GRD) pre-processing and image–processing steps

Table 1. Type of lakes, coordinates, lake surface area, and surface elevation of 14 lakes considered in present study

Lake	Type of lake	Latitude (˚N)	Longitude (˚E)	Area covered (km^2)	Elevation (m)
Tso Moriri	Brackish	32.9112	78.3159	120	4,522
Chilika	Brackish to Saline	19.8450	85.4788	1100	0 – 2
Lonar	Salt/Saline Lake	19.9758	76.5069	1.13	480
Pulicate	Saline	13.4177	80.3185	759	100 – 1200
Sambhar Salt	Salt to brine	26.9261	75.0962	190 – 230	360
Pangong Tso	Saline	33.7595	78.6674	604	4,225
Nainital	Natural freshwater	29.3869	79.4598	0.5	1,938
Loktak	Natural freshwater	24.5593	93.8147	287 – 500	768.5
Manasarovar	Natural freshwater	30.6615	81.4718	410	4,590
Wular	Freshwater	34.3696	74.5580	30 – 189	1,580
Pichola lake	Freshwater	24.5720	73.6790	6.96	590
Govind Ballabh Pant Sagar	Artificial	24.1426	82.8425	130	265
Bhojtal	Artificial	23.2532	77.3382	31	500
Stanley reservoir	Artificial	11.9034	77.8310	42.5	238

(i) Apply orbit file

The first step is to update and restore the orbit file. The orbit state vector information in the metadata information of SAR products is inaccurate. The precise orbit step provides accurate satellite position information and velocity information. SNAP is programmed to automatically download and update the orbit state vectors for each SAR section in its product metadata. The precise orbits state vectors are available for each satellite for the SNAP, from a few days to months after the product generation.

(ii) Thermal noise removal

The disturbance in the intensity of the Sentinel–1 image is caused by thermal noise in the cross-polarization channel. These thermal noise effects in the image must be removed from the inter-sub-swath texture. Performing this step with the SNAP toolbox reduces thermal noise effects in the Sentinel–1 image and, in particular, normalizes the backscatter signal throughout the Sentinel-1 scene. Thus, this operational step discards the additional noise from sub-swaths in multi-swath acquisition modes.

(iii) Calibration

In this procedural step, digital SAR data pixel values are transformed into equivalent radiometrically calibrated SAR backscatter intensity images. The calibration vector information within the Sentinel – 1 GRD products uses the calibration equation and converts the image intensity values to backscatter intensity i.e., σ0. To generate a radiometrically calibrated SAR backscatter to the nominally horizontal plane. The σ0 specifies the strength related to the geometric cross-section of a distributed target. The σ0 depends on the angle of incidence, wavelength, and polarization, including the scattered surface's surface properties.

(iv) Speckle filtering

Interference caused by waves scattered from the surface creates granular noise in the SAR images known as speckles. The speckle or spatial filtering step reduces the speckles in the image and thereby improves the quality of the image.

(v) Range Doppler terrain correction

SAR images are distorted due to side-looking geometry and shadows caused by the Earth's surface, and this step perform a correction for each SAR pixel. The stage overcomes the distortions caused by the earth's surface. SNAP software downloads SRTM 1 sec HGT DEM files to convert the data from ground range geometry to σ0. The processed image is the best possible real image.

(vi) Conversion to dB

The final step converts the unitless backscattering coefficient from linear to dB (decibel) using logarithmic transformation. The image processing step requires drawing the polygon(s) on the lake surface, the statistical information is then extracted.

Table 2. Data acquisition from Sentinel–1: filename and date

Sentinel – 1 image ID (S1A_IW_GRDH_1SDV_ pre-fixed)	Observation Date (DD-MM-YYYY)
20211001T001344_20211001T001409_039918_04B945_53CE	01-10-2021
20211021T004257_20211021T004326_040210_04C35B_2DBA	21-10-2021
20211023T003148_20211023T003213_040239_04C461_42A6	23-10-2021
20211023T130307_20211023T130332_040247_04C4AB_956B	23-10-2021
20211025T124732_20211025T124757_040276_04C5B5_54FC	25-10-2021
20211016T233933_20211016T233958_040151_04C153_C8C7	16-10-2021
20211006T002046_20211006T002111_039991_04BBCD_9E3D	06-10-2021
20211009T004531_20211009T004556_040035_04BD42_BD24	09-10-2021
20211018T125657_20211018T125722_040174_04C225_E0BB	18-10-2021
20211019T010144_20211019T010209_040181_04C262_2C1C	19-10-2021
20211025T124822_20211025T124847_040276_04C5B5_BA9E	25-10-2021
20211009T004646_20211009T004711_040035_04BD42_FE0B	09-10-2021
20211028T003519_20211028T003544_040312_04C6EF_F889	28-10-2021
20211028T004044_20211028T004109_040312_04C6EF_AADD	28-10-2021

RESULTS AND DISCUSSION

Using pre-processing steps (i) to (vi) in the 14 datasets from 14 lakes and image processing to extract the backscattering coefficient σ0 with the Sentinel Application Platform (SNAP), discussed under Methodology, the detailed results obtained for the Lonar Lake is shown in Figure 3. The dB image in VH and VV polarization mode and the image processing of the other 13 lakes are shown in Figure 4 to 16.

In the image processing steps, the statistical information is extracted from the polygons drawn on the lake surface. The pixel value results in the backscattering coefficient σ0. The maximum pixel value, the minimum pixel value, and the arithmetic mean of all pixel values of the backscatter coefficient σ0 were determined from the total number of pixels in selected polygons.

The lake σ^0 values were extracted from the created polygon, which is arranged to cover the lakebed and not the adjacent land and lake. This not only minimizes the speckle effect required for the statistical calculation but also reduces the uncertainties when covering flat surfaces (Liu, 2016). Compared to the maximum and the minimum VH polarized σ0 values (Table 3 Column 4 VH and Column 5 VH) to the maximum and the minimum VV polarized σ0 values (Table 3 Column 4 VV and Column 5 VV), VV polarized σ0 has low values and widespread variations, which is due to the surface scattering effects giving a higher signal on the VV channel. This is also shown in Figure 17. Therefore, in the present study, VV polarized σ0 values were chosen to understand their possible variations.

The fluctuations in the backscattering coefficient depend on the polarization, angles of incidence, surface roughness, and dielectric property of the surface (water). The dielectric property, in turn, is a function of salinity. The data for all the lakes are recorded for the C-band frequency and at an incidence angle of 38.5˚ (Laur et. al., 2020). The surface of lakes is considered to be a smooth surface. Since the polarization VV, angle of incidence, and frequency parameters are well defined, the variation in the σ0 in the distinct lakes will be mainly due to changes in the salinity of the water.

Table 3 shows σ0 for the lake type brackish to brine i.e., Tso Moriri, Chilika, Lonar, Pulicate, and Sambhar Lakes and Pangong Lake. No significant variations are observed in the maximum and minimum σ0 values for VV polarization in the Lonar and Sambhar lakes. The maximum and minimum values for VV polarization of these lakes are -19.50 dB to -23.41 dB and -21.08 dB to -26.78 dB respectively. However, the maximum and minimum σ0 for VV polarization for the Tso Moriri lake, -10.52 dB to -24.83 dB, Chilika lake, -3.07 to -25.91 dB, Pulicate lake -8.11 dB to -25.82 dB and Pangong lake, -12.74 dB to -27.74 dB significant variations are observed. The effective range of backscattering coefficient for maximum and minimum

values for the VV polarization change for a brackish to saline type lake can also be seen in column 6 of Table 3. The effective range difference of Lonar and Sambhar Lake is low, 3.91 and 5.7 as compared with Tso Moriri, Chilika lake, Pulicate lake, and Pangong lake i.e., 14.31, 22.84, 17.71, and 15, respectively. The probable reason for variations in the maximum and minimum σ0 values for the Chilika Lake and Pulicate Lake is an increase in salts and minerals in these lakes due to the flooding during the rainy season from the Daya and Bhargavi rivers. These lakes are located in the eastern part of India near the Bay of Bengal Sea, there may be an influx of seawater i.e. saline water into these lakes. The Tso Moriri and Pangong lakes are situated in the Himalayan region where salts and minerals from the mountains are dissolved with the lake water (Barik, 2017; Barik et al., 2020). The maximum and minimum σ0 values for VV polarization for freshwater lake Wular Lake, -15.28 dB to -23.52 dB, and Pichola Lake, -15.51 to -22.61 dB. The effective range difference for freshwater lakes, Wular, and Pichola lakes is almost similar. For the natural freshwater lakes, Loktak and Manasarovar, the maximum and minimum σ0 values for VV polarization are -8.99 dB to -23.09 dB and -8.45 dB to -27.67 dB respectively. The effective range difference is 14.1 and 19.22 respectively.
For the artificial water lakes, Govind Ballabh Pant Sagar, Bhojtal Lake, and Stanley Reservoir, maximum and minimum σ0 values for VV polarization are -13.06 dB to -27.88 dB, -12.10 dB to -24.36 dB, and -16.83 to -24.60 respectively. The effective range difference is 14.82, 12.26, and 7.77 respectively.

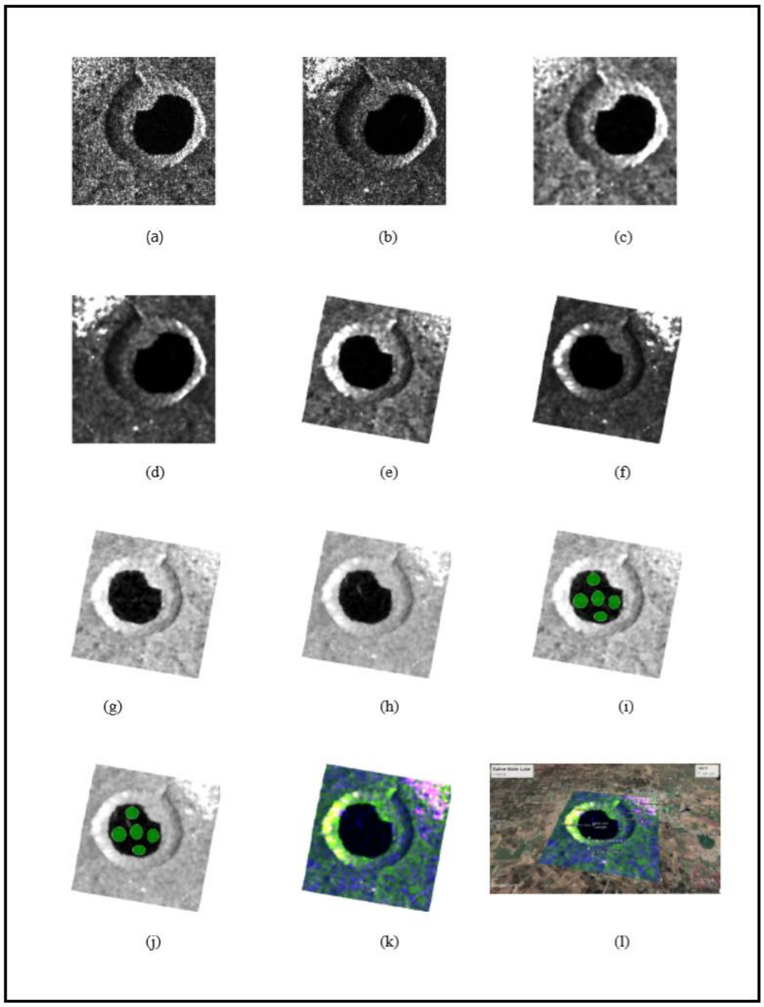

Figure 3. Pre-processing and image processing of Lonar Lake, image after application of the orbit file in (a) VH polarization mode, (b) VV polarization mode; speckled filtered and calibrated image, (c) VH polarization mode, (d) VV polarization mode; Terrian corrected image, (e) VH polarization mode, (f) VV polarization mode; Conversion of linear to dB, (g) VH polarization mode, (h) VV polarization mode; Selection of the region to determine the required statistics, (i) VH polarization mode, (j) VV polarization mode, (k) RGB image, and (l) KMZ Google Earth image.

Table 3. The mean, maximum, and minimum backscattering coefficient values of lakes

	Lake type (2)	Mean σ0 (3)		Maximum σ0 (4)		Minimum σ0 (5)		Difference - effective range (6)	
		VH	VV	VH	VV	VH	VV	VH	VV
Tso Moriri	Brackish	-25.55	-19.42	-20.21	-10.52	-28.81	-24.83	8.6	14.31
Chilika	Brackish to Saline	-24.18	-20.18	-8.53	-3.07	-27.81	-25.91	19.28	22.84
Lonar	Saline Lake	-23.82	-21.44	-22.00	-19.50	-25.96	-23.41	3.96	3.91
Pulicate	Saline	-24.08	-21.46	-17.54	-8.11	-27.25	-25.82	9.71	17.71
Sambhar	Salt to brine	-24.98	-24.18	-19.18	-21.08	-27.20	-26.78	8.02	5.7
Pangong Tso	Saline lake	-25.65	-21.52	-18.64	-12.74	-28.92	-27.74	10.28	15
Nainital	Natural freshwater	-23.15	-19.72	-21.78	-16.77	-24.33	-21.49	2.55	4.72
Loktak	Natural freshwater	-23.27	-19.40	-15.47	-8.99	-26.97	-23.09	11.5	14.1
Manasarovar	Natural freshwater	-23.03	-17.08	-15.42	-8.45	-28.42	-27.67	3.8	19.22
Wular	Freshwater	-22.66	-21.29	-20.4	-15.28	-24.56	-23.52	4.16	8.24
Pichola lake	Freshwater	-24.08	-19.18	-22.05	-15.51	-26.12	-22.61	4.07	7.1
Govind Ballabh Pant Sagar	Artificial	-27.12	-23.14	-19.46	-13.06	-30.79	-27.88	11.33	14.82
Bhojtal Lake	Artificial	-24.67	-21.53	-18.57	-12.10	-27.11	-24.36	8.54	12.26
Stanley reservoir	Artificial	-23.34	-21.71	-20.64	-16.83	-26.19	-24.60	5.55	7.77

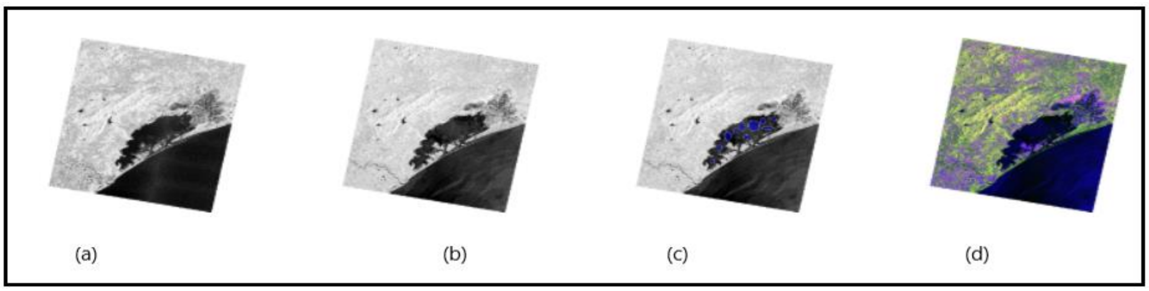

Figure 4. Chilika Lake – The conversion of a linear to a dB image, (a) VH polarization mode, (b) VV polarization mode, (c) selecting the area to determine the required statistics, and (d) RGB image

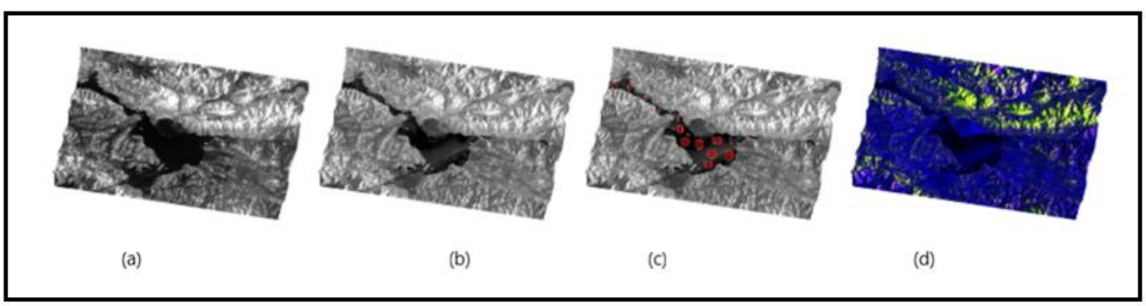

Figure 5. Pangong Tso Lake – The conversion of a linear to a dB image, (a) VH polarization mode, (b) VV polarization mode, (c) selecting the area to determine the required statistics, and (d) RGB image

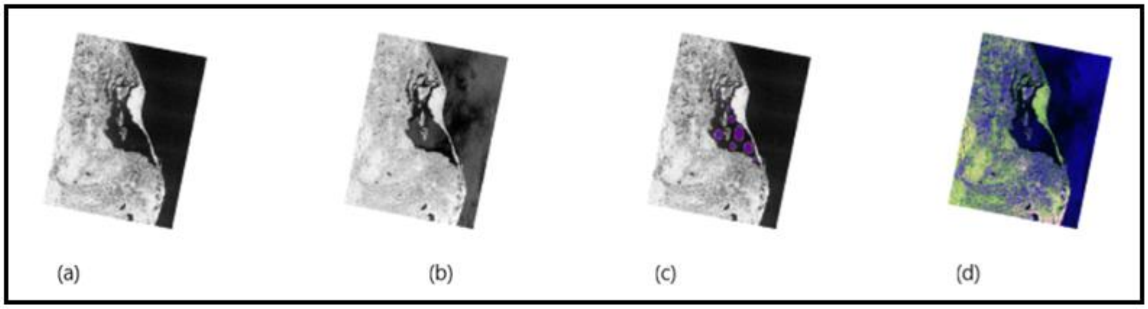

Figure 6. Pulicate Lake – The conversion of a linear to a dB image, (a) VH polarization mode, (b) VV polarization mode, (c) selecting the area to determine the required statistics and (d) RGB image

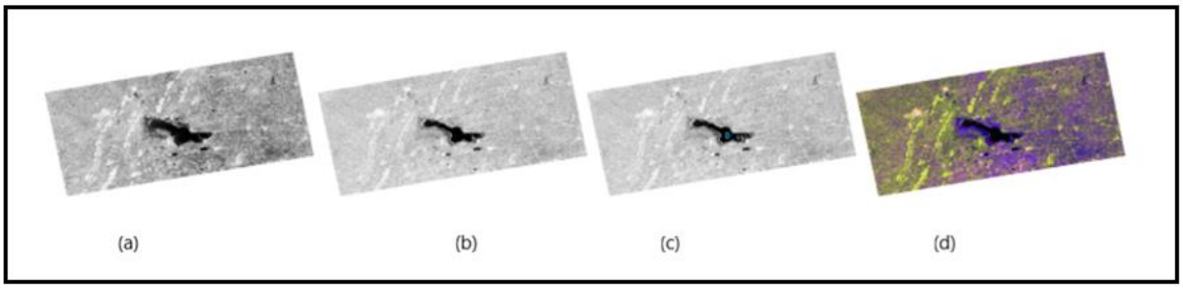

Figure 7. Sambhar Lake – The conversion of a linear to a dB image, (a) VH polarization mode, (b) VV polarization mode, (c) selecting the area to determine the required statistics, and (d) RGB image

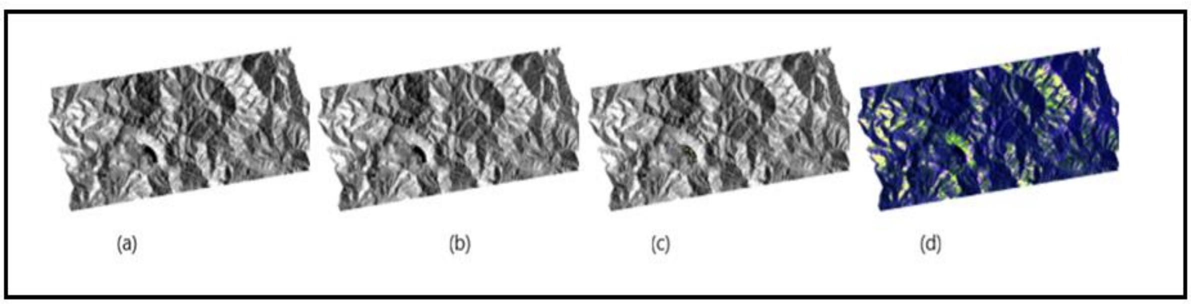

Figure 8. Nainital Lake – The conversion of a linear to a dB image, (a) VH polarization mode, (b) VV polarization mode, (c) selecting the area to determine the required statistics, and (d) RGB image

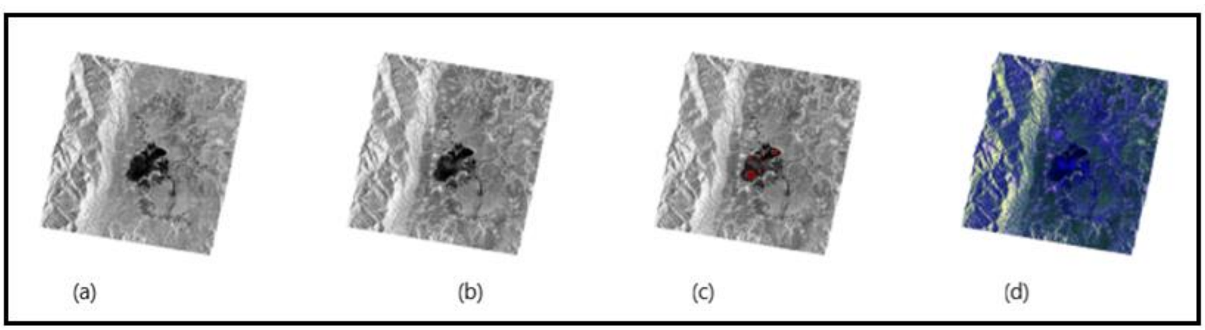

Figure 9. Loktak Lake – The conversion of a linear to a dB image, (a) VH polarization mode, (b) VV polarization mode, (c) selecting the area to determine the required statistics, and (d) RGB image

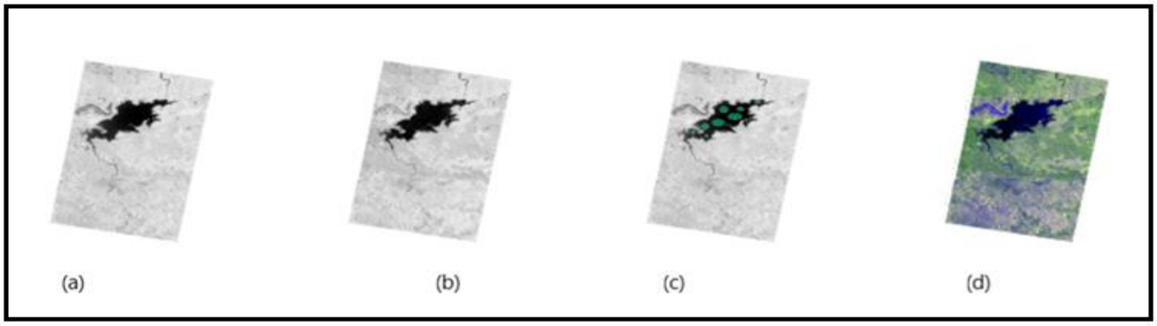

Figure 10. Govind Ballabh Pant Sagar – The conversion of a linear to a dB image, (a) VH polarization mode, (b) VV polarization mode, (c) selecting the area to determine the required statistics, and (d) RGB image

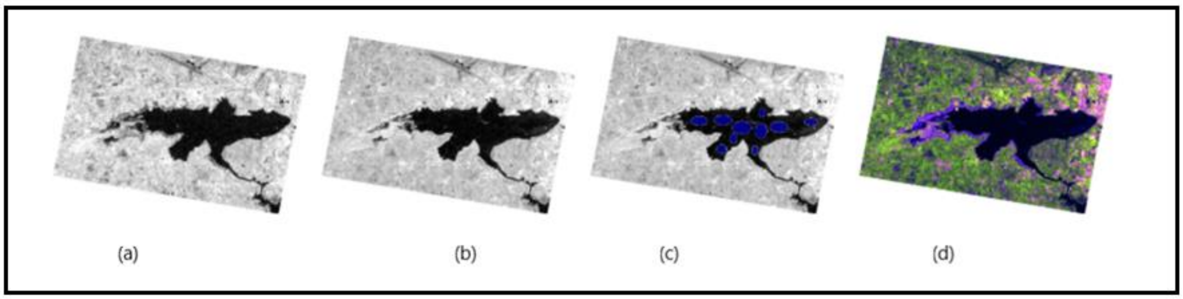

Figure 11. Bhojtal Lake – The conversion of a linear to a dB image, (a) VH polarization mode, (b) VV polarization mode, (c) selecting the area to determine the required statistics, and (d) RGB image

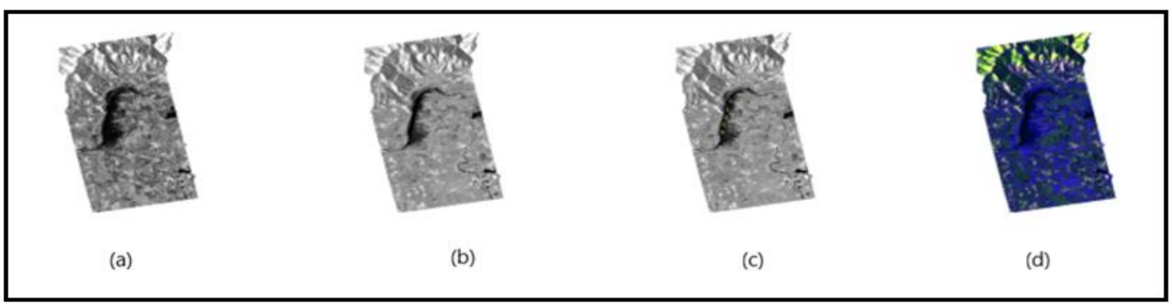

Figure 12. Wular Lake – The conversion of a linear to a dB image, (a) VH polarization mode, (b) VV polarization mode, (c) selecting the area to determine the required statistics, and (d) RGB image

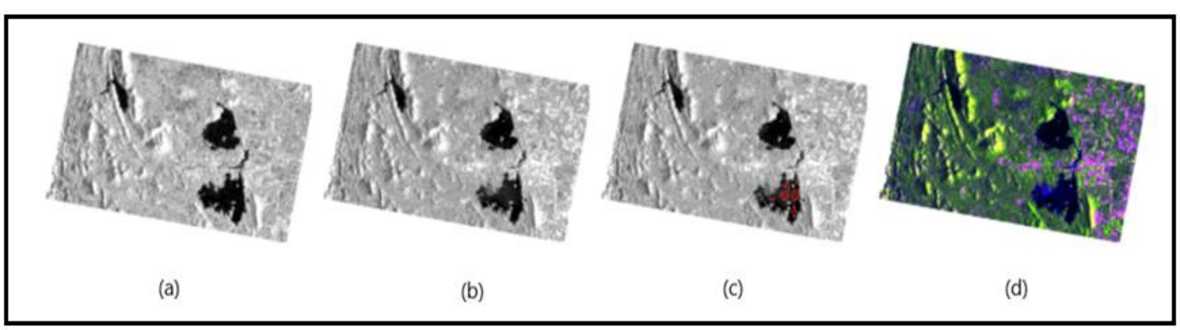

Figure 13. Pichola Lake – The conversion of a linear to a dB image, (a) VH polarization mode, (b) VV polarization mode, (c) selecting the area to determine the required statistics, and (d) RGB image

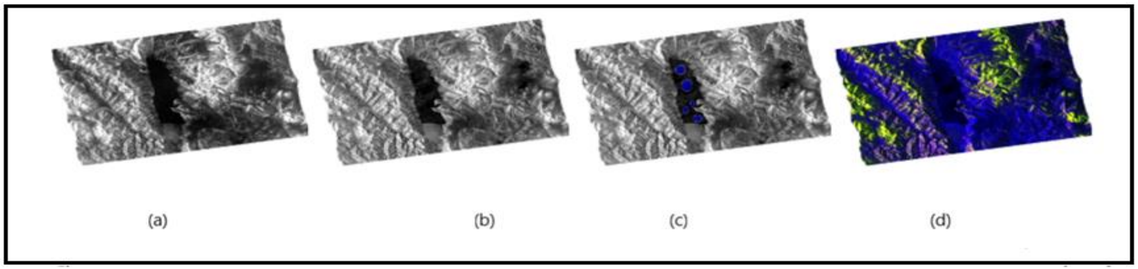

Figure 14. Tso Moriri Lake – The conversion of a linear to a dB image, (a) VH polarization mode, (b) VV polarization mode, (c) selecting the area to determine the required statistics, and (d) RGB image

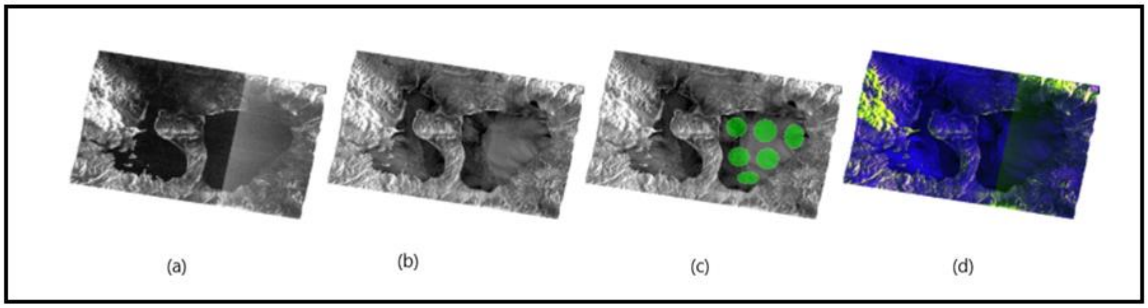

Figure 15. Manasarovar Lake– The conversion of a linear to a dB image, (a) VH polarization mode, (b) VV polarization mode, (c) selecting the area to determine the required statistics, and (d) RGB image

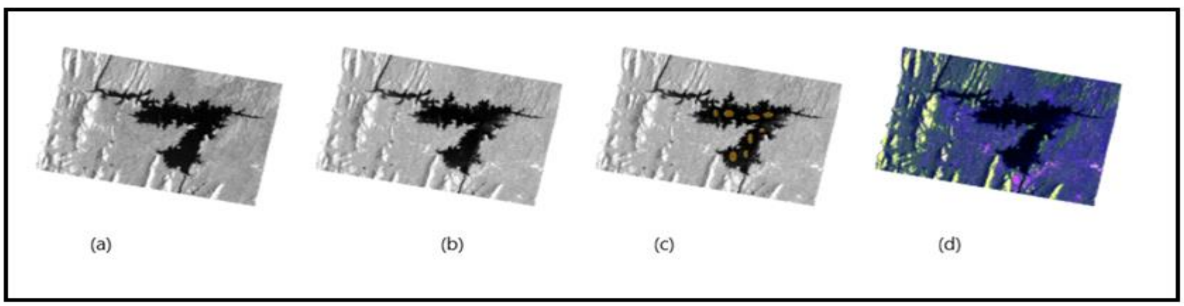

Figure 16. Stanley reservoir – The conversion of a linear to a dB image, (a) VH polarization mode, (b) VV polarization mode, (c) selecting the area to determine the required statistics, and (d) RGB image

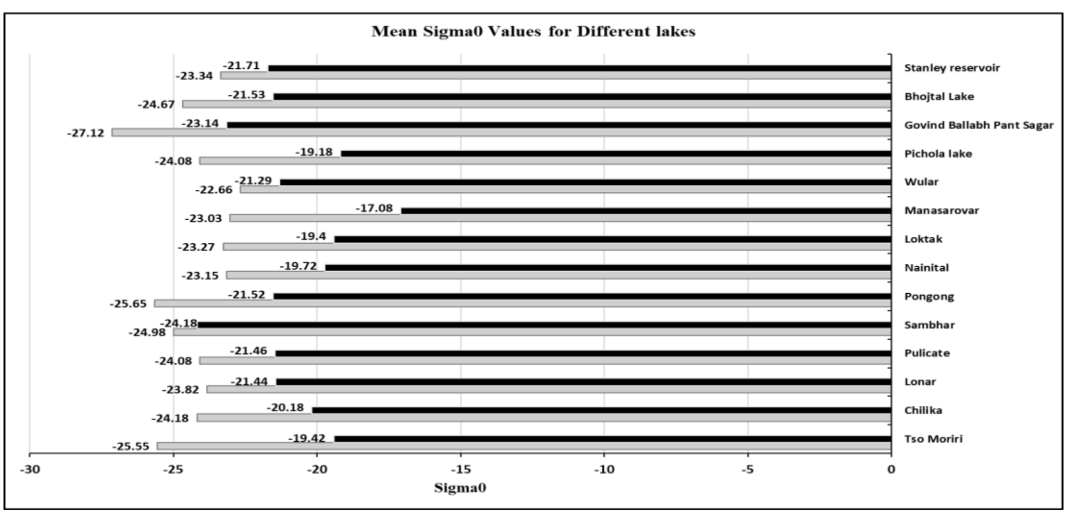

Figure 17. Graphical representation of σ0 for VH and VV polarization; Gray – VH, and Black – VV

The VH polarized and VV polarized mean backscattering coefficients σ0 of distinct lakes are plotted in Figure 17 and shown in column 3 VV in Table 3. It is observed that VV polarized mean σ0 values decrease markedly for natural and freshwater lakes to saline/brine water lakes. The freshwater lake Manasarovar Lake σ0 is -17.08 dB and Lake Sambhar with the most saline water has a σ0 value of -24.18 dB. With a comparison of σ0 among the natural freshwater and freshwater lakes, the backscattering coefficient of Wular Lake is low. Though Wular Lake is a freshwater lake, its backscattering coefficient is low, this might be due to the surface aquatic plants in selected polygons (Keller et al., 2018). The backscattering coefficient is influenced by surface aquatic plants. The artificial lakes have values similar to a saline lake, the artificial lake originally created by man for agricultural, industrial, and hydroelectric projects, collects rainwater and water from nearby streams. Due to industrial discharges, household discharges, and human pollution, dissolved salts are found to be more in artificial lakes and reservoirs. The increase in salinity of Lake Govind Ballabh Pant Sagar lake has been noted due to the discharge of coal mine water and due to the mixing of flying ash from the nearby coal mining (Khan, 2020; Rani et. al., 2014).

CONCLUSIONS

In this paper, the C–Band SAR Sentinel–1 dataset were pre-processed and image processed to extract the VV and VH polarization mode σ0 values from 14 distinct lakes. The retrieved results show that the VV polarization mode has a wider effective range difference compared to the VH polarization and is sensitive to the change in lake type. The maximum and minimum mean σ0 values among the distinct lakes are -17.08 dB and -24.18 dB. The study interprets and analyze the possible causes for the variations of the maximum, minimum, and mean σ0 values for the same and different lake type i.e., saline lakes, natural and freshwater lakes, and artificial reservoirs. The mean σ0 value decreases with increasing salt content in water. Monitoring of saline lakes, natural and freshwater lakes, and artificial reservoirs is significant as these lakes play crucial roles in the existence of the ecology community and climate change. The survival of fish and aquatic plants is reduced in saline lakes. A decrease of the mean value σ0 in the freshwater lake signifies that the lake is turning into a saline type. In addition, the mean σ0 would be monitored for the artificial lakes and reservoirs, so that pollution from industries, households, and humans could be minimized. We will extend the present study by pre-and image-processing and extracting the σ0 for different lake types during the pre-monsoon, monsoon, and post-monsoon periods. The resulting database will be a comprehensive study of the σ0 in the distinct lake types and for the distinct period.

ACKNOWLEDGMENT

The authors thank ESA for making freely available the Sentinel – 1 data and the SNAP software. The authors are grateful to Dr. M. L. Kurtadikar and their working academic institutes for giving constant encouragement to work towards scientific contributions.

Compliance with Ethical Standards

The authors declare that they have no conflict of interest and adhere to copyright norms.

REFERENCES

Abazaj, F. and Hasko, G., 2020. Use of Sentinel-1 Data in Flood Mapping in the Buna River Area. Int. J. Environ. climate change., 10(10), 147-156.

Balasubramanian, A., 2013. Origin and Characteristics of Lakes. Technical Report 2., University of Mysore. doi:10.13140/RG.2.2.34305.04962.

Barasa, B. and Wanyama, J., 2020. Freshwater Lake inundation monitoring using Sentinel-1 SAR imagery in Eastern Uganda, Annals of GIS., 26(2), 191-200.

Barik, S.K., 2017. Water quality monitoring of Chilika lake. Technical report CDA-ICZM project of Odhisha.

Barik, S.K., Kar, B.B., Dixit, P.R. and Bastia, T.K., 2020. Water Quality Index A Critical Tool for an Assessment of Biodiversity of Inland Water Ecosystem. J. Water Engineering and Management., 1(1), 44-54.

Bhateria R. and Jain, D., 2016. Water quality assessment of lake water: a review. Sustainable Water Resources Management., 2(2), 161-173.

Carreño Conde F. and De Mata Muñoz, M., 2019. Flood monitoring based on the study of Sentinel – 1 SAR images: The Ebro River case study, Water., 11(12), 2454.

Chen, Y., Qiao, S., Zhang, G., Xu, Y.J., Chen, L. and Wu, L., 2020. Investigating the potential use of Sentinel-1 data for monitoring wetland water level changes in China's Momoge National Nature Reserve. Peer J., https://doi.org/10.7717/peerj.8616

Desai, D., Mandowara, A. and Nigam, R., 2020. Modeling of rice crop biomass using Sentinel-1 backscatter coefficients: A case study over Nawagam, Gujarat, J. Agrometeorology., 22(1), 67-70.

Filipponi, F., 2019. Sentinel-1 GRD preprocessing workflow. In Multidisciplinary digital publishing institute proceedings., 18(1), 11.

Guccione, P., Lombardi, A. and Giordano, R., 2016. Assessment of seasonal variations of radar backscattering coefficient using Sentinel-1 data, in IEEE Int. Geosci. Remote Sensing Symp., (IGARSS), 3402-3405. doi: 10.1109/IGRASS.2016.7729879.

Huang, W., DeVries, B., Huang, C., Lang, M.W., Jones, J.W., Creed, I.F. and Carroll, M.L., 2018. Automated extraction of surface water extent from Sentinel-1 data, Remote Sensing., 10(5), 797.

Keller, R.P., Masoodi A. and Shackleton, R.T., 2018. The impact of invasive aquatic plants on ecosystem services and human well-being in Wular Lake, India. Reg. Environ. Change., 18(3), 847-857.

Khan, M.F., 2020. Physico-Chemical and Statistical Analysis of Upper Lake Water in Bhopal Region of Madhya Pradesh, India. Int. J. of Lakes and Rivers. 13(1), 1-16.

Kumar, D., 2021. Urban objects detection from C-band synthetic aperture radar (SAR) satellite images through simulating filter properties. Scientific Reports., 11(1), 1-24. doi: org/10.1038/s41598-021-851219.

Laur, H., Bally, P., Meadows, P., Sanchez, J., Schaettler, B., Lopinto, E. and Esteban, D., 2020. Derivation of the backscattering coefficient σ0 in ESA ERS SAR PRI products. In Proc. of the Second International Workshop on ERS Applications., 139.

Liu, C.H., 2016. Analysis of Sentinel-1 SAR data for mapping standing water in the Twente Region. Master Dissertation. The University of Twente.

Rani, M., Yadav, S.K. and Kumar, A., 2014. Geochemical alterations in surface waters of Govind Ballabh Pant Sagar, Northern Coalfield, India. Environ. Earth Sci., 71(7), 3181-3193.

Reddy, M.S. and Char, N.V.V., 2004. Management of lakes in India Annex 2 list of the lake. World Lakes Network. 19-20.

Ulaby, F.T., Moore, R.K. and Fung, A.K., 1986. Microwave Remote Sensing, Active and Passive: Vol III, Published by Artech House Boston, MA, USA.

Veci, L., 2016. Sentinel-1 Toolbox TOPS Interferometry Tutorial. European Space Agency, Paris, France, 1-20.

Received on: 04-04-2022; 01-05-2022; Accepted on: 10-05-2022

J. Ind. Geophys. Union, 26(3) (2022), 207-216

Variability of atmospheric electric parameters during pre-lockdown and lockdown periods of 2020 – 2021 at Tirunelveli (Tamilnadu, India)

C.P. Anil Kumar[1*], N. Venkatesh[1], Arul Asir[2], and C. Selvaraj[1]

[1]Equatorial Geophysical Research Laboratory, Indian Institute of Geomagnetism, Krishnapuram, Tirunelveli– 627011, Tamil Nadu, India
[2]Popes College, M.S. University, Tirunelveli- 628251, Tamil Nadu, India
*Corresponding author: anilkumar.cp.iig@nic.in

ABSTRACT

We got unique opportunity to carry out the globally improved air pollution-based atmospheric electricity experiments from 2020 to 2021. This period composes of lockdown phases of the Covid-19 pandemic. Tirunelveli (8.7^{0}N,77.8^{0}E) in Tamil Nadu, is one of the southern Indian peninsular stations for the observations of atmospheric electric parameters (AEP). A comparative study of AEP has been made during the pre-pandemic period and the lockdown period imposed to control the spread of Novel Corona virus infection with the help of ground-based indigenously developed atmospheric electric instruments. The analysis of both 2020 and 2021 data showed a marked difference in electric field and air-Earth (AE) current density. The difference in the AEP pattern is attributed to some extent to the decrease in aerosol loading caused by minimum human activities, drastically reduced emissions from industry, building construction, quarrying and mining, cement plants, vehicular emission, and stoppage of particulate matters, etc, which seem to have reduced the resistivity load in a global electric circuit (GEC).

Keywords: Global electric circuit, Meteorology, Atmospheric electric parameters (DC), Statistic analysis, Pollution, Resistivity load, Covid-19 pandemic, Tirunelveli

INTRODUCTION

Particulate matters are a complex mixture of organic and inorganic substances that are found in the ambient air and play a vital role in the radiation budget of the atmosphere via the scattering and absorption processes (Qu et al., 2017). Other main sources are vehicular emissions, industry, building construction, quarrying and mining, cement plants, and the burning of fossil fuels from power plants. All these constituents are the cause of air pollution and a major environmental concern, which affects the atmospheric electric measurements. During the period 2020-2021, the Government of India and the State Government of Tamil Nadu, imposed a lockdown from April 2020 to June 2020 and again during the second wave from April 2021 to May 2021 to stop the spreading of the Novel Coronavirus (Covid-19) infection. During the lockdown period, these emissions were cut-off due to severely restricted human, industrial, and transportation activity. As such, a change in air pollution levels was expected. Numerous studies were performed globally to evaluate air pollution during Covid lockdown phases (Resmi et al., 2020; Gautam, 2020; Sharma et al., 2020; Kannaiah et al., 2020; Bao and Zhang, 2020; Shi and Brasser, 2020; Kinoshita et al., 2020; Tobias et al., 2020; Nakada and Urban, 2020; Asir, 2021). Few studied the role of atmospheric variation in surface NO, NO_2, CO, SO_2, NH_3, volatile organic compounds (VOCs), and particulate matter (PM) variations (Qu et al., 2017).

Globally too, several investigations have been made on the pollution rate/air quality index during lockdown phases (Bao and Zhang, 2020; Shi and Brasser, 2020; Kanniah et al., 2020; Tobioas et al., 2020; Nakada and Urban, 2020). Bao and Zhang (2020) reported a significant decrease in SO_2, NO_2, CO, and particulate matter ($PM_{2.5}$ and PM_{10}) in China. Kannaiah et al. (2020) revealed that the restricted industrial activity imposed during the lockdown period resulted in a reduced concentration of aerosol optical depth and tropospheric NO_2 over the East Asian region. Shi and Brasser (2020), Tobias et al., (2020) and Nakada and Urban (2020) studied such changes in air quality in China, Barcelona (Spain), and São Paulo in Brazil, respectively. A similar type of observation in air quality index and pollution levels has been reported in India (Resmi et al., 2020, Gautam, 2020, Sharma et al., 2020). Resmi et al. (2020) and Asir (2021) carried out similar investigations at the regional level in India. During the pre-lockdown period and different stages of lockdown, Resmi et al. (2020) reported the diurnal variability of pollutants in Kerala; while, Asir (2021) studied the pollution levels during the lockdown period in the southern region of Tamil Nadu. Both these studies indicate that the concentration of pollutants declined by 50% or above from pre-lockdown days to lockdown days. Regional air-quality reports from Tirunelveli Pollution Control Board also suggested that during lockdown days, vehicular emissions, NO_2, CO, etc. are considerably reduced by more than 55% per day. Overall, these studies indicate that the air pollution levels decreased by about 40-55 % or even more during the lockdown period.

These lockdown days provided an excellent opportunity for atmospheric scientists to study the changes in atmospheric electric parameters and happenings in the tropospheric boundary layer when the air pollution was considerably reduced. As such, this dramatic decline in air pollution during the lockdown period is expected to have significant consequences on the columnar resistance in the global electric circuit (GEC). Such improvement in the columnar resistance during the lockdown in turn is expected to enhance conductivity in different parts of the globe. We carried out dedicated investigations on atmospheric electric parameters on regular basis at Tirunelveli (8.7^0 N, 77.8^0 E) in India from, January 2020 to June 2020 and January 2021 to June 2021. Contemporary automatic weather station (AWS) data analyses were carried out in EGRL on fair-weather days and reported here. We noted a marked difference in amplitude and phase of the aforesaid parameters during the lockdown phases brought about by the decrease in the quantity of overall atmospheric pollution level other than world lightning activity. We also found that the direct separation of hourly data concerning one-to-one UT time in these two intervals quantitatively described AEP, which implicitly shows its dependency on change in load resistance which is connected with air pollution of the global atmosphere.

OROGRAPHY AND EXPERIMENTS

The present measurement site in Krishnapuram village is 36 m above mean sea level (AMSL). This remote village has less human habitat, emissions from industry are very less, very few building constructions, no quarrying, no mining, no cement factory, and vehicular emission is comparatively less. These factors of less local aerosol loading provided a clear window for carrying out the atmospheric measurements since 1997. The terrain is mostly rocky, less sandy and rainfall is scanty as it falls in the rain shadow area of the Western Ghats. Corona current due to the pointed objects is totally avoided by removing the wild grass. The Gulf of Mannar is at a distance of 35 km. The nearest twin cities Tirunelveli and Palayamkottai are 14 km and 12 km away, respectively, from the experimental site so there is little anthropogenic pollution from the urban area. Earlier studies proved that this experimental site is suitable for atmospheric electric studies (Panneerselvam et al., 2003, 2007; Anil Kumar et al., 2009, 2013, 2020). Generally, the experiments are conducted from December to June at this station. During the rest of the year, bad weather prevails since this station comes under the monsoon tropics of the southern peninsular part of India. We present in this study high time resolution (1-second sample) data of electric field and near air-earth current density.

We describe the measurements of the AE current, electric field, small ion conductivity (not included in this study due to technical reasons), and meteorological parameters. The total air-Earth components include the conduction current, displacement current, and convection current. The conduction current, which is mainly a direct current, constitutes the current due to the actual transport of electric charge under the influence of an electric potential. The displacement current is the fluctuating part of the current and it contains spectra of frequencies. It does not involve any charge transport in the medium but exists because of the time variation of the electric field within it. When the charge carriers are driven by air motion, the current is called the convection current. It can occur in different directions and intensities depending on the space charge density, air movement, stability of the atmosphere, and gravity acting on a suspended charged particle. The AE current has been successfully measured with a horizontal long wire antenna. Despite the fact that airborne measurements provide conditions that minimize the effect of local disturbances, ground-based measurements are widely used because of their cost-effectiveness and capability for continuous long-term recordings. One of the most important ground-based sensors is the horizontal long-wire antenna (Kasemir, 1951; Kasemir and Ruhnke, 1959). We use a long wire antenna of 144 m in length and 3 mm in diameter. The sensor is supported 1 m above the ground by means of masts that are electrically separated by Teflon rods as shown in Figure 1. All the sensors and insulation are cleaned properly with isopropyl alcohol, periodically. The engineering details of the horizontal long wire antenna are provided in Anil Kumar et al. (2020).

Measurement of atmospheric electrical parameters in fair-weather is essential to understanding the fundamental processes that govern the electrical state of the atmosphere. Fair-weather conditions are the least electrically active, where no charge separation is expected to occur, with low wind speeds and less than three octas of cloud cover. The electric field is one of the important atmospheric electrical parameters and has been measured using a passive technique. In recent years, compact electric field mills (EFM) have been widely used for high-resolution measurements. This is an important instrument as it evaluates the height-integrated electric field over a 25 km wide area in the region under consideration.

Electric fields develop whenever there is a difference in electric potential. EFM is a specialized electro-mechanical instrument used for measuring the strength of the electric field in the atmosphere. An upward-facing EFM made up of non-magnetic stainless steel was deployed to measure the vertical electric fields over Tirunelveli and is shown in Figure 2. EFM device is based on the principle of electrostatic induction and primarily consists of two electrodes. One of them is exposed to the atmospheric electric field and has rotating vanes due to which the shielding and unshielding of the field take place. When the sensor is alternately exposed and shielded from the electric lines of force, the surface charge induced on the sensor is a time-varying function of the electric field. Thus, the induced electric current that flows to secondary sensor electrodes is proportional to the strength of the electric field. A higher electric field develops whenever there is a major difference in overhead electric potential.

Next, a charge amplifier measures the charge collected in the second electrode and the output is transferred to the measuring device through a multiplexer. Further details of EFM can be found at http://www.boltek.com.

Here the signal is not a function of the rotor frequency. Using the relation E = V/d, the electric field mill is calibrated with the known potential (V) of the horizontal plate at height (d) viz. 1 meter herein. Proper earthing, military quality components, and proper connectivity ensured that there is no error.

The globally decreased air pollution during Covid-19 lockdown times provided a unique opportunity for atmospheric physicists to understand the role of aerosol in defining the columnar resistances in GEC. The incoming solar radiation causes various chemical and physical mechanisms to control the weather phenomenon in the troposphere (Arnold et al., 1984; Castleman, et al., 1971; Eisele, 1988; Hoppel et al., 1986; Jonassen and Wilkening, 1965; Junge, 1963; Mani and Huddar, 1972; Alderman and William, 1996). It is very important to analyze the AWS data during AEP measurements. The AWS provides temperature, humidity, pressure, wind direction, and wind speed data. Fair- weather conditions viz. the cloud coverage, rain, and visibility have been monitored manually for this study. Observed meteorological parameters conformed to the fair-weather characteristics and are summarized in Table 1.

Figure 1. Picture of Long-wire antenna located in Equatorial Geophysical Research Laboratory (Tirunelveli).

Figure 2. Photograph of Electric Field Mill located in Equatorial Geophysical Research Laboratory (Tirunelveli).

Table 1. Number of fair-weather days considered for the study during the years 2020 and 2021

Date	Avg temp.	Mean wind speed	Wind direction	Mean humidity	Cloud coverage	Max. visibility
Pre–lockdown						
09/1/2020	24	3m/s	Easterly	74%	3octas	10km
15/1/2020	26	5m/s	Easterly	74%	2octas	12km
19/1/2020	25	2m/s	Easterly	74%	2octas	12km
11/2/2020	24	3m/s	Westerly	71%	3octas	14km
17/2/2020	25	4m/s	Easterly	71%	3octas	12km
18/2/2020	26	2m/s	Easterly	71%	3octas	12km
19/2/2020	28	4m/s	S-W	71%	2octas	13km
15/3/2020	30	4m/s	S-W	67%	3octas	14km
Lockdown						
16/04/2020	34	3m/s	16/04/2020	65%	2octas	14km
25/04/2020	34	3m/s	25/04/2020	62%	2ctas	14km
04/05/2020	36	4m/s	04/05/2020	59%	2octas	14km
(Pre – lockdown)						
18/01/2021	26	2m/s	N-W	72.3%	3octas	12km
19/01/2021	25	3m/s	Easterly	72.5%	3octas	10km
24/01/2021	25	3m/s	Easterly	72.8%	3octas	11km
25/01/2021	26	2m/s	N-W	73.7%	3octas	10km
27/01/2021	25	4m/s	N-W	66.7%	3octas	12km
28/01/2021	22	2m/s	Easterly	67%	2octas	12km
07/02/2021	24	3m/s	Easterly	69%	3octas	11km
08/02/2021	24	3m/s	Easterly	70.2%	3octas	12km
09/02/2021	26	4m/s	Easterly	73.9%	3octas	13km
10/02/2021	25	2m/s	Easterly	69.3%	3octas	12km
11/02/2021	26	2m/s	Easterly	70.8%	2octas	14km
12/02/2021	25	3m/s	Easterly	68.2%	3octas	13km
16/02/2021	27	3m/s	N-W	69.1%	3octas	12km
17/02/2021	27	2m/s	N-W	73.2%	2octas	13km
18/02/2021	24	4m/s	N-W	71.9%	3octas	10km
19/02/2021	26	4m/s	Westerly	68.2%	3octas	14km
26/02/2021	26	3m/s	Westerly	70.3%	2octas	12km
28/02/2021	27	3m/s	N-W	70%	2octas	13km
02/03/2021	26	4m/s	Easterly	59.9%	2octas	12km
03/03/2021	23	2m/s	Westerly	66.3%	2octas	12km
04/03/2021	24	2m/s	S-W	64%	2octas	11km
05/03/2021	24	3m/s	S-W	60%	3octas	12km
07/03/2021	26	3m/s	S-W	70.1%	3octas	13km
15/03/2021	27	5m/s	S-W	71.2%	2octas	12km
16/03/2021	29	5m/s	S-W	69.6%	1octas	14km
21/03/2021	31	4m/s	Variable	72.9%	1octas	13km
Lockdown						
17/04/2021	33	4m/s	S-W	60.6%	2octas	14km
19/04/2021	34	5m/s	Variable	63.2%	2octas	14km
23/04/2021	35	5m/s	Variable	61.9%	2octas	15km
24/04/2021	37	5m/s	S-W	60.8%	2octas	14km
25/04/2021	35	5m/s	S-W	70.1%	2octas	15km
02/05/2021	38	4m/s	N-W	66.5%	2octas	15km
Partial lockdown						
10/06/2021	36	5m/s	S-W	60.7%	3octas	13km
19/06/2021	36	5m/s	S-W	68.1%	3octas	13km
21/06/2021	38	4m/s	S-W	67%	3octas	14km
30/06/2021	38	5m/s	Variable	68.8%	3octas	13km

DATA AND METHODOLOGY

The electrodynamical state of the low-latitude ionosphere is well-known to be highly stable during fair-weather days; thereby, providing the sequential opportunities to measure the global impact of pollution on the AEP. The initial data selection process involved the assessment of a weather sheet that contains manual sky observations and AWS data to filter out any other disturbances owing to the weather. We have excluded the periods of high clouds of more than 3 octas, wind speed of more than 5 m/s, and days with precipitation. We also rejected the intervals of saturated and excessively turbulent data due to unknown reasons. Based on these, each resultant fair-weather day data comprising 86400 data points were selected for further analysis. Next, we carried out a 1-minute averaging of data. Such a strict data selection procedure resulted in 11 and 36 days of fair-weather data in 2020 and 2021, respectively, and is tabulated in Table 1. Next, we grouped observations into three categories namely, pre-lockdown, lockdown, and partial lockdown phases for further study. We have considered measurements during normal days and the complete lockdown phase in this study to understand the behavior of AEP.

RESULTS AND DISCUSSION

From Table 1, it is obvious that December to February is the coldest months in this region with an average temperature of 26^0C. During these months, the wind is mostly northeasterly with a typical speed of ~2-4 m/s so the electrodynamical state of the atmosphere is highly stable thereby, providing the sequential opportunities to measure the global impact of pollution on the AEP. It is noted that the relative humidity lies in the 52-76% range during this period. We also noticed fog coverage in the early morning hours during this period. During the mid-March-June period, we found (i) the humidity to decrease, (ii) an increase in temperature up to 36-42^0C, and (iii) rapid variation in the wind direction with its speed reaching up to 8 m/s or even more. Because of increased short-wave heating during these months, the surface temperature starts to increase up to 6^0 C from its base value, and the humidity drops. Since the surface temperature is the most important indicator of thermodynamical processes, this increased temperature during April-June causes a variation in advective and convective ways that result in a slight variation in electric field and current in mid-noon over this station.

Figure 3 shows the diurnal variation of averaged AE current density and averaged electric field observed at this station on 8 fair-weather days of the pre-lockdown period from January to March 2020. Plot (a) and (b) illustrate the variation of AE current density and ambient electric field, respectively. Diurnal variation clearly shows a positive trend of electric field/electric potential. Further, the electric field showed a phase variation with AE current which could be attributed to the variability of local conditions, columnar resistivity, temporal and spatial variability in the load resistance with respect to the sensor.

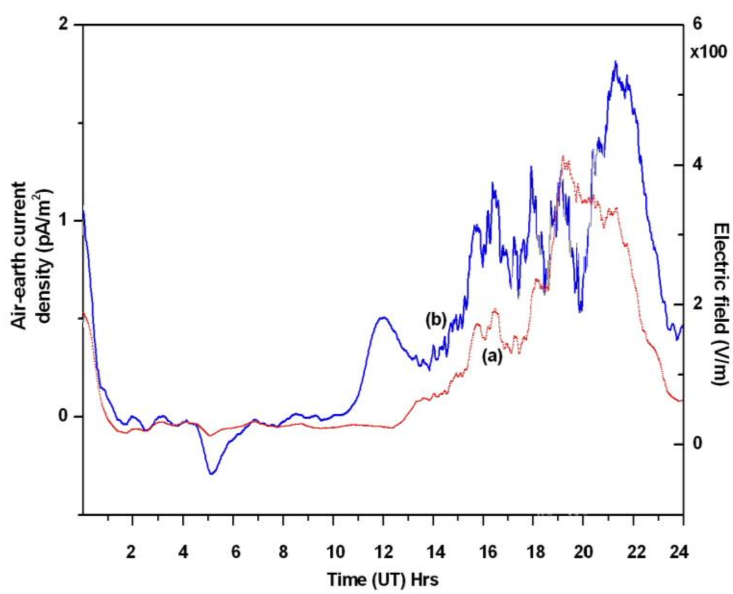

Figure 3. Diurnal variation of (a) averaged AE current density and (b) ambient electric field before lockdown (normal days) 2020 over Tirunelveli.

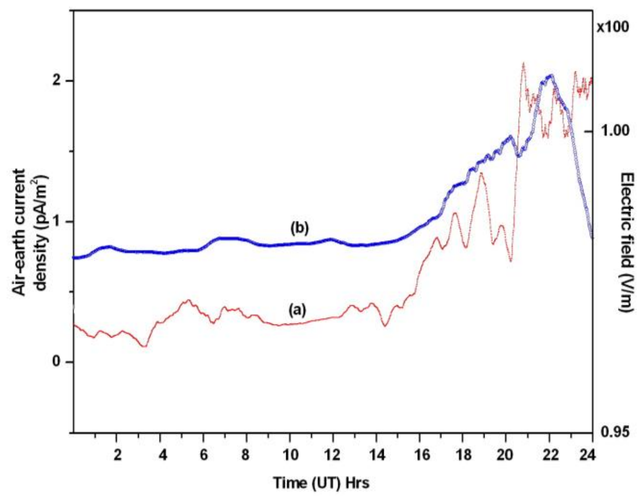

Figure 4. Average values of diurnal variation of (a) AE current density and (b) ambient electric field during lockdown 2020 over Tirunelveli.

Various combinations of the oceanic and continental thunderstorms source regions govern the global AEP pattern. When orography is suitable and aerosol concentration is less, the local factors produce small changes in AEP (Tinsley and Zhou, 2006). Another important factor is local weather. Meteorological parameters tabulated in Table 1 indicate that the wind speed had no significant influence during the period. In such fair-weather conditions, the principal component analysis suggested that the first Eigenvalue gives information about the thunderstorm's contribution to the global electric circuit (Panneerselvam et al., 2007). The study further indicated that the second and third components give information about the E-region ionosphere dynamo and the solar wind-magnetosphere dynamo, respectively. The currents and electric fields produced by the ionospheric wind dynamo are relatively weak. We present, in Figure 4, diurnal variation of electric field and AE current during lockdown-2020. We have taken the averaged variation of three fair-weather days and shown a half-hourly running mean.

In Figure 3, the electric field variations showed the lowest values at ~0500 UT; however, during the lockdown period, it occurred at ~0300 UT on most of the days and is widely accepted (Retails, 1991; Isrealsson and Tammet, 2001). We noted the prominent 1200 UT peak in the electric field (with values ~185 V/m) in Figure 3, which is linked with the South African thunderstorm chimney. However, its amplitude was comparatively smaller during lockdown days as seen in Figure 4. We found a few shallow peaks (with electric field ~100 V/m and AE current density ~1.35 pA/m^2) during 1600-1800 UT, which are connected with thunderstorm activity in the Mediterranean locations, Ukraine, and some Scandinavian countries. We also noted the usual 1900 UT prime peak in Figures 3 and 4, which are associated with the world thunderstorm activation. Its amplitude is dependent on the lightning activity in South America, Uruguay, Peru, and Ecuador. We found its' magnitude was ~300V/m (Figure 3); while, it was ~138 V/m during lockdown (Figure 4). On certain days, dual peaks were also noted between 1800 UT and 2200 UT, and the amplitude was shifted to a second higher peak in such cases which can be due to the change in global thunderstorm pattern due to climate variability.

We found the average AE current density of ~1.4 pA/m^2 and the electric field of ~140 V/m during the lockdown phase. It follows from the fact that the world anthropogenic pollution considerably reduced due to less human activity during the lockdown days, which affected the resistivity load in the GEC. A resistive load is defined as the resistance of the atmosphere from the Earth's terrain to the ionosphere and determines the AE current flow and electric field. It is the height integral of the reciprocal of the electric conductivity distributions. The major part of this resistance resides in the troposphere and strongly depends on the electrical conductivity variation due to the presence of aerosol, and pollution. From the variation depicted in the measured atmospheric electrical field and current in UT on two-dimensional diagrams (Figures 4 and 5), we calculated the amplitude ratio factor (Reddell et al., 2004) in the electric field to scale the signal strength of the fair-weather field. During the lockdown period, this amplitude ratio factor is in agreement with the Carnegie pattern.

Studies for each quartile indicate that the third quartiles had higher values. It implies that most of the thunderstorms are taking place during afternoon hours to pre-night hours. We found that the co-efficient of thunderstorm count range was (i) the highest during January to March 2020 in the pre-lockdown period, and (ii) was lesser during the lockdown phase. Using the following equation (1), Karl Pearson correlation coefficient (r) between the electric field and thunderstorm activity was computed and is provided in Table 2.

$$r = \frac{N\sum XY - (\sum X)(\sum Y)}{\sqrt{N\sum x^2 - (\sum X)^2} \quad x \quad \sqrt{N\sum y^2 - (\sum Y)^2}} \qquad (1)$$

where X is the value of the electric field and Y is the number of thunderstorms detected, N number of observations, x=X/10, and y=Y/100.

From Table 2, the quartiles define the three thunderstorm chimneys of the world. We found that the range co-efficient is in agreement with 1921 Carnegie cruises values (Fleming, 1949) during the lockdowns.

We found that these values signify maximum correlation in lockdown-2021; while, it was lowest during 2020, which may be due to lack of observation and the limited number of fair-weather days during the observational window.

We utilized 5° x 5° grid data of the World-Wide Lightning Location Network (WWLLN http://wwlln.net/) to identify the global hourly lightning count. Being limited by detectors, an absolute thunderstorm detection calculation may be difficult. It is noted that the lightning distribution peaks globally for the usual three lightning "chimneys"- America, Africa, and the Maritime continents. We compared the lightning events from January to March 2020 with that of April to June 2020 months. We found that the lightning events were higher (12%) from January to March. The pre-lockdown statistical weight of the signal ratio is not proportional to the world thunderstorm activity, which indicates the role of global load resistance. We repeated the observations during the second phase of this pandemic in 2021 since the thunderstorm strength is almost similar to that in 2020.

The results for the second phase of the pandemic in 2021 are depicted in Figures 5 and 6. It clearly indicates that resistivity varied during lockdown. Again, we carried out a comparative study with WWLLN lightning data from January to March and April 2021. Using the following equation (2), we determined the range co-efficient of the average diurnal curve since this ratio gives more reliability to the electric field/PG measurements, which are global.

Co-efficient of Range = (max.–min.)/(max.+min.) (2)

Overall estimated range co-efficient varied from 45 to 50 %, during the lockdown phase. When compared with the observations in 2020, the number of observations and positioning of the thunderstorm source regions were vivid during 2021. The plot in Figure 5 is based on 26 fair-weather days of pre-lockdown and Figure 6 is based on 10 fair-weather days in the lockdown period. As we know that the thunderstorm develops from cumulonimbus clouds, the condition for an overturning process is essential for the thunderstorm development. The characterization of this data set in Figure 5 shows that Malawi-Zimbabave-Zambia in the African continent had the peak thunderstorm activity between 1200 to 1400 UT, while in Figure 6 this time had been extended to Australia, where the thunderstorm regions include Daravia, New-south Wales, and Tasmania.

Table 2. Quartiles and Karl Pearson's Coefficient of correlation with Probable error.

State of the fair-weather day	Quartiles	Range	Co-efficient of range	Mean average	Karl Pearson's coefficient of correlation	Probable error
Before lockdown 2020	Q1 = 40.75 Q2 =136 Q3 = 352.5	370	0.9	147.5	.71 %	.07
During lockdown 2020	Q1 = 52.75 Q2 =55.5 Q3 = 83.5	80	0.5	64.7	0.57	.074
Before lockdown 2021	Q1 = 43 Q2 =56 Q3 = 182.5	80.79	0.68	80.79	0.84	.068
During lockdown 2021	Q1 = 138 Q2 =129 Q3 = 380	150	0.45	140	.88	.04

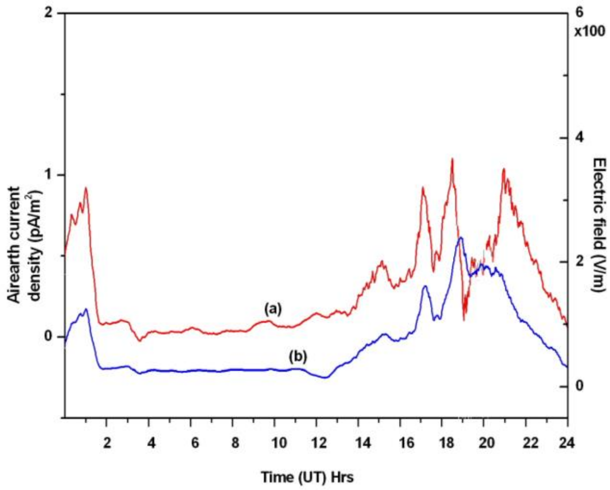

Figure 5. Average values of diurnal variation of AE current density and ambient electric field before lockdown 2021 over Tirunelveli, **(a)** AE current density, and **(b)** ambient electric field.

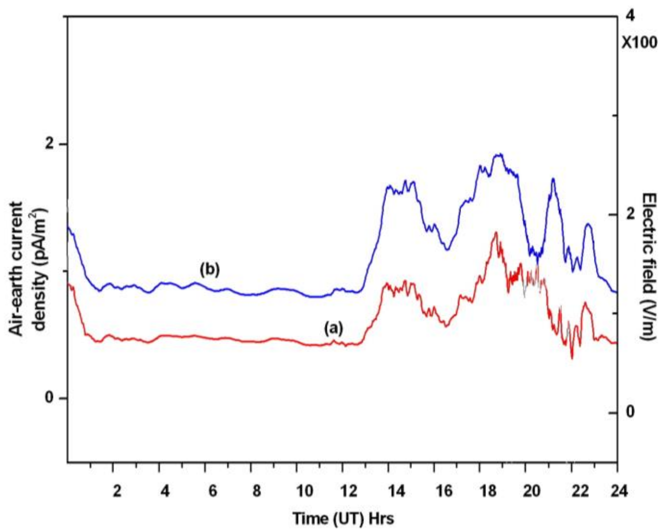

Figure 6. Average values of diurnal variation of (a) AE current density and (b) ambient electric field during lockdown during 2021

Figure 6 clearly shows the highest amplitude (2.6 pA) pattern in AE currents between 1900 and 2000 UT which indicates world lightning activity. The AE current and electric field were enhanced and followed phase coherence on most of the days during the 2021 lockdown. It is a good indicator of the stability of the columnar resistance. Since the vertical electric field is the most representative electrical parameter of local conductivity (Adlerman and Williams, 1996; Reddell et al., 2004). If the local conductivity remains constant with respect to the ground then the electric field/PG and current density must follow parallel to each other. Present observation is consistent with this aforesaid inference as well as the presence of a global continental signature in atmospheric electrical parameters measured over this station (Reddell et al., 2004).

As per the Karl Pearson's correlation coefficient, the relation between electric field and the number of thunderstorms in those fair-weather conditions is in good agreement with the principal component analysis carried out by Panneerselvam et al. (2007).

Again, we first scaled the measured half-hourly AE current values of the control day pre-lockdown say J (days, h) using the following equation (3). Next, the half-hourly average of AE currents values during lockdown selected day J_L (day) equaled the half-hourly average of variation in the control fair-weather day minus the daily half-hourly average of the scaled values.

$$\nabla J(\text{day}, h) = J\,(\text{pre-lockdown}; h) - J_L(\text{lockdown day}; h) \quad (3)$$

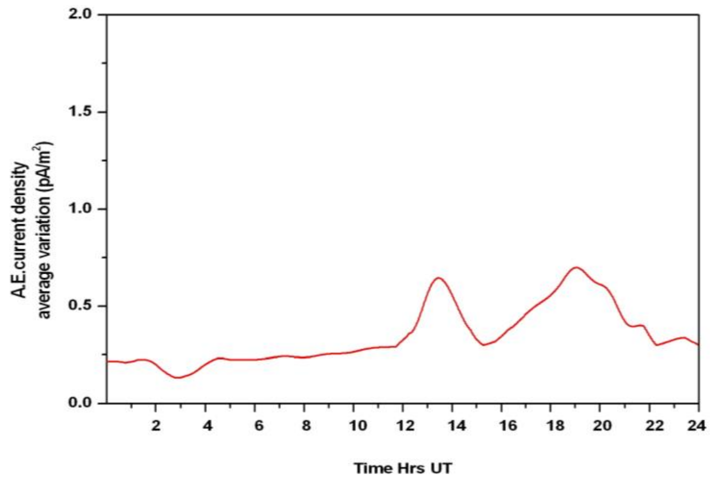

Figure 7. The plot shows enhancement in AE current density as per Eq.3.

A similar analysis of the atmospheric electric field and the AE current has been carried out earlier to measure ΔJ precisely (Frank-Kamenetsky et al., 2001; Burns et al., 2005). Figure 7 represents the results of this analysis. The resultant current variation has been attributed to the load resistance. In this case, the morning hours atmospheric electrical field ΔE_z corresponding was less and afternoon it was identified higher than 100V/m (Figure not included). A variation of 125 to 200 V/m is observed from 1300 UT to 1500 UT and further, from 1800 UT to 2100 UT, the ΔE_z almost remained the same. One-to-one correlation between vertical electric field and ΔJ_z is not always expected since both the variations are dependent on multiple factors in temporal and spatial scales; hence, an individual day is considered.

ΔJ_z varied from 0.4 pA/m^2 to 0.6 pA/m^2. From the above analysis, it is seen that the conductivity enhancement happened during the lockdown period. The decreased pollution rate is realized with the enhancement in AE current. On the other hand, the variability of load resistance responded with the variations of the large drops in the vertical electric resistance due to the dramatic decline in air pollution during the lockdowns.

CONCLUSIONS

We present here AEP measurements from Tirunelveli during 2020-2021. This epoch witnessed the pre-lockdown and lockdown periods of the first and second phases of the Covid-19 pandemic. The electric field and AE current variation during the lockdown period show an almost typical fair-weather pattern with a minimum around ~ 0300 UT and a peak around ~1900 UT. It is noted that the quartiles define the three thunderstorm chimneys of the world. Global distribution peaks usually at three lightning "chimneys"- Asia (Maritime Continents)-Australia, Africa-Europe, and South America. The range coefficient agrees with the Carnegie curve ratio of the observations of electric field and AE current during the lockdown periods. Karl Pearson's coefficient of correlation analysis connecting electric field/electric potential and the number of thunderstorms in fair-weather conditions is in good agreement with the principal component analysis. The study strongly supports that the pollution-less atmospheric processes contribute to an increase in fair-weather current density. In this comparative study, the enhancement in AE current indicates that the world anthropogenic pollution was considerably reduced due to less human activity during the lockdown times, which dramatically reduced the effective load resistance in GEC.

ACKNOWLEDGMENT

The authors are grateful to the Director, Indian Institute of Geomagnetism, Navi Mumbai for constant support and the Ministry of Science and Technology, Government of India, for the financial assistance. We would like to thank the referees for valuable comments and discussion of this paper.

Compliance with Ethical Standards

The authors declare no conflict of interest and adhere to copyright norms.

REFERENCES

Adlerman, E.J. and Williams, E.R., 1996. Seasonal variation of global electric circuit. J. Geophys. Res., 101, 29679-29688.

Anil Kumar, C.P., Panneerselvam, C., Nair, K.U., Jeyakumar, H.J., Selvaraj, C. and Gurubaran, S., 2009. Measurement of atmospheric air-earth current density from a tropical station using, improvised Wilson's plate antenna, Earth Planet and Space, 61, 919-926.

Anil Kumar, C.P., Gopal Singh, R., Selvaraj, C., Nair, K.U., Jeyakumar, H.J., Vishnu, R., Muralidas, S. and Balan, N., 2013. Atmospheric electric parameters and micrometeorological process during the solar eclipse on 15, January 2010, J. Geophys. Res. (Atmos) 118, 5098-5104, DOI: 10.1002/jgrd.50437.2013.

Anil Kumar, C.P., Venkatesh, N., Panneerselvam, C. and Selvaraj, C., 2020. Measurement Maxwell's current density from a tropical station during severe lightning disturbances and fair-weather days of 2019, J. Ind. Geophys. Union, 24(3), 25-31.

Arnold, F.H., Heitmann and Oberfrank, K., 1984. First composition measurements of positive ions in the upper troposphere, Planet. Space Sci., 32, 1567-1576.

Asir, A., 2021. Study of pollution levels during lockdown period in the southern region of Tamil Nadu (Personnel communication).

Bao, R., and Zhang, A., 2020. Does lockdown reduce air pollution? Evidence from 44 cities in northern China. Sci. Total Environ. 731, doi:10.1016/j.scitotenv.2020.139052

Burns, G.B., Frank-Kamenetsky, A.V., Troshichev, O.A., Bering, E.A. and Reddell, B.D., 2005. Interannual consistency of bi-monthly differences in diurnal variations of the ground level vertical electric field J. Geophys. Res. 110, D10106, doi:10.1029/2004JD005469.

Castleman, A., Tang, W.I.N. and Munkelwiz, H.R., 1971. Clustering of sulfur dioxide and water vapour about oxonium and nitric oxide ions., Amer. Assoc. Advanc. Sci., 173, 1025-1027.

Eisele, F.L., 1988. First tandem mass spectrometric measurement of tropospheric ions, J. Geophys. Res. 93, 716-724.

Frank-Kamenetsky, A.V., Troshichev, O.A., Burns, G.B. and Papitashvili, V.O., 2001. Variations of the atmospheric electric field in the near pole region related to the interplanetary magnetic field, J. Geophys. Res**.,** 106, 179-190.

Fleming, J.A., 1949. Physics of the Earth-Terrestrial Magnetism and Electricity, Dover publications, New York.

Gautam,S., 2020. The influence of Covid-19 on air quality in India: a boon or inutile Bulletin of Environmental Contamination and Toxicology, 104(6), 724-726.

Hoppel, W.A., Anderson, R.V. and Willet, J.C., 1986. Atmospheric electricity in the planetary boundary layer, The Earth electrical environment, 149-165, National academy press, Washington D.C.

Israelsson, S. and Tammet, H., 2001. Variation of fair-weather atmospheric electricity at Marsta Observatory, Sweden, 1993-1998, J. Atmos & Solar Terr. Phys., 63, 1693-1703.

Jonassen, N. and Wilkening, M.H., 1965. Conductivity and concentration of small ions in the lower atmosphere, J.Geophys. Res., 70, 779-784.

Junge, C.E., 1963. Air chemistry and radioactivity, Academic press., New York, 336-382.

Kanniah, K.D., Kamarul Zaman, N.A.F., Kaskaoutis, G.D. and Latif, M.T., 2020. Covid-19's impact on the atmospheric environment in the Southeast Asia region. Sci. Total Environ., 736**,** 139658. doi:10.1016/j. scitotenv2020.139658.

Kasemir, H.W., 1951. An apparatus for simultaneous registration of potential gradient and air-Earth current first results, J. Atmos. Terr. Phys, 2, 32-37.

Kasemir, H.W. and Ruhnke. L.H., 1959. Antenna problems of measurements of the air-Earth current, Recent advances in Atmospheric electricity, edited by L. G. Smith, Pergamon, New York, 37-147.

Kinoshita, H., Türkan, H., Vucinic, S., Naqvi, S., Bedair, R., Rezaee, R. and Tsatsakis, A., 2020. Carbon monoxide poisoning. Toxicology Reports 7, 169-173.

Mani, A. and Huddar, B.B., 1972. Studies of the surface aerosols and their effect on atmospheric electric parameters, Pure Appl. Geophys., 100, 154-166.

Nakada, L.Y.K. and Urban, R.C., 2020. COVID-19 pandemic: Impacts on the air quality during the partial lockdown in São Paulo state Brazil, Sci. Total Environ. 730, 139087, doi:10. 1016j.scitotenv.2020.139087.

Panneerselvam, C., Nair, K.U., Jeeva, K., Selvaraj, C., Gurubaran, S. and Rajaram, R., 2003. A comparative study of atmospheric Maxwell current and electric field from a low latitude station Tirunelveli, Earth Planets Space, 55, 697-703.

Panneerselvam, C., Selvaraj, C., Jeeva, K., Nair, K.U., Anil Kumar, C.P. and Gurubaran, S., 2007. Diurnal variation of atmospheric Maxwell current over the lower-latitude continental station, Tirunelveli, India, (8.7^0N, 77.8^0E), Earth Planet and Space, 59, 429-435.

Qu, Y.W., Han. Y., Wu, Y.H., Gao, P. and Wang, T.J., 2017. Study of PBLH and its correlation with particulate matter from one-year observation over Nanjing, Southeast China. Rem. Sens. 9(7), 66, doi.10.3390/rs9070668.

Reddell, B.D., Benbrook, J.R., Bering, E.A., Clearly, E.N. and Few, A.A., 2004. Seasonal variations of atmospheric electricity measured at Amundsen-Scott station, J. Geophys. Res.109 A 09308., 1-17, doi:10 1029/2004JA010536.

Resmi, C.T., Nishanth, T., Satheesh Kumar, M.K., Manoj, M.G., Balachandran M., and Valsaraj, K.T., 2020. Air quality improvement during the triple lockdown in the coastal city of Kannur, Kerala to combat Covid-19 transmission, Peer J., doi:10.7717/peerj.9642.

Retails, D.A., 1991. Study of the air-earth electrical current density in Athens, Pure Appl. Geophys., 136, 217-233.

Sharma.S., Zhang, M., Anshika, Gao, A.J., Zhang, H. and Kota, S.H., 2020. Effect of restricted emissions during COVID-19 on air quality in India. Sci. Total Environ. 728, 138878. doi:10.1016J.scitotenv.2020.138878.

Shi, X. and Brasseur G.P., 2020. The response in air quality to the reduction of Chinese economic activities during the COVID-19 Outbreak. Geophys. Res. Lett., 47(11), 1-8, DOI: 10.1029/2020GL088070.

Tinsley, B.A., and Zhou, L., 2006. Initial results of a global circuit model with variable stratospheric and tropospheric aerosols, J. Geophys. Res., 111, D16205, 1-23.

Tobías, A., Carnerero, C., Reche, C., Massagué J, Via M., Minguillón, M.C., Alastuey., A. and Querol, X., 2020. Changes in air quality during the lockdown in Barcelona (Spain) one month into the SARS-CoV-2 epidemic. Sci. Total Env. 726,138540, doi:10.1016/j. scitotenv.2020.138540.

Received on: 05.01.2022; Revised on: 26.04.2022; Accepted on: 09-05-2022

J. Ind. Geophys. Union, 26(3) (2022), 217-227

Nitrate contamination in groundwater of Coimbatore district (South India) and human health risk assessment

Karung Phaisonreng Kom[1*], B. Gurugnanam[1], and V. Sunitha[2]

[1]Centre for Applied Geology, The Gandhigram Rural Institute, Gandhigram, Dindigul-624302, Tamil Nadu, India
[2]Department of Geology, Yogi Vemana University, Kadapa-516005, Andhra Pradesh, India
[*]Corresponding author: phaikarung@gmail.com

ABSTRACT

This study aims to determine the nitrate (NO_3^-) concentrations in groundwater and their harmful effects on human health when consumed by drinking in the Coimbatore district, South India. For this purpose, 55 groundwater samples were collected through borewells during November and December 2020 from various parts of the study area. The results of the study revealed that 36.36% of the samples had NO_3^- concentration greater than the World Health Organization (WHO) recommended limit (50 mg/L) for drinking purposes. The relationship between the hydrochemical parameters and possible sources were studied using the principal component analysis (PCA) method. The results indicate that anthropogenic activities like excessive use of fertilizers, animal waste, septic tanks, municipal sewage, and wastewater may be responsible for the high nitrate (NO_3^-) content. The non-carcinogenic health hazards caused by high nitrate content in groundwater were calculated using the hazard quotient (HQ) model for adults, children and infants. The results suggest that 38.18% of samples for adults, 72.73% of samples for children, and 78.18% of samples for infants have an HQ value > 1 (safe value = less than or equal to 1). Therefore, the health risk assessment (HRA) indicates that infants and children in the study area are more susceptible to non-carcinogenic risks than adults. This finding could serve as a valuable guide for policy makers, which could help them better understand the groundwater quality and the non-carcinogenic risks caused by elevated nitrate in the region's groundwater.

Keywords: Nitrate contamination, Groundwater, Health risk assessment, Coimbatore, South India

INTRODUCTION

Groundwater is one of the most valuable natural resources in economic and social value. Globally, groundwater resources are continually depleted to meet the rising demand for freshwater. Since groundwater is generally considered safe for drinking than surface water as it is a concealed natural resource. Private and public wells become the primary drinking water sources for most rural residents in India. Unfortunately, the quality of groundwater resources has been seriously threatened by human activity and the industrial revolution over the last few decades (Chen et al., 2016). There are also many threats to groundwater resources worldwide, including climate change, land use, and population growth. Remediation becomes complex if the groundwater has been contaminated.

Nitrate is a significant pollutant released into groundwater naturally and also through human activity. A natural process may release nitrates into the groundwater from the weathering of nitratine, tobelite, and other nitrite-bearing rocks via rock-water interaction (Patel et al., 2020). However, numerous studies have reported that nitrate fertilizer used in agriculture is the primary cause of elevated nitrate in groundwater (Jayarajan and Kuriachan, 2021; Torres-Martínez et al., 2021). Fertilizers are used extensively in agricultural land areas because plants obtain nitrogen from nitrate, a readily available oxidized form of dissolved nitrogen. As a result of over-farming, soil loses its ability to retain water. Nitrogen fertilizers are often used to replace depleted soil nutrients. However, when these nitrates enter the food chain through groundwater and surface water, they threaten human health (Xiao et al., 2022). Several researchers have asserted that septic tanks, atmospheric inputs, livestock, and natural organic nitrogen all contribute to the contamination of groundwater with excessive nitrate levels, despite the widely held belief that commercial fertilizers are the primary source (Reddy and Sunitha, 2020; Kadam et al., 2020; Sunitha et al., 2012). The constant nitrogen flow from numerous pollution sources endangers groundwater and has become a global issue (Rao et al., 2018; Sreedevi et al., 2017; Wagh et al., 2020).

Groundwater with high nitrate concentrations can pose public health and environmental hazards, already a problem in many countries. A maximum nitrate concentration of 50 mg/L for drinking water has been recommended by the WHO (2011). In adults, thyroid dysfunction and hypertension are linked with more significant nitrate in drinking water (Adimalla and Li, 2019). Low oxygen levels in the blood caused by nitrate consumption in neonates can result in methemoglobinemia, also known as "blue baby" sickness (Spalding and Exner, 1993; Wang and Li, 2022). In addition, several forms of cancers, including gastric, colorectal, bladder, urothelial, and brain tumours, may be aggravated or worsened by long-term exposure to high levels of nitrates in water (Subba Rao, 2021). In India, many researchers have reported the high nitrate levels in groundwater in different states such as Tamil Nadu (Ramalingam et al., 2022), Punjab (Ahada and Suthar, 2018), Andhra Pradesh (Sunitha et al., 2021), Telangana (Duvva et al., 2022), Maharastra (Wagh et al., 2017) and Uttar Pradesh (Ahamad et al., 2018). More than 10.82 million people in India consume water containing high nitrate levels exceeding the permissible limit (Panneerselvam et al., 2021).

Coimbatore, known as the "Textile City of South India," is home to a thriving textile sector. Groundwater contamination in urban areas is a major concern, especially near industrial areas. An increasing population has impacted the groundwater quality in the urban region, and industrial activities like leather tanning, textiles, and foundries have affected the groundwater quality (Selvakumar et al., 2017). In rural areas, agricultural activities have adversely affected the groundwater quality. According to CGWB (2008), about 23% of the total geographical location of the region is under agricultural land. In addition, groundwater quality in the research area has deteriorated dramatically due to overuse and over-extraction (Kom et al., 2021). A few studies on nitrate contamination have been conducted in the Coimbatore district. Nitrate contamination of groundwater in the eastern Coimbatore city has been reported by (Karunanidhi et al., 2020a). Jayarajan and Kuriachan (2021) studied the NO_3^- content in groundwater and its health hazards in Coimbatore and Tirupur districts, Tamil Nadu. They concluded that children are more susceptible to non-carcinogenic threats than adults in their study. Excessive use of nitrogen fertilizers in agricultural land to yield more crops to meet the growing population needs in the country is to be blamed for the elevated nitrate level in groundwater (Bijay-Singh and Craswell, 2021). The main objective of this study is to focus on groundwater nitrate contamination and the health risks it poses to different age groups in the Coimbatore district, Tamil Nadu.

STUDY AREA

Coimbatore is one of the important districts of Tamil Nadu, which share a border with the state of Kerala, It lies between 10°13'18.38"N to 11°24'9.21"N and 76°59'4.72"E to 77° 6'33.36"E (Figure 1). Aliyar, Kousika, Noyyal and Bhavani are the main rivers that pass through the district. Dendritic drainage is the most common type in the study area (Figure 1). Parts of the Western Ghats are located in the southwest and north, which provide a pleasant climate year-round. Dissected hills and valleys, pediment-pediplain complex and bajada are among the geomorphic features found in the study area. The district has hard rock terrain belonging to the Archean age of rocks.

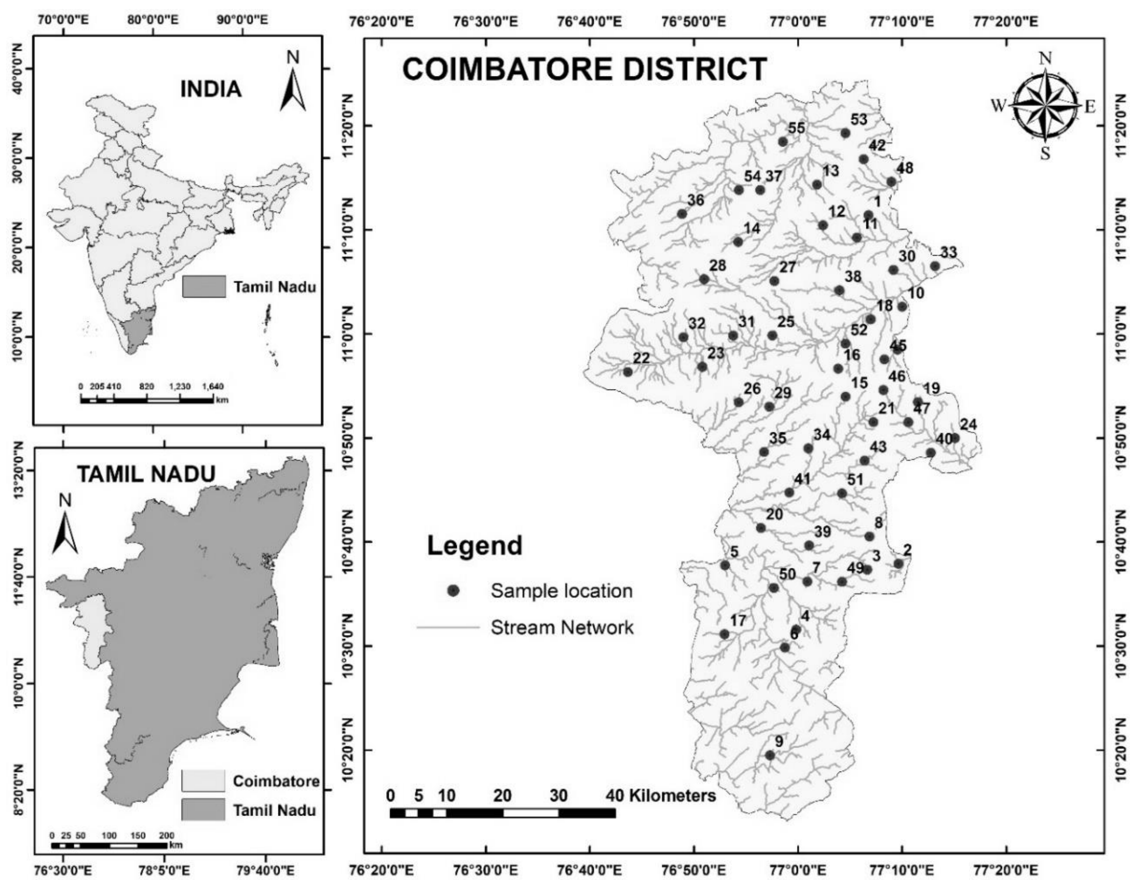

Figure 1. Location map of the study area in the Coimbatore district of Tamil Nadu, showing sampling points and drainage patterns.

The dominant rock type found in the study area is hornblende–biotite gneiss. Sedimentary deposits like kankar, alluviums, and colluviums have existed near the river banks (Kom et al., 2022). The aquifers in the study area range from Archaean to Recent alluvium (CGWB, 2008), and the thickness is highly variable, ranging from 10 to 40 metres below ground level (MoEF&CC, 2019). This region relies on borewells and open wells for domestic and agricultural use. The climate in this region is tropical, with temperatures ranging between 14° and 40° C (Kumar, 2021). Groundwater recharge is primarily provided by the NE monsoon, as the SW rains are insignificant. The study area receives an average annual rainfall of between 550 and 900 mm. (Jebastina and Arulraj, 2016). The soil types found in the study area are alluvial, colluvial black soil, brown soil, red soil and forest soil (Karunanidhi et al., 2020b).

METHODOLOGY

Fifty-five groundwater samples were collected during November and December 2020 to determine the groundwater chemistry; significantly, the NO_3^- level and its related health concerns in the Coimbatore district. The groundwater sampling and analysis procedures were carried out following the American Public Health Association (APHA, 2005) guidelines. All samples were collected from borewells and stored in pre-cleaned 1-litre polyethene bottles. During sampling, portable kits, such as Total dissolved solids (TDS), electrical conductivity (EC) and pH metres, were used to determine the TDS, EC and pH values. A UV-visible spectrophotometer was utilized to determine the nitrate and sulphate (SO_4^{2-}). Chloride (Cl^-), magnesium (Mg^{2+}), calcium (Ca^{2+}), total hardness (TH) and bicarbonate (HCO_3^-) were estimated at the laboratory by the titration method. Potassium (K^+) and sodium (Na^+) concentrations were determined using a flame photometer. The concentration of fluoride (F^-) was estimated using an ion-selective electrode method. The correlation matrix and Principal Component Analysis (PCA) were carried out through SPSS 16 software. The base map and spatial variation maps were prepared in ArcGIS 10.5, and Microsoft Excel was used to analyze the chemical data.

Health risk assessment (HRA)

The most widely used mathematical method for determining the possibility of health risks is human health risk assessment (HRA). This method effectively evaluates water quality, even when the pollutant levels are within the acceptable range (Shukla and Saxena, 2020). The US Environmental Protection Agency (USEPA, 1989) developed this approach to evaluate water quality and protect public health from various aspects of toxic substances (Adimalla et al., 2020). Nitrate has been categorized as a non-carcinogenic contaminant for human health by the USEPA. This study evaluated the human health hazards of nitrate via oral ingestion for infants, children and adults using equation 1.

$$CDI = C \times IR \times F \times ED / BW \times AT \quad \text{..... (1)}$$

Table 1 summarises the parameter values used to estimate the chronic daily intake.

The hazard quotient (HQ) of nitrate due to oral intake was calculated using equation 2.

$$HQ = CDI / RfD \quad \text{..... (2)}$$

Where, RfD specifies the reference dose; NO_3^-= 1.6 in mg/Kg × day (USEPA, 1989).

HQ ≤ 1 indicates no health risk to humans, while HQ > 1 signifies a higher level of hazard (**V**aiphei and Kurakalva, 2021)

Table 1. Parameters and input assumptions for evaluating non-carcinogenic health risk through an oral pathway.

Parameters	Unit	Male	Female	Children	Reference
Chronic daily intake (CDI)	mg/kg×day	-	-	-	(Yousefi et al., 2019)
Concentration of nitrate in groundwater (C)	mg/L	-	-	-	(Karunanidhi et al., 2020a)
Ingestion rate of water (IR)	L/day	1.5	1.5	0.9	(Mondal et al., 2012)
Exposure frequency (EF)	days/ years	365	365	365	(Chavoshi et al., 2011)
Exposure duration (ED)	year	30	30	12	(Haji et al., 2021)
Average body weight (BW)	Kg	70	55	15	(Adimalla et al., 2020)
Averaging time (AT)	day	10950	10950	4380	(Haji et al., 2021)

RESULTS AND DISCUSSION

Table 2 summarises the groundwater sample's statistical hydrochemical analysis results obtained in the Coimbatore district. The pH values of the samples varied from 7.7-8.8 (average 8.27), indicating alkaline groundwater. About 21.82% of the samples have a pH value above the WHO (2011)-permissible limit. The EC concentration in groundwater samples varied from 77-5705 μS/cm (mean = 1721.56 μS/cm), and the WHO permissible limit of 1500 mg/L was exceeded by 45.45% of the samples. The concentration of TDS was found between 57 and 3407 mg/L (average = 982.13 mg/L). The analysis revealed that 18.18% of samples exceeded the WHO recommended value of 1500 mg/L for drinking water. The range of TH concentrations is from 25-1511 mg/L, with an average concentration of 187.78 mg/L. The allowable limit of TH concentrations is 500 mg/L, exceeding 9.09% of the samples. Among the cations, the concentration of Na^{+} was most prevalent, followed by $Mg^{2+} > Ca^{2+} > K^{+}$. The order of anions identified based on the abundance in the groundwater samples were $HCO_3^- > Cl^- > SO_4^{2-} > NO_3^- > F^-$.

Nitrate and their spatial distributions

The nitrate concentration in the current investigated region varied from 2-135 mg/L (average 58.20 mg/L), as indicated in Table 2. A maximum nitrate level of 50 mg/L has been recommended by the WHO (2011). However, the study found that 36.36% of the collected water samples exceeded the allowable limit for drinking purposes. Excessive nitrate intake, especially for newborns, might be harmful. The spatial map of nitrate was created using the interpolation model in the GIS environment (Figure 2). The figure depicts that the nitrate concentration greater than 50 mg/L is located in the eastern and northeastern study areas. These regions are predominantly cultivated areas and settlement sites. This scenario for the study area indicates that agricultural inputs or sewage could have been a source of groundwater nitrate (Panda et al., 2022). On the other hand, nitrate level <50 mg/L is found in the southern, western and northern parts covering a vast study area.

Table 2. The descriptive statistical analysis of groundwater quality compared to WHO (2011) standard for drinking water.

Parameters	Units	Minimum	Maximum	Mean	Standard deviation	WHO (2011)			
						Highest desirable limit	Maximum permissible limit	No. of samples above the permissible limit	% of samples above the permissible limit
pH	-	7.7	8.8	8.27	0.29	6.5	8.5	12.0	21.82
EC	μS/cm	77	5705	1721.56	1297.24	750	1500	25	45.45
TDS	mg/l	57	3407	982.13	780.86	500	1500	10	18.18
TH	mg/l	25	1511	187.78	246.24	100	500	5	9.09
Ca	mg/l	10	211	60.02	47.75	75	200	2	3.64
Mg	mg/l	3	264	65.02	59.70	50	150	6	10.91
Na	mg/l	4	634	164.73	150.30		200	17	30.91
K	mg/l	2	205	43.84	49.42		12	37	67.27
HCO_3	mg/l	9	657	332.84	154.37				
Cl	mg/l	9	1843	279.35	327.97	200	600	8	14.55
SO_4	mg/l	5	395	96.98	100.10	200	400	NIL	NIL
NO_3	mg/l	2	135	58.20	43.76	50			
F	mg/l	0.05	1.92	0.87	0.51	0.5	1.5	6.00	10.91

* No. of samples above the WHO desirable limit for NO_3=20

*% of samples above the WHO desirable limit for NO_3=36.36%

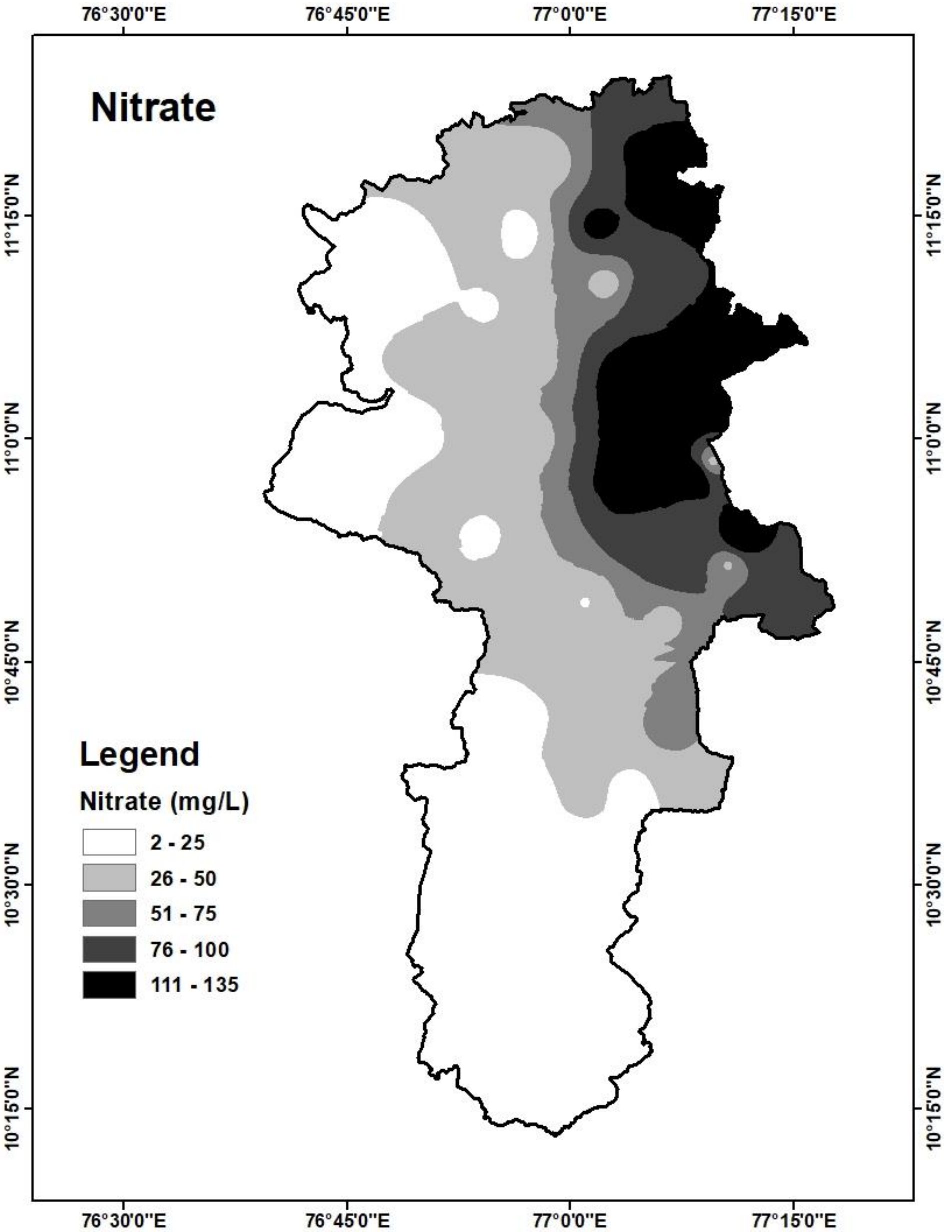

Figure 2. Spatial variation map of nitrate in groundwater of the study area.

Correlation Analysis

The correlation coefficient (*r*) is a mathematical expression that expresses the degree of relationship between two variables; an *r* value larger than or equal to 0.7 signifies a strong (high) correlation, between 0.3 and 0.7 as moderate and less or equal to 0.3 denotes a weak correlation (Zhang et al., 2020). A strong correlation between the hydrochemical parameters suggests that the geochemical behaviour and the source are similar (Ram et al., 2021). A correlation analysis between NO_3^- and other water quality parameters suggest a moderate positive correlation with EC, TDS, SO_4^{2-}, HCO_3^-, Cl^-, Na^+, Ca^{2+} and Mg^{2+} while a weak positive correlation with TH, K^+ and F^- (Table 3). A moderate correlation between NO_3^- and Cl^- indicates that human and animal wastes could be the source of elevated NO_3^- in groundwater (Rahman et al., 2021). On the other hand, a positive correlation with K^+ suggest that the high nitrate could result from sewage and excessive use of fertilizers (Zhang et al., 2020). The weak correlation with F^- indicate that nitrate content in groundwater is mainly an anthropogenic source, as fluoride contamination in groundwater is a geogenic (Subba Rao et al., 2020).

Table 3. Correlation matrix between various physical-chemical parameters.

	pH	EC	TDS	TH	Ca	Mg	Na	K	HCO_3	Cl	SO_4	NO_3	F
pH	1												
EC	-0.002	1											
TDS	-0.010	0.857	1										
TH	-0.183	0.625	0.705	1									
Ca	-0.225	0.621	0.735	0.851	1								
Mg	-0.046	0.585	0.689	0.254	0.492	1							
Na	0.068	0.639	0.800	0.354	0.369	0.363	1						
K	0.374	0.273	0.338	0.235	0.320	0.350	0.036	1					
HCO_3	0.221	0.492	0.469	-0.002	0.148	0.402	0.590	0.349	1				
Cl	-0.117	0.818	0.936	0.784	0.700	0.588	0.710	0.258	0.262	1			
SO_4	-0.072	0.714	0.819	0.731	0.720	0.551	0.574	0.166	0.289	0.734	1		
NO_3	-0.073	0.461	0.559	0.194	0.370	0.606	0.446	0.218	0.501	0.400	0.378	1	
F	0.344	0.225	0.011	-0.041	-0.030	0.033	0.017	0.210	0.317	-0.029	0.010	0.061	1

Principal component analysis (PCA)

The relationship between chemical parameters and possible sources can be depicted using the PCA technique (Rahman et al., 2021). In this analysis, the varimax rotation procedure was used to identify the relationship among factors. It was performed on 55 groundwater samples of the study area using 13 water quality parameters. Scree plots (Figure 3) and principal component loadings (Table 4) were used to analyze the hydrochemical features of groundwater samples. A total of three significant principal components (PC1, PC2 and PC3) were derived from the PCA, depending on their Eigenvalue greater than one (Table 4). The PC1, PC2 and PC3 have eigenvalues of 6.280, 1.999 and 1.246, respectively, and their total variance at 34.49%, 25.10%, and 13.68%, with a cumulative variance of 73.27%. Absolute loadings less than or equal to 0.50 were regarded weak; those between 0.75 and 0.50 were deemed moderate, and greater than or equal to 0.75 were considered strong or high (Kaur et al., 2020).

The PC1 show high positive loading of TH (0.959), Ca^{2+}(0.889), Cl^{-} (0.823) and SO_4^{2-} (0.781), suggesting that the source of high NO_3^{-} concentration may be derived from human activities like animal waste, municipality sewage and septic tanks (Zhang et al., 2020). The PC2 demonstrates high positive loading with NO_3^{-} (0.768), indicating that the source could be excessive fertilizer application in the agricultural areas. The PC3 has positive potassium loadings (0.706), indicating that sewage and manure are potential sources of high nitrate content in groundwater.

Evaluation of non-carcinogenic health risk

Nitrate has been categorized as a non-carcinogenic contaminant for human health by the USEPA and the International Agency for Research on Cancer (Rishi et al., 2020). As a result, the current study assessed the non-carcinogenic risk to human health from drinking nitrate-contaminated water using a risk assessment model developed by the USEPA (1989). Direct ingestion through drinking water and direct skin contact are the two main ways nitrate enters the human body. However, many studies have demonstrated that the risk of skin contact is minor compared to the risk of drinking water consumption (Moeini and Azhdarpoor, 2021). Hence, only nitrate exposure via the oral route is considered in this risk evaluation.

Hazard quotient (HQ) values for each of the groundwater samples examined in this investigation can be seen in Table 5. The HQ values found for adults, children and infants varies from 0.04-2.61 (average 1.12), 0.07-4.89 (average 2.11) and 0.12-7.90 (average 3.41), respectively. The recommended safe limit for HQ is ≤ 1.0, and higher than this specified limit (HQ>1.0) is considered to pose a non-carcinogenic risk to humans (USEPA 1989). The obtained result shows that 21 (38.18%) samples for adults, 40 (72.73%) samples for children and 43 (78.18%) samples for infants, respectively, have HQ values greater than 1 (Figure 4). The findings show that non-carcinogenic nitrate risks are more susceptible to infants and children than adults. This could be due to their lower body being more sensitive to nitrate contaminated water than adults.

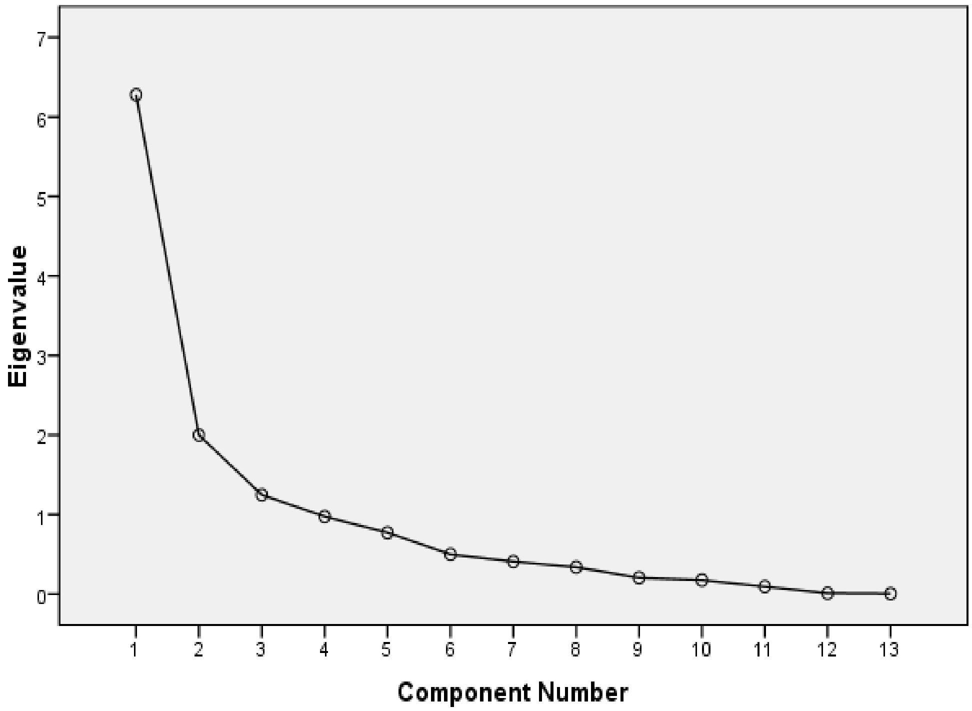

Figure 3. Scree plot of the eigenvalues.

Table 4. Varimax principal component loadings of groundwater samples.

	Principal component		
Parameters	PC1	PC2	PC3
pH	-0.164	0.011	0.787
EC	0.672	0.559	0.167
TDS	0.760	0.621	0.062
TH	0.959	-0.016	-0.037
Ca	0.889	0.161	-0.023
Mg	0.404	0.629	0.073
Na	0.356	0.748	-0.030
K	0.328	0.073	0.706
HCO_3	-0.028	0.798	0.382
Cl	0.823	0.439	-0.035
SO_4	0.781	0.385	-0.020
NO_3	0.170	0.768	-0.013
F	-0.059	0.100	0.687
Eigenvalue	6.28	1.999	1.246
% of Variance	34.492	25.099	13.675
Cumulative %	34.492	59.591	73.266

Table 5. Results of non-carcinogenic risk assessment for infants, children and adults based on hazard quotients.

Age groups	Hazard Quotient (HQ) ranged in the samples			Health risk	No. of samples	% of samples
	Minimum	Maximum	Mean			
Infants	0.12	7.90	3.41	HQ<1 (No risk)	43	78.18
				HQ>1 (High risk)	12	21.82
Children	0.07	4.89	2.11	HQ<1 (No risk)	40	72.73
				HQ>1 (High risk)	15	27.27
Adults	0.04	2.61	1.12	HQ<1 (No risk)	21	38.18
				HQ>1 (High risk)	34	61.82

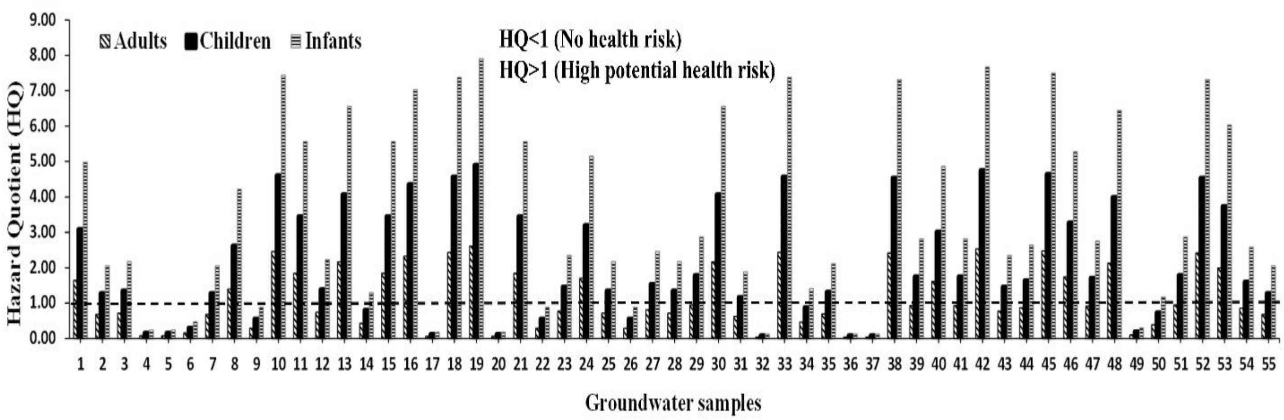

Figure 4. Statistical graph of nitrate causing non-carcinogenic hazards found in groundwater samples for adults, children and infants.

Methemoglobinemia (blue baby) in infants can be caused by excessive nitrate concentrations in groundwater (Sun et al., 2021). Hence, the groundwater must be treated before it is used for drinking to minimize nitrate causing non-carcinogenic hazards. The present study recommends improving drinking water quality and minimizing potential health hazards caused by high nitrate content, such as minimizing the usage of pesticides and fertilizers, the appropriate building of landfills and septic systems, and constructing artificial recharge systems in the Coimbatore district.

CONCLUSION

This study evaluated the concentrations of physicochemical parameters and the non-carcinogenic health risk caused by nitrate for different age groups (infants, children and adults) in the groundwater of Coimbatore district, Tamil Nadu. For this purpose, fifty-five groundwater samples through borewells were collected from different parts of the study area. The hydrochemical analysis revealed that all of the groundwater samples were alkaline. The study also found that sodium and bicarbonate were the most prevalent cation and anion in the groundwater samples. The nitrate content in the samples ranged between 2 and 135 mg/L (average 58.20 mg/L). About 36.36% of the samples surpassed the WHO desirable limit (50mg/L) for drinking water. The nitrate distribution map shows that the eastern and northeastern parts of the study area have the highest concentrations of nitrate, where agricultural land and build-up lands are predominant, indicating an anthropogenic source. The PCA results show that the high nitrate levels in groundwater are influenced by human activities such as the overuse of fertilizers, manure, septic tanks, and municipal sewage and wastewater. The USEPA method was used in this study to assess non-carcinogenic health risks posed by nitrate in different age groups. The HQ values found for adults, children and infants varies from 0.04-2.61 (average 1.12), 0.07-4.89 (average 2.11) and 0.12-7.90 (average 3.41), indicating 38.18%, 72.73% and 78.18% surpassed the threshold limit (HQ=1), respectively. The finding of this study indicates that infants and children are more vulnerable to non-carcinogenic hazards caused by nitrate than adults in the study area.

ACKNOWLEDGEMENTS

The authors express their sincere appreciation to the editor-in-chief and anonymous reviewers for their insightful comments and suggestions, significantly enhancing the manuscript.

Compliance with Ethical Standards

The authors declare no conflict of interest and adhere to copyright norms.

REFERENCES

Adimalla, N. and Li, P., 2019. Occurrence, health risks, and geochemical mechanisms of fluoride and nitrate in groundwater of the rock-dominant semi-arid region, Telangana State, India. Hum. Ecol. Risk Assess., 25, 81–103. DOI: 10.1080/10807039.2018.1480353.

Adimalla, N., Qian, H. and Nandan, M.J., 2020. Groundwater chemistry integrating the pollution index of groundwater and evaluation of potential human health risk: A case study from hard rock terrain of south India. Ecotoxicol. Environ. Saf., 206, 1-10. DOI: 10.1016/J.ECOENV.2020.111217.

Ahada, C.P.S. and Suthar, S., 2018. Groundwater nitrate contamination and associated human health risk assessment in southern districts of Punjab, India. Environ. Sci. Pollut. Res., 25, 25336–25347. DOI: 10.1007/S11356-018-2581-2.

Ahamad, A., Madhav, S., Singh, P., Pandey, J. and Khan, A.H., 2018. Assessment of groundwater quality with special emphasis on nitrate contamination in parts of Varanasi City, Uttar Pradesh, India. Appl. Water Sci., 8, 1–13. DOI: 10.1007/S13201-018-0759-X.

APHA, A., 2005. Stand. methods Exam. water wastewater. 21, 258–259.

Bijay-Singh and Craswell, E., 2021. Fertilizers and nitrate pollution of surface and ground water: an increasingly pervasive global problem. SN Appl. Sci., 34(3), 1–24. DOI: 10.1007/S42452-021-04521-8.

CGWB, 2008. District groundwater brochure Coimbatore district, Tamil Nadu. CGWB Technical report series.

Chavoshi, E., Afyuni, M., Hajabbasi, M.A., Khoshgoftarmanesh, A.H., Abbaspour, K.C., Shariatmadari, H. and Mirghafari, N., 2011. Health Risk Assessment of Fluoride Exposure in Soil, Plants, and Water at Isfahan, Iran. Hum. Ecol. Risk Assess., 17, 414–430. DOI: 10.1080/10807039.2011.552397.

Chen, J., Wu, H., Qian, H. and Gao, Y., 2016. Assessing Nitrate and Fluoride Contaminants in Drinking Water and Their Health Risk of Rural Residents Living in a Semiarid Region of Northwest China. Expo. Heal., 93(9), 183–195. DOI: 10.1007/S12403-016-0231-9.

Duvva, L.K., Panga, K.K., Dhakate, R. and Himabindu, V., 2022. Health risk assessment of nitrate and fluoride toxicity in groundwater contamination in the semi-arid area of Medchal, South India., Appl. Water Sci., 12, 1–21. DOI: 10.1007/S13201-021-01557-4.

Haji, M., Karuppannan, S., Qin, D., Shube, H. and Kawo, N.S., 2021. Potential Human Health Risks Due to Groundwater Fluoride Contamination: A Case Study Using Multi-Techniques Approaches (GWQI, FPI, GIS, HHRA) in Bilate River Basin of Southern Main Ethiopian Rift, Ethiopia. Arch. Environ. Contam. Toxicol., 80, 277–293. DOI: 10.1007/S00244-020-00802-2.

Jayarajan, P. and S.K., Kuriachan, L., 2021. Exposure and health risk assessment of nitrate contamination in groundwater in Coimbatore and Tirupur districts in Tamil Nadu, South India. Environ. Sci. Pollut. Res., 28, 10248–10261. DOI: 10.1007/s11356-020-11552-y.

Jebastina, N. and Arulraj, G.P., 2016. Contamination analysis of groundwater in Coimbatore district, India: a statistical approach. Environ. Earth Sci., 75, 1–12. DOI: 10.1007/S12665-016-6253-6.

Kadam, A.K., Umrikar, B.N. and Sankhua, R.N., 2020. Assessment of recharge potential zones for groundwater development and management using geospatial and MCDA technologies in semiarid region of Western India. SN Appl. Sci., 2, 1–11. DOI: 10.1007/S42452-020-2079-7.

Karunanidhi, D., Aravinthasamy, P., Roy, P.D., Praveenkumar, R.M., Prasanth, K., Selvapraveen, S., Thowbeekrahman, A., Subramani, T. and Srinivasamoorthy, K., 2020a. Evaluation of non-carcinogenic risks due to fluoride and nitrate contaminations in a groundwater of an urban part (Coimbatore region) of south India. Environ. Monit. Assess., 192, 1–16. DOI: 10.1007/S10661-019-8059-Y.

Karunanidhi, D., Aravinthasamy, P., Deepali, M., Subramani, T., Bellows, B.C. and Li, P., 2020b. Groundwater quality evolution based on geochemical modeling and aptness testing for ingestion using entropy water quality and total hazard indexes in an urban-industrial area (Tiruppur) of Southern India. Environ. Sci. Pollut. Res., 28, 18523–18538. DOI: 10.1007/S11356-020-10724-0.

Kaur, L., Rishi, M.S. and Siddiqui, A.U., 2020. Deterministic and probabilistic health risk assessment techniques to evaluate non-carcinogenic human health risk (NHHR) due to fluoride and nitrate in groundwater of Panipat, Haryana, India. Environ. Pollut., 259, 1–11. DOI: 10.1016/J.ENVPOL.2019.113711.

Kom, K.P., Gurugnanam, B. and Sunitha, V., 2022. Delineation of groundwater potential zones using GIS and AHP techniques in Coimbatore district, South India. Int. J. Energy Water Resour., 1–25. DOI: 10.1007/S42108-022-00188-Y.

Kom, K.P., Gurugnanam, B., Sunitha, V., Reddy, Y.S. and Kadam, A.K., 2021. Hydrogeochemical assessment of groundwater quality for drinking and irrigation purposes in western Coimbatore, South India. Int. J. Energy Water Resour., 1–20. DOI: 10.1007/S42108-021-00138-0.

Kumar, P.J.S., 2021. Groundwater fluoride contamination in Coimbatore district: a geochemical characterization, multivariate analysis, and human health risk perspective. Environ. Earth Sci., 80, 1–14. DOI: 10.1007/S12665-021-09521-W.

MoEF&CC, 2019. District survey report for granite, Coimbatore district, Ministry of Forest and Climate Change.

Moeini, Z. and Azhdarpoor, A., 2021. Health risk assessment of nitrate in drinking water in Shiraz using probabilistic and deterministic approaches and impact of water supply. Environ. Challenges 5, 1-16. DOI: 10.1016/J.ENVC.2021.100326.

Mondal, N.K., Pal, K.C. and Kabi, S., 2012. Prevalence and severity of dental fluorosis in relation to fluoride in ground water in the villages of Birbhum district, West Bengal, India. Environ., 321(32), 70–84.

Panda, B., Chidambaram, S., Snow, D., Malakar, A., Singh, D.K. and Ramanathan, A.L., 2022. Source apportionment and health risk assessment of nitrate in foothill aquifers of Western Ghats, South India. Ecotoxicol. Environ. Saf. 229, 1-9. DOI: 10.1016/J.ECOENV.2021.113075.

Panneerselvam, B., Karuppannan, S. and Muniraj, K., 2021. Evaluation of drinking and irrigation suitability of groundwater with special emphasizing the health risk posed by nitrate contamination using nitrate pollution index (NPI) and human health risk assessment (HHRA). Hum. Ecol. Risk Assess. An Int. J., 27, 1324–1348. DOI: 10.1080/10807039.2020.1833300.

Patel, P.M., Saha, D. and Shah, T., 2020. Sustainability of groundwater through community-driven distributed recharge: An analysis of arguments for water scarce regions of semi-arid India. J. Hydrol. Reg. Stud., 29, 1-10. DOI: 10.1016/J.EJRH.2020.100680.

Rahman, A., Mondal, N.C. and Tiwari, K.K., 2021. Anthropogenic nitrate in groundwater and its health risks in the view of background concentration in a semi-arid area of Rajasthan, India. Sci. Rep., 11, 1–13. DOI: 10.1038/s41598-021-88600-1.

Ram, A., Tiwari, S.K., Pandey, H.K., Chaurasia, A.K., Singh, S. and Singh, Y. V., 2021. Groundwater quality assessment using water quality index (WQI) under GIS framework. Appl. Water Sci., 11, 1–20. DOI: 10.1007/S13201-021-01376-7.

Ramalingam, S., Panneerselvam, B., and Kaliappan, S.P., 2022. Effect of high nitrate contamination of groundwater on human health and water quality index in semi-arid region, South India. Arab. J. Geosci., 153(15), 1–14. DOI: 10.1007/S12517-022-09553-X.

Rao, N.S., Sunitha, B., Rambabu, R., Rao, P.V.N., Rao, P.S., Spandana, B.D., Sravanthi, M. and Marghade, D., 2018. Quality and degree of pollution of groundwater, using PIG from a rural part of Telangana State, India. Appl. Water Sci., 8, 1–13. DOI: 10.1007/S13201-018-0864-X.

Reddy, B.M. and Sunitha, V., 2020. Geochemical and health risk assessment of fluoride and nitrate toxicity in semi-arid region of Anantapur District, South India. Environ. Chem. Ecotoxicol., 2, 150–161. DOI: 10.1016/J.ENCECO.2020.09.002.

Rishi, M.S., Kaur, L. and Sharma, S., 2020. Groundwater quality appraisal for non-carcinogenic human health risks and irrigation purposes in a part of Yamuna sub-basin, India. Hum. Ecol. Risk Assess., 26, 2716–2736. DOI: 10.1080/10807039.2019.1682514.

Selvakumar, S., Chandrasekar, N. and Kumar, G., 2017. Hydrogeochemical characteristics and groundwater contamination in the rapid urban development areas of Coimbatore, India. Water Resour. Ind., 17, 26–33.

Shukla, S. and Saxena, A., 2020. Appraisal of Groundwater Quality with Human Health Risk Assessment in Parts of Indo-Gangetic Alluvial Plain, North India. Arch. Environ. Contam. Toxicol., 801(80), 55–73. DOI: 10.1007/S00244-020-00771-6.

Spalding, R.F. and Exner, M.E., 1993. Occurrence of Nitrate in Groundwater-A Review. J. Environ. Qual., 392–402.

Sreedevi, P.D., Ahmed, S. and Reddy, D. V., 2017. Mechanism of Fluoride and Nitrate Enrichment in Hard-Rock Aquifers in Gooty Mandal, South India. Environ. Process., 4, 625–644. DOI: 10.1007/S40710-017-0254-7.

Subba Rao, N., 2021. Spatial distribution of quality of groundwater and probabilistic non-carcinogenic risk from a rural dry climatic region of South India. Environ. Geochem. Health, 43, 971–993. DOI: 10.1007/S10653-020-00621-3.

Subba Rao, N., Ravindra, B. and Wu, J., 2020. Geochemical and health risk evaluation of fluoride rich groundwater in Sattenapalle Region, Guntur district, Andhra Pradesh, India. Hum. Ecol. Risk Assess., 26, 2316–2348. DOI: 10.1080/10807039.2020.1741338.

Sun, X., Zheng, Q., Xiong, L., Xie, F., Li, X., Li, Y., Zhang, L., Saud, S., Guo, Z., Yan, Y., Wu, H., Liu, Q., Cui, G. and Chen, Y., 2021. Nitrogen assimilation and gene regulation of two Kentucky bluegrass cultivars differing in response to nitrate supply. Sci. Hortic., 288, 1-15. DOI: 10.1016/J.SCIENTA.2021.110315.

Sunitha, V., Reddy, B.R. and Reddy, M.R., 2012. Groundwater quality evaluation with special reference to fluoride and nitrate pollution in Uravakonda, Anantapur District, Andhra Pradesh—a case study. Int J Res Chem Env., 2, 88–96.

Sunitha, V., Reddy, Y.S., Suvarna, B. and Reddy, B.M., 2021. Human health risk assessment (HHRA) of fluoride and nitrate using pollution index of groundwater (PIG) in and around hard rock terrain of Cuddapah, A.P. South India. Environ. Chem. Ecotoxicol., 4, 113-123. DOI: 10.1016/J.ENCECO.2021.12.002.

Torres-Martínez, J.A., Mora, A., Mahlknecht, J., Daesslé, L.W., Cervantes-Avilés, P.A. and Ledesma-Ruiz, R., 2021. Estimation of nitrate pollution sources and transformations in groundwater of an intensive livestock-agricultural area (Comarca Lagunera), combining major ions, stable isotopes and MixSIAR model. Environ. Pollut., 269, 1-15. DOI: 10.1016/J.ENVPOL.2020.115445.

USEPA, 1989. Risk Assessment Guidance for Superfund, Volume I: Human Health Evaluation Manual (Part A), Office of Emergency and Remedial Response, Washington, DC.

Vaiphei, S.P. and Kurakalva, R.M., 2021. Hydrochemical characteristics and nitrate health risk assessment of groundwater through seasonal variations from an intensive agricultural region of upper Krishna River basin, Telangana, India. Ecotoxicol. Environ. Saf., 213, 1-16. DOI: 10.1016/j.ecoenv.2021.112073.

Wagh, V., Mukate, S., Muley, A., Kadam, A., Panaskar, D. and Varade, A., 2020. Study of groundwater contamination and drinking suitability in basaltic terrain of Maharashtra, India through PIG and multivariate statistical techniques. J. Water Supply Res. Technol., 69, 398–414. DOI: 10.2166/AQUA.2020.108.

Wagh, V.M., Panaskar, D.B. and Muley, A.A., 2017. Estimation of nitrate concentration in groundwater of Kadava river basin-Nashik district, Maharashtra, India by using artificial neural network model. Model. Earth Syst. Environ., 3, 1–10. DOI: 10.1007/S40808-017-0290-3.

Wang, Y. and Li, P., 2022. Appraisal of shallow groundwater quality with human health risk assessment in different seasons in rural areas of the Guanzhong Plain (China). Environ. Res. 207, 112210. DOI: 10.1016/J.ENVRES.2021.112210.

WHO, G., 2011. Guidelines for drinking-water quality. World Heal. Organ. 216, 303–304.

Xiao, Y., Hao, Q., Zhang, Y., Zhu, Y., Yin, S., Qin, L. and Li, X., 2022. Investigating sources, driving forces and potential health risks of nitrate and fluoride in groundwater of a typical alluvial fan plain. Sci. Total Environ. 802, 149909. DOI: 10.1016/J.SCITOTENV.2021.149909.

Yousefi, M., Ghalehaskar, S., Asghari, F.B., Ghaderpoury, A., Dehghani, M.H., Ghaderpoori, M. and Mohammadi, A.A., 2019. Distribution of fluoride contamination in drinking water resources and health risk assessment using geographic information system, northwest Iran. Regul. Toxicol. Pharmacol., 107, 1-8. DOI: 10.1016/J.YRTPH. 2019.104408.

Zhang, M., Huang, G., Liu, C., Zhang, Y., Chen, Z. and Wang, J., 2020. Distributions and origins of nitrate, nitrite, and ammonium in various aquifers in an urbanized coastal area, south China. J. Hydrol., 582, 1-18. DOI: 10.1016/J. JHYDROL.2019.124528.

Received on: 19.02.2022; Revised on: 11.04.2022; Accepted on: 12.04.2022

J. Ind. Geophys. Union, 26(3) (2022), 228-238

Hydrogeochemistry and groundwater evaluation in and around Badel, Y.S.R Kadapa district, Andhra Pradesh (India)

B.Muralidhara Reddy[1], V. Sunitha[2*], B.Suvarna[2], Y.G. Sai Sudha[2], and K. Sai Krishna[3]

[1]Department of Earth Sciences, Yogi Vemana University, Kadapa-516005, Andhra Pradesh, India
[2]Department of Geology, Yogi Vemana University, Kadapa-516005, Andhra Pradesh, India
[3]Department of Geology, Kakatiya University, Warangal, Telangana-506009, India
[*]Corresponding author: vangalasunitha@gmail.com

ABSTRACT

This study intends to evaluate hydrogeochemical properties of groundwater for drinking and irrigation purpose in and around Badvel area of Y.S.R Kadapa district (Andhra Pradesh). To accomplish this objective, twenty five groundwater samples were collected and analyzed for quality parameters viz pH, EC, TDS, TH, Ca^{2+}, Na^{+}, K^{+}, CO_3^{2-}, HCO_3^{-}, SO_4^{2-}, Cl^{-}, NO_3^{-} and F^{-}. Most of the groundwater samples are above the safe limits of W.H.O standards. Total dissolved solids (TDS), total hardness (TH), electrical conductivity (EC), chloride, sulphates, fluoride, nitrate levels in groundwater are beyond acceptable limits. The Gibbs plot indicates that groundwater samples fall within the field of rock dominance which is the predominant hydrogeochemical factor controlling the water chemistry. Piper's diagram reveals that water is of Na^{+}-K^{+}-Cl^{-}-SO_4^{2-} type. Agricultural water quality indices like percent sodium, sodium adsorption ratio, kellys ratio, magnesium hazard, permeability index, potential salinity, soltan classification were also determined. Percent sodium (% Na) of 80% of water is under doubtful class. 36% of groundwater samples are unsuitable for irrigation with respect to magnesium hazard. 100% of groundwater belongs to undoudtful category in terms of Permeability Index (PI), Potential Salinity (PS) and Kelly's Ratio (KR). Based on our study, majority of groundwater samples fall under the unsuitable category for drinking and irrigation purposes and requires proper groundwater management techniques.

Keywords: Hydrogeochemistry, Groundwater quality, Percent Sodium, Sodium Adsorption Ratio, Badvel, Y.S.R Kadapa District.

INTRODUCTION

For the long-term growth, there must be reliable and easy access to safe drinking water. The chemical and physical quality of water determines its suitability for various purposes. Groundwater chemistry is primarily influenced by natural and manmade factors. Groundwater's hydrochemical properties are influenced by the lithological and geochemical composition through subsurface movement (Elango et al., 2003). Its percolation through pore spaces and weathered formations can cause changes in various hydrochemical properties (Rajmohan and Elango 2004; Brindha and Elango, 2012). Groundwater chemistry can be also be influenced by a variety of anthropogenic factors, including point sources such as waste disposal and sanitary conditions (Amoako et al., 2011; Brindha and Elango, 2015). The efficient assessment of physico-chemical parameters, their origin, and the regulation of hydrogeochemical operations are critical for the ecosystem's long-term viability. Many workers have studied physicochemical and hydrochemical factors to assess the features of groundwater (Sanchez Martos et al., 1999; Subbarao et al., 2002; Bharadwaj and Singh 2011; Sredevi et al., 2018). Due to the lack of a suitable water source, groundwater is considered of fundamental importance. As a result, groundwater quality has become one of the most pressing environmental concerns (Ravichandra and Chandana 2006). In India, groundwater is the primary source of drinking water for both urban and rural populations. In rural places, groundwater accounts for more than 88 percent of clean drinking water (Jain et al., 2010). Groundwater is used for agriculture and industrial purposes in addition to drinking. In today's world, advanced pumping techniques have created a demand for groundwater. As surface water pollution worsens, groundwater extraction rises dramatically, resulting in increased groundwater pollution and abuse. Because people rely on groundwater for a variety of uses, the quality of drinking water has a direct impact on public health. It is critical to keep track of it in a methodical manner. Increased irrigation methods could also pollute groundwater (Pawar and Shaikh, 1995). Groundwater irrigates 39 million hectares in India, it accounts for approximately 80% of residential use and more than 45 percent in agriculture (Kumar et al., 2005). Groundwater is considered the only substantial and viable source of water for irrigation activities in India (Kinzelbach et al., 2003).

As per the available information groundwater pollution is caused by a variety of factors including geogenic and anthropogenic pollution, nitrogen pollution, agricultural practices, and the dissolution of rocks and soil (Guo et al., 2007; Elango et al., 2012; Sunitha et al., 2016, 2018, 2022; Sunitha and Reddy, 2022; Adimilla and Venkatayogi 2017; Sreedevi et al., 2019). Several researchers have carried out groundwater quality investigations, viz, (Arumugam and Elangovan, 2009; Sreedevi et al., 2017, 2018; Sunitha and Reddy, 2019; Sudharshan Reddy et al., 2018, 2020). Understanding the geochemical evolution of groundwater is critical for the long-term development of semi-arid water resources region like Badvel in the Y.S.R Kadapa District (Figure 1), where groundwater is the primary source of water for drinking and agriculture. The main objective of this paper is to assess the suitability of groundwater for drinking and irrigation purposes using integrated approaches

.STUDY AREA

Schists, amphibolites, granites, and doleritic rock formations make up the research area. Granites have encroached on schists and amphibolites on a huge scale. Basic igneous rocks intruded in the granites and earlier mentioned rocks as dykes. Dolerites are commonly used to symbolise these dykes. Ferruginous loam is the soil type. This soil is usually of poor quality and barely reaches a few inches below ground level. Weathered shales, fractured shales, and phyllites follow the top soil, which has a thickness of 1-2 m. The primary rivers running through Badvel are the Sagileru and the Penna, both of which are not ephemeral. In the Badvel town area, the average rainfall is around 700 mm. Here, the temperature ranges from 20 to 45^0C.

METHODOLOGY

Twenty five groundwater samples were collected from borewells in and around Badvel Mandal of Y.S.R Kadapa District, A.P during March 2020. In order to evaluate the suitability of water for drinking and irrigation water quality parameters like pH, electrical conductivity, TDS, total hardness, Ca^{2+}, Mg^{2+}, Na^+, K^+, CO_3^{2-}, HCO_3^-, Cl^-, SO_4^{2-}, NO_3^-, F^- and various irrigational quality indices like percent sodium (%Na), sodium adsorption ratio (SAR), residual sodium carbonate (RSC), permeability index(PI), magnesium ratio(MR), Kelly's ratio (KR) were used. The techniques and methods adopted for collection and parameter analytical are based on Hem (1985), Raghunath (1987), Karanth (1989), and APHA (2012). The data is depicted in Table 1.

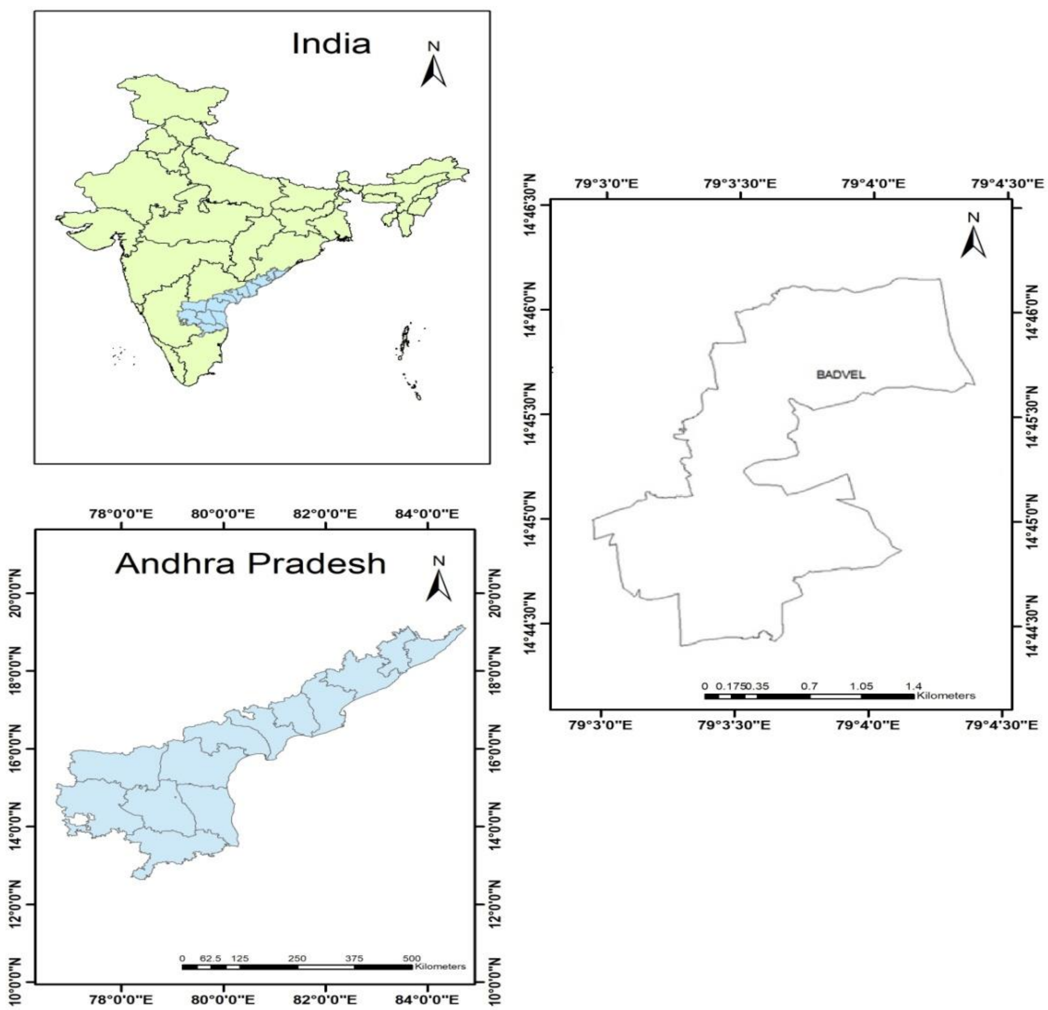

Figure 1. Location map of the study area

RESULTS AND DISCUSSION

The results of chemical analysis were shown in Table 1. pH is important in classifying many types of geochemical equilibrium (Hem 1985). The pH of groundwater varies from 7 and 9.3, indicating that it is alkaline. All of the samples' pH levels are within acceptable ranges (WHO 2011). Water with a pH of more than 8.5 or less than 6.5 can cause aesthetic impacts including staining and etching, as well as equipment scaling. At 25°C, the electrical conductivity of groundwater ranges from 560 to 3200 µS/cm, indicating that there are more salts in the water. Higher electrical conductivity could be caused by high mineral content and higher salinity at the study site, as well as temperature, ion types and the concentration of electrical conductivity increases as TDS concentration increases (Hem 1985). EC is classified as type I if the salt enrichment is modest (EC:1500 µS/cm), type II if the salt enrichment is medium (EC:1500-3000 µS/cm), and type III if the salt enrichment is large (EC> 3000 µS/cm).

According the classification of electrical conductivity, 64% of samples fall into type I (low salt enrichment), 24% of samples fall into type II (medium salt enrichment) and the remaining 12% of samples fall into type III (high salt enrichment) category. Higher electrical conductivity variations could possibly be caused by geochemical processes and anthropogenic activities in this area (Subba Rao, 2017; Narasimha and Sudarshan, 2013).

Table1. Analytical data of the groundwater samples of the Badvel region

S.No	pH	EC	TDS	TH	Na^+	K^+	Ca^{2+}	Mg^{2+}	CO_3^{2-}	HCO_3^-	Cl^-	SO_4^{2-}	NO_3^-	F^-
1	8.4	3200	2100	70	130	100	70	40	40	160	230	230	60	1.8
2	7.9	2300	1320	82	180	140	76	45	28	158	240	240	68	2.2
3	7.8	1250	810	64	140	80	80	50	38	162	180	190	70	1.9
4	8	1750	1100	23	280	170	84	36	18	170	190	220	72	1.6
5	8.2	2100	1200	43	230	200	75	58	18	220	320	450	135	4.2
6	8.4	1320	800	42	260	190	78	60	20	210	380	140	58	3.6
7	8.5	1850	900	46	190	170	64	56	22	230	430	210	54	3.8
8	8.3	1200	850	38	200	190	68	70	24	190	420	230	60	2.9
9	8.4	1120	760	28	210	180	70	45	26	160	500	190	48	1.9
10	8.2	980	870	28	320	210	90	38	14	170	180	170	45	2.4
11	8.3	1200	670	34	300	230	220	40	18	80	150	310	60	2.2
12	7.8	3100	530	86	520	340	120	46	20	120	160	340	80	2.8
13	8.4	2800	530	34	420	290	130	50	22	110	230	320	86	2.6
14	8.2	3100	540	76	500	400	140	55	14	60	220	170	90	2.4
15	7	1300	340	46	380	210	110	38	16	80	280	160	110	1.8
16	8.3	1200	320	110	330	240	90	40	18	70	400	150	80	1.7
17	9.3	1530	380	45	430	300	80	45	25	180	160	140	85	1.8
18	8.2	1200	320	60	420	320	70	46	22	190	170	380	87	2.4
19	8.4	1260	430	63	310	290	75	50	20	200	90	340	84	2.3
20	7.8	1300	560	43	300	190	68	30	18	130	180	380	78	3
21	7.6	1400	820	60	210	110	72	45	24	180	130	400	80	2.8
22	7.8	1200	540	45	240	180	90	36	30	230	150	310	130	2.3
23	8	1200	580	60	410	200	95	38	28	220	130	240	130	1.2
24	8.4	1320	670	58	180	160	120	40	26	200	280	190	110	1.3
25	8.6	560	340	54	230	200	110	48	28	180	230	180	100	1.2

(*All parameters are expressed in mg/L ; EC in µS/cm and pH as no units)

Similarly, total dissolved solids range from 320 mg/L to 2100 mg/L (Table 2), with 1% of samples surpassing the allowed limit and rendering them unfit for human consumption. All inorganic salts, such as carbonates, bicarbonates, chlorides, fluoride, sulphates, nitrates, calcium, magnesium, sodium and potassium are included in total dissolved solids in water (Sawyer, 1994). According to the United States Geological Survey (USGS), 84% of groundwater samples are classified as freshwater, while 16% are classified as mildly saline (Table 3). TDS levels are high due to salt leaching from the soil as well as sewage percolation into the groundwater. According to WHO (2011), drinking water with a palatability of less than 600 mg/L is beneficial for human health, while water with a palatability of more than 1000 mg/L is unappealing and majority of the samples fall into this category. Total hardness ranges from 23 to 110 mg/L. Sawyer et al. (2003) classified groundwater with TH <75, 75-150, 150-300, > 300 mg/L as soft, moderately hard, hard and very hard, respectively (Table 3). Based on this, 84% of the samples are classified as safe, while 16% are classified as moderately hard or hard. Groundwater hardness is caused by calcium and magnesium. Carbonate (CO_3^{2-}), bicarbonate (HCO_3^-) in groundwater varies from 14 - 40 mg/L and 60-230 mg/L with a median value of 23 and 162 mg/L, respectively. The majority of the groundwater samples are below the 300 mg/L standard (WHO, 1990; Table 2). The concentration of chlorides in groundwater ranges from 90 to 500 mg/L, with a median of 241 mg/L. Higher chlorides are commonly used as a pollution indicator and as a tracer for groundwater contamination (Loizidou and Kapetanios 1993). Shand (1952) indicated that residual water contained in pores of granites or within the crystals of rocks may contain chloride. Higher chloride concentrations are also caused by leaching of upper soil layers by home, municipal, and industrial pollutants, as well as dry climate (Subba Rao, 2017). Sulfates in the studied region range from 140 to 450 mg/L, with an average of 251 mg/L, showing that the majority of the groundwater is below the 200 mg/L limit. Sodium concentrations in groundwater range from 130 to 520 mg/L. 76% of groundwater exceeds the WHO's recommended level of 200 mg/L. The increase in Na^+ is related to the leaching of the deposit and the breakdown of certain minerals. When water comes into contact with igneous rocks, sodium gets dissolved from its natural source. Industrial and municipal waste releases, as well as run-off from diffuse sources, can all contribute to sodium entering natural rivers. Because of the high salt concentration, soil structure and permeability may be harmed, resulting in alkaline soils. Excess sodium in drinking water reduces its potability, yet water with up to 1000 mg/L may be medically tolerated (Ramesh and Anbu, 1996). Increased salt levels in drinking water, on the other hand, cause hypertension, arteriosclerosis, oedema, hyperosmolarity, renal, and neurological system diseases in humans.

High sodium levels are not recommended for agricultural poerations since they degrade the soil (Sarath Prashanth et al., 2012). Groundwater potassium concentrations range from 80 to 400 mg/L, with a median of 211 mg/L. According to WHO (1990), the allowed maximum of K^+ in drinking water is 12 mg/L and all of the samples are above this limit. The concentration of calcium in groundwater ranges from 64 to 220 mg/L, with a median of 93 mg/L (Table 2). Calcium levels in drinking water are limited to 75 mg/L (WHO, 1990). The calcium limit in groundwater is exceeded in 64% of the time. Magnesium concentrations ranged from 30 to 70 mg/L (Table 2). Magnesium levels in groundwater must not exceed 30 mg/L for drinking purposes (WHO, 1990). The majority of the samples exceed the magnesium regulatory limit. Nitrate levels in groundwater range from 45 to 135 mg/L. According to WHO guidelines, 4% of groundwater samples have nitrate concentrations over the allowed level (45 mg/L). Agricultural activity, septic tank leakage and home sewage all contribute towards higher nitrate concentrations (Datta and Tyagi, 1996; Muralidhara Reddy et al., 2019, Muralidhara Reddy and Sunitha, 2020). Nitrate poisoning causes not only methaemoglobinamia in babies, but also cancer, birth defects, stomach cancer, goitre, and hypertension (Dissanayake et al., 1987; Bao et al., 2017; Fan 2011). Fluoride in the range of 0.8-1.0 mg/L is beneficial to human health in terms of avoiding dental cavities and aiding enamel formation in children under the age of eight. If the groundwater contains more than 1.5 mg/L of fluoride, it produces dental fluorosis and skeletal fluorosis if the water is consumed continuously for 8-10 years. Fluoride in the range of 0.8-1.0 mg/L is beneficial to human health in terms of avoiding dental cavities and aiding enamel formation in children under the age of eight. Dental fluorosis manifests itself most prominently in youngsters under the age of 12. Dental fluorosis has been reported in Vemula, Y.S.R Kadapa District, Kadapa (Sunitha and Srinivasulu, 2015); Kadapa, Anantapur District (Sunitha et al., 2013); Badvel, Y.S.R Kadapa District (Sunitha et al., 2014); and in and around abandoned mines in Vemula, Y.S.R Kadapa District (Sunitha et al., 2018). The maximum fluoride content of 4.2 mg/L was found in Veerapalli, while the lowest fluoride concentration of 1.2 mg/L was found at Ramakrishnapuram and Badvel town North.

Gibbs diagram

The mechanism influencing groundwater chemistry in the Badvel region is assessed using Gibb's diagram. Precipitation dominance (PD), rock dominance (RD) and evaporate dominance (ED) are depicted as a function of TDS for $Na^{+}+K^{+}/Na^{+}+K^{+}+Ca^{2+}$ and $Cl^{-}/Cl^{-}+HCO_3^{-}$ (ED) (Gibb's, 1970). Figures 2a,b show the plots of all groundwater samples. The figures show that all of the groundwater samples were in the rock dominance (RD) zone, indicating that rock weathering and dissolution of fluoride-bearing minerals from the source rock are the primary causes of fluoride release into groundwater (Sunitha et al., 2012; Faten et al., 2016; Thomas et al., 2016).

Table 2. Comparison of the quality parameters of groundwater samples of the study area with WHO standards

Parameter	Units	Minimum	Maximum	W.H.O (2011)		Sample numbers exceeding the permissible limit	No.of samples
				Desirable Limit	Permissible Limit		
pH		7	9.3	6.5-8.5	9.2	Nil	Nil
EC	µS/cm	560	3200	750	1500	1,2,4,5,7,12,13,14,17	9
TDS	mg/L	320	2100	500	1500	1	1
TH	mg/L	23	110	100	500	Nil	Nil
Na^{+}	mg/L	130	520	50	200	4,5,6,9,10,11,12,13,14,15,16, 17,18,19, 20,21,22,23,25	19
K^{+}	mg/L	80	400	-	200	10,11,12,13,14,15,16,17,18,19	10
Ca^{2+}	mg/L	64	220	75	200	11	1
Mg^{2+}	mg/L	30	70	30	150	Nil	Nil
CO_3^{2-}	mg/L	14	40	-	-	Nil	Nil
HCO_3^{-}	mg/L	60	230	500	500		
Cl^{-}	mg/L	90	500	250	600	Nil	Nil
SO_4^{2-}	mg/L	140	450	2.5	375	5,18,20.21	4
NO_3^{-}	mg/L	45	135	-	45	1,2,3,4,5,6,7,8,9,11,12,13,14,15, 16,17,18,19,20,21,22,23,24,25.	24
F^{-}	mg/L	1.2	4.2	0.5	1.5	1,2,3,4,5,6,7,8,9,10,11,12,13, 14,15,16, 17,18,19,20,21,22.	22

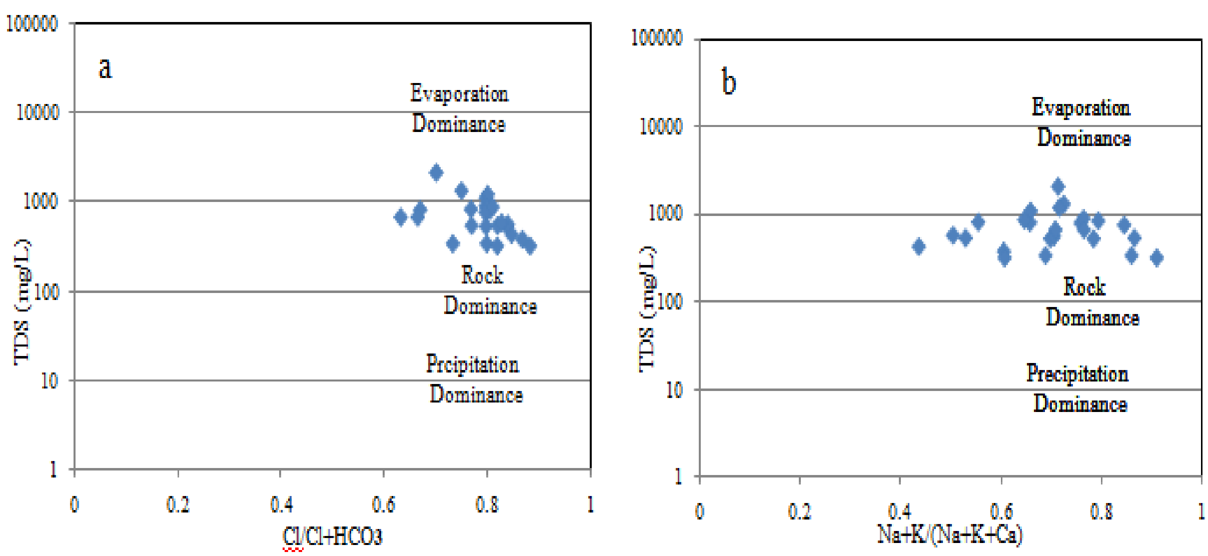

Figure 2. Mechanism controlling groundwater chemistry for study area (a) TDS vs. $(Cl^{-})/(Cl^{-} + HCO_3^{-})$. (b) TDS vs. $(Na^{+}+K^{+})/(Na^{+}+K^{+}+Ca^{2+})$

Hydro-geochemical facies

Piper (1953) trilinear graphic shows the hydro geochemistry regime of groundwater by showing main cations and anions. Geochemical evolution can be studied from the Piper's plot which is further categorized in to four groups namely Ca^{2+}-Mg^{2+}-SO_4^{2-}, Na^+-K^+-Cl^--SO_4^{2-}, Na^+-K^+-Cl^- -HCO_3 and Ca^{2+}-Mg^{2+}-HCO_3^-. Majority of the samples in the study area belongs to Na^+-K^+-Cl^--SO_4^{2-} type (Figure 3).

Classification of groundwater for irrigation purposes

The sodium percentage (%Na; Wilcox 1955), Sodium adsorption ratio (SAR; Richards, 1954); Residual sodium carbonate (RSC; Eaton, 1950; Raghunath, 1987), Magnesium hazard Ratio (MHR; Raghunath, 1987), Kelly ratio (KR; Kelly, 1940) and permeability Index (PI) (Doneen, 1964) are some of the methods used to determine the suitability of groundwater for agricultural/ irrigation practices.

Percent Sodium (%Na)

The sodium in irrigation waters is usually denoted as Percent sodium and can be determined by the following formula (Wilcox, 1955).

$$\text{Percent sodium} = \frac{Na^+ + K^+}{Ca^{2+} + Mg^{2+} + Na^+ + K^+} \times 100$$

Na, Ca, Mg and K are taken in meq/L. It is observed that based on percent sodium, 80% of water is under doubtful class, 20% belongs to permissible class (Eaton, 1950). %Na ranges between 54 mg/L to 78 mg/L with the median value of 66 mg/L.

Sodium Adsorption Ratio (SAR)

Sodium concentration assessment is crucial for the assessment of irrigation. Increased sodium in soils substitutes calcium and magnesium from them by making hard and compact causing to reduced infiltration and poor internal drainage (Karanth, 1987; Todd, 1980). The SAR (Sodium adsorption ratio) is determined by the equation:

$$SAR = \frac{[Na^+]}{\sqrt{\frac{[Ca^{2+} + Mg^{2+}]}{2}}}$$

where the concentrations are expressed in meq/L. The greater the value of SAR, the grater is the hazard to the crops due to excess sodium. SAR values ranges from 3.025212 to 10.23332. 96% in groundwater and thus belong to excellent category while 4% of the groundwater belongs to good category (Richards, 1954).

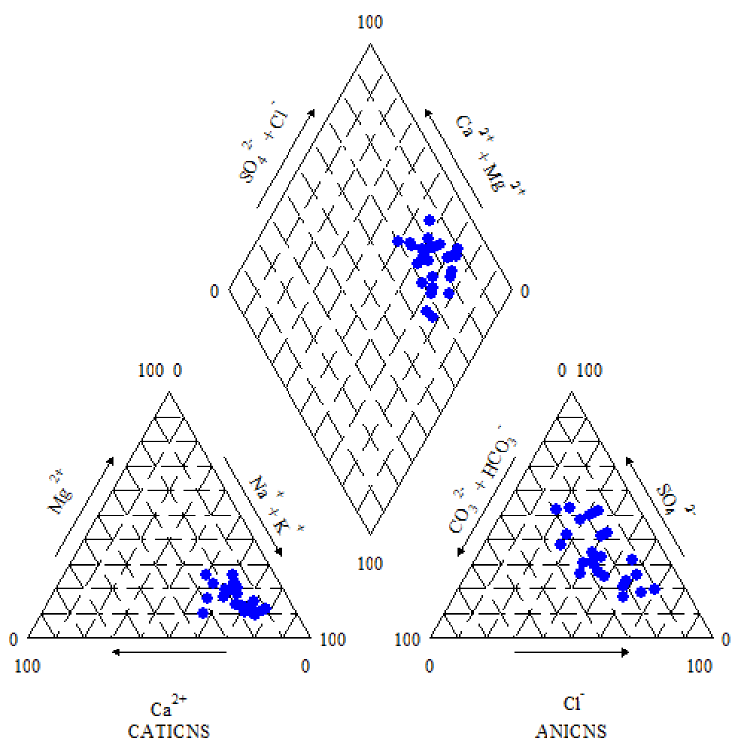

Figure 3. Piper trilinear diagram for the chemical composition of groundwater samples in the study area

Table 3. Groundwater classification based on irrigational water quality parameters

Parameter	Classification	Range	No.of Samples	% of Samples	Reference
TDS	Fresh water	<1000	21	84	US Geological Survey (2000)
	Slightly saline	1000 - 3000	4	16	
	Moderatly saline	3000 - 10000	Nil	Nil	
	High Saline	10000-35000	Nil	Nil	
TH	Safe	<75	21	84	Sawyer et al.(2003)
	Moderate Hard	75-150	4	16	
	Hard	150-300	Nil	Nil	
	Very hard	>300	Nil	Nil	
%Na	Excellent	<20	Nil	Nil	Eaton (1950)
	Good	20-40	Nil	Nil	
	Permissible	40-60	5	20	
	Doubtful	60-80	20	80	
	Unsuitable	>80	Nil	Nil	
KI/KR	Suitable	<1	5	20	Kelley (1940)
	Unsuitable	>1	20	80	
PI	Suitable	>75%	Nil	Nil	Doneen (1964)
	Good	25-75%	Nil	Nil	
	Unsuitable	<25%	25	100	
MH	Suitable	<50	16	64	Szabolcs and Darab (1964)
	Unsuitable	>50	9	36	
PS	Suitable	<3	Nil	Nil	Doneen (1962)
	Unsuitable	>3	25	100	
SAR	Excellent	<10	24	96	Richards (1954)
	Good	10-18	1	4	
	Doubtful	18-26	Nil	Nil	
	Unsuitable	>26	Nil	Nil	
RSC/RA	Good	<1.25	25	100	Eaton (1950)
	Doubtful	1.25-2.5	Nil	Nil	
	Unsuitable	>2.5	Nil	Nil	

Residual sodium carbonate (RSC)

Residual sodium carbonate can be determined by subtracting the alkaline earth (Ca^{2+} + Mg^{2+}) from the carbonate (CO_3^{2-} + HCO_3^-). Water containing high concentrations of carbonate and bicarbonate ions tends to precipitate calcium and magnesium as their carbonates. Hence the relative proportion of sodium in water is increased in the form of sodium carbonate and this is indicated by RSC, which can be calculated as follows (Eaton, 1950; Raghunath, 1987).

$$RSC = (CO_3^{2-} + HCO_3^-) - (Ca^{2+} + Mg^{2+})$$

According to the above classification, water >2.5 meq/L of RSC is not suitable for irrigation. Based on RSC classification (Eaton 1950) 100% of samples fall in the good category.

Magnesium hazard (MH)

Calcium and magnesium maintain a state of equilibrium in most waters, A high level of Mg^{2+} is generally due to the presence of exchangeable Na^+ in irrigated soils. The excess Mg^{2+} alters the quality of soil making it alkaline ensuing decreased crop yield and poor agricultural returns. Mg hazard is determined by the equation:

$$\text{Magnesium Hazard (MH)} = Mg^{2+} \times 100/ (Ca^{2+} + Mg^{2+})$$

MR value <50 is suggested for irrigation while MR value >50 is not suggested for irrigation thereby decreasing the crop yield (Szabolcs and Darab, 1964). The Mg hazard in this region ranges between 23.06 to 62.92 (Table 3). 64% of groundwater samples are within Mg hazard while 36% of groundwater samples are unsuitable for irrigation.

Permeability index (PI)

Permeability index is an important parameter for classifying irrigation water permeability of the soils and is inclined by prolonged application of irrigation water (higher salts) as it is influenced by Na^+, Ca^{2+}, Mg^{2+}, and HCO_3^- ions in soils. Doneen (1964) developed permeability index PI which is determined by the equation:

$$PI = (Na^+ + \sqrt{HCO^-_3} \times 100) / (Ca^{2+} + Mg^{2+} + Na^+)$$

(where all the ions are expressed in meq/l). PI values of this region range from 3.63– 13.47. PI is divisible into three classes. Class I (75 Suitable), Class II (25-75% good) and Class III (25% and less, unsuitable). 100% of groundwater belongs to Class III.

Potential salinity (PS)

Potential salinity is applied for categorization of water for agricultural purpose. PS <3 meq/l is good for agricultural applications (Doneen, 1962).100% of the samples belong to the unsuitable class. PS can be calculated by the following equation.

$$PS = Cl^- + 0.5\times SO_4^{2-}$$

Soltan classification

Soltan (1999) classified groundwater into base-exchange indices (r1) and meteoric genesis indices (r2) as given below:

$$r1 = (Na^+ - Cl^-)/ SO_4^{2-}$$

$$r2 = [(K^+ + Na^+)-Cl^-]/SO_4^{2-}$$

where Na^+, K^+, Cl^-, SO_4^{2-} concentrations are expressed in meq/L. If r1<1 and r2<1, groundwater is of Na^+ - SO_4^{2-} and deep meteoric type, respectively whereas r1>1 and r2>1 shows the source are of Na^+-HCO_3^- and shallow meteoric type respectively (Table 3). As per Soltan classification, 100% groundwater belongs to Na^+- CO_3^{2-}, deep meteoric type.

Kelly's ratio (KR)

Kelly's ratio signifies higher content of sodium in water (Kelly 1940). It is also one of the vital parameters in classifying irrigation water. KR index is alkali hazard indicator. In case of high KR values gypsum is advised to decrease the effects of Na^+ ion.

KR is determined by formula

$$KR = Na^+/ (Ca^{2+} + Mg^{2+})$$

KR values of the groundwater sample range from 0.66 to 3.68 with the average value of 1.88. Water within KR < 1 is suitable for irrigation while water within KR >1 is unsuitable. As per table 3, 20% of the values fall in a suitable class and 80% fall in unsuitable class for irrigation. It is clear that most of the water samples are not suitable for irrigation.

CONCLUSION

In the study area, groundwater is the primary source of drinking water. The current study examined the groundwater quality for drinking and irrigation in the Badvel region of Y.S.R Kadapa District (A.P. South India). The groundwater is naturally alkaline. TDS, TH, EC, chloride, sulphates, fluoride, nitrate levels in groundwater are beyond acceptable limits. High chloride concentrations could be caused by leaching of top soil layers by domestic, municipal, and industrial wastes, as well as residual water in pores of granite. Fluoride distribution in groundwater (0.25-2.93 mg/L) has been associated to high levels of fluorosis. Fluoride ions are released or exchanged by hydroxyl ions when sodium, bicarbonate and an alkaline pH are increased (OH-). The main contributors to fluoride release in groundwater are rock weathering and dissolution of fluoride-bearing minerals from the source rock. Agricultural operations, septic tank leakage and sewage from this area all contribute to the high concentration of nitrates. Based on TDS classification according to US Geological Survey most of groundwater samples are slightly saline. Gibbs diagram reveal that all of the groundwater samples were in the rock dominance (RD) zone, indicating that rock weathering and dissolution of fluoride-bearing minerals from the source rock are the primary causes of fluoride release into groundwater. Agricultural yields are low in lands irrigated with water belonging to doubtful and unsuitable category. MH reveals that 66.66% of groundwater samples are harmful and unsuitable for irrigation. KR values reveal that 86.6 % fall in unsuitable category for irrigation. PS indicates that 25% of groundwater samples fall in unsuitable class. Hence based on above irrigational quality parameters, it can be concluded that groundwater fall under unsuitable class for irrigation and application of this untreated water may be harmful for the crops and decreases the crop yield. However more saline tolerant crops could be suggested to combat soil salinization and application of lime or gypsum may be suggested to bout the soil permeability. This will play a significant role for effective management of the available water resources, and hence sustainable socio-economic development of the region.

ACKNOWLEDGEMENTS

The autors are greatful to the editor and anonymous reviewers for suggestions and comments which improved manuscript significantly

Compliance with Ethical Standards

The authors declare no conflict of interest and adhere to copyright norms.

REFERENCES

Adimalla, N. and Venkatayogi, S., 2017. Mechanism of fluoride enrichment in groundwater of hard rock aquifers in Medak, Telangana State South India. Environ. Earth Sci., 76, 45. https ://doi.org/10.1007/ s1266 5-016-6362-2

Arumugam, K., and Elangovan, K., 2009. Hydrochemical characteristics and groundwater quality assessment in Tirupur region, Coimbatore district, Tamil Nadu, India. Envi. Geo., 58(7),1509. https://doi.org/10.1007/s00254

APHA., 2012. Standard methods for the examination of water and wastewater, 22nd edn. American Public Health Association, New York.

Amoako, J., Karikari, A.Y. and Ansa-Asare, O.D., 2011. Physico-chemical quality of boreholes in Densu Basin of Ghana. Appl. Water. Sci., 1, 41–48

Brindha, K. and Elango, L., 2012. Impact of Tanning Industries on Groundwater Quality near a Metropolitan City in India Water Resour. Manage., 26, 1747–1761. DOI 10.1007/s11269-012-9985-4.

Brindha, K. and Elango, L., 2015. Cross comparison of five popular groundwater pollution vulnerability index approaches, J. of Hydrol. doi: http://dx.doi.org/10.1016/j.jhydrol.2015.03.003

Bhardwaj, V. and Singh, D.S., 2011. Surface and groundwater quality characterization of Deoria District, Ganga Plain, India. Environ. Earth Sci., 63, 383–395.

Bao, Z., Hu, Q., Qi, W.,Tang, Y., Wang, W., Wan, P., Chao, J. and Yang, X.J., 2017. Nitrate reduction in water by aluminium alloys particles. J. Environ. Manag., 196, 666-673.

Datta, P.S. and Tyagi, S.K., 1996. Major ion chemistry of groundwater in Delhi area: chemical weathering processes and groundwater flow regime. J. Geol. Soc. India., 47, 179-188.

Dissanayake, C.B., Niwas, J.M. and Weerasooriya, S.V.R., 1987. Heavy metal pollution of the mid canal of Kandis; An environmental case study from Sri Lanka. Environ. Res., 42, 24–35.

Doneen, LD., 1962. The influence of crop and soil on percolating water. In: Proceedings of 1961. Biennial conference on Groundwater Recharge., 156–163.

Doneen, LD., 1964. Water quality for agriculture. Department of Irrigation, University of California, Davis. P. 48.

Eaton, FM., 1950. Significance of carbonates in irrigated waters. Soil Sci. 69, 127–128.

Elango, L., Kannan, R. and Senthil Kumar, M., 2003. Major ion chemistry and identification of hydrogeochemical processes of groundwater in a part of Kancheepuram district, Tamil Nadu, India. J. Environ. Geosci., 10, 157–166.

Elango, L., Brindha, K., Kalpana, L., Faby Sunny Nair, R. N. and Murugan, R., 2012. Groundwater flow and radionuclide decay-chain transport modeling around a proposed uranium tailings pond in India. Hydrogeology J., 20, 797–812. DOI 10.1007/s10040-012-0834-6.

Fan, A.M., 2011. Nitrate and Nitrite in drinking water: a toxicological review. California Environmental protection Agency, Oakland.

Faten, H., Azouzi, R., Charef, A. and Be´dir, M., 2016. Assessment of groundwater quality for irrigation and drinking purposes and identification of hydrogeochemical mechanisms evolution in ortheastern, Tunisia. Environ. Earth Sci., 75, 746. https ://doi.org/10.1007/s12665-016-5441-8.

Gibbs, R.J., 1970. Mechanisms controlling world water chemistry Science. 170, 1081–1090.

Guo, F., Jiang, G. and Yuan, D., 2007. Major ions in typical subterranean rivers and their anthropogenic impacts in southwest karst areas, China. Environ. Geol., 53, 533–541

Hem, J.D., 1985. Study and interpretation of the chemical characteristics of natural water, 2nd edn. US Geol Surv water supply. 2, 254-363.

Jain, C.K., Bandyopadhyay, A. and Bhadra, A., 2010. Assessment of ground water quality for drinking purpose, District Nainital, Uttarakhand, India. Environ. Monit. Assess., 166(1–4), 663–676.

Kinzelbach, W., Bauer, P., Siegfried, T. and Brunner, P., 2003. Sustainable groundwater management—problems and scientific tools. 26(4), 279–284.

Karanth, K.R., 1987. Groundwater Assessment, Development and Management. Tata McGraw-Hill Publishing Company Limited, New Delhi. pp. 576-638.

Karanth, KR., 1989. Groundwater assessment, development and management Tata McGraw-Hill Publ. Com. Ltd, New Delhi.

Kelly,W.P., 1940. Permissible composition and concentration of irrigated waters. Proc AFCS. 66:607.

Kumar, R., Singh, RD. and Sharma, KD., 2005. Water resources of India. Curr. Sci., 89(5), 794–811.

Loizidou, M. and Kapetanios, EG., 1993. Effect of leachate from landfills on underground water quality. Sci. Total Environ., 128, 69–81

Muralidhara Reddy, B. and Sunitha, V., 2020. Geochemical and health risk assessment of fluoride and nitrate toxicity in semi- arid region of Anantapur District, South India. Environmental Chem.Ecotoxicology, 2, 150-161. http://dx.doi.org/10.1016/j.encero.2020.09.002.

Muralidhara Reddy, B., Sunitha, V., Prasad, M., Sudharshan Reddy, Y. and Ramakrishna Reddy, M., 2019. Evaluation of groundwater suitability for domestic and agricultural utility in semi-arid region of Anantapur, Andhra Pradesh State, South India. Groundwater for Sustainable Development., https://doi.org/10.1016/j.gsd.2019.100262.

Narsimha, A. and Sudarshan, V., 2013. Hydrogeochemistry of groundwater in Basara area, Adilabad district, Andhra Pradesh, India. J. Appl. Geochem., 15(2), 224-237.

Pawar, NJ. and Shaikh. IJ., 1995. Nitrate pollution of ground waters from shallow basaltic aquifers, Deccan trap Hydrologic Province, India. Environ. Geol., 25, 197–204.

Piper, A., 1953. A graphic procedure in the geochemical interpretation of water analysis. USGS Groundwater Note. No. 12.

Raghunath, H.M., 1987. Groundwater, 2nd edn. New Delhi, Wiley Eastern Limited. P. 563.

Rajmohan, N. and Elango, L., 2004. Identification and evolution of hydrogeochemical processes in the groundwater environment in an area of the Palar and Cheyyar River Basins, Southern India. Environ. Geol., 46,47–61.

Ramesh, R. and Anbu, M., 1996. Chemical methods of Environmental Analysis, Macmillan India Limited.

Ravichandra, R. and Chandana, O.S., 2006. Study on evaluation on ground water pollution in Bakkannaplem, Visakhapatnam. Nature, Environment and Pollution Technology. 5(2), 203-207.

Richards, L.A., 1954. Diagnosis and improvement of saline and alkali soils. US Department of Agricultural Handbook, Washington DC. P. 160.

Sanchez Martos, F., Pulido Bosch, A. and Calaforra, J.M., 1999. Hydrogeochemical processes in an arid region of Europe (Almeria, SE Spain). Appl. Geochem., 14, 735–745

Sarath Prashanth, S.V., Magesh, N.S., Jitheshlal, K.V., Chandrasekhar, N. and Ganhadhar, K., 2012. Evaution ofgroundwater quality and its suitability for drinking and agricultural use in the costal stretch of Alappizha District, Kerala, India.Appl. water sci., 2, 165-175.

Shand, S.J., 1952. Rocks for chemistry. Patmann Publishing Company, New York. p. 14.

Sreedevi, P.D., Shakeel, Ahmed. and D.V, Reddy., 2017. Mechanism of fluoride and nitrate enrichment in hard rock aquifers in Gooty Mandal, South India. Environmental processes, 4(3), 625-644.

Sreedevi, P.D., Sreekanth, P.D., Shakeel, Ahmed. and D.V, Reddy., 2018. Appraisal of groundwater quality in crystalline aquifer; a chemometric approach. Arabian J. Geosci., 11(9), 211.

Sreedevi, P.D., Sreekanth, P.D., Shakeel, Ahmed. and D.V, Reddy., 2019. Evaluation of groundwater quality for irrigation in a semi-arid region of South India. Sustainable Water Res. Management., 5(3) 1043-1056.

Subba Rao, N., Prakasa Rao, J., John Devadas, D., Srinivasa Rao, KV., Krishna, C. and Nagamalleswara Rao, B., 2002. Hydrogeochemistry and groundwater quality in a developing urban environment of a semi-arid region, Guntur, Andhra Pradesh. J. Geol. Soc. India., 59, 159–166.

Subba Rao, N., 2017. Controlling factors of fluoride in groundwater in a part of South India. Arab. J. Geosci., 10(23), 524. https://doi.org/10.1007/s12517-017-3291-7

Sudarshan Reddy, Y., Sunitha, V, Suvarna, B. and Prasad, M., 2018. Assessment of Groundwater quality with special reference to Fluoride in groundwater surrounding abandoned mine sites at Vemula, Y.S.R district, A.P.J. Emerging Technologies and Innovative Res., 5(11), 769-777.

Sudharshan Reddy, Y., Sunitha, V. and Suvarna, B., 2020. Monitoring of groundwater quality for drinking purposes using the WQI method and its health implications around inactive mines in Vemula Vempalli region, Kadapa District, South India. App. Water Sci., 10:202. https://doi.org/10.1007/s13201-020-01284-2.

Sunitha, V. and Srinivasulu, G., 2015. Fluoride contamination of groundwater and its impacts on human health in and around vemula, vempalli mandals, Y.S.R district, A.P. India. Int. J. Curr. Res., 3(7).

Sunitha, V. and Muralidhara Reddy, B., 2018. Defluoridation of water using Mentha longifolia (Mint) as Bioadsorbent. J. Ind. Geophys. Un., 22(2), 207-211.

Sunitha, V. and Reddy, Y.S., 2019. Hydrogeochemical evaluation of groundwater in and around Lakkireddipalli and Ramapuram, YSR District, Andhra Pradesh, India. Hydro. Res., 2, 85-96. https://doi.org/10.1016/j.dib.2020.105187.

Sunitha, V. and Reddy, B.M., 2022. Geochemical characterization, deciphering groundwater quality using pollution index of groundwater (PIG), water quality index (WQI) and geographical information system (GIS) in hard rock aquifer, South India. Appl Water Sci., 12, 41. https://doi.org/10.1007/s13201-021-01527-w.

Sunitha, V., Rajeswara, Reddy, B. And Ramakrishna, M., 2012. Groundwater quality evaluation with special reference to fluoride and nitrate pollution in Uravakonda, Anantapur District, Andhra Pradesh, India. Int. J. Res. Chem. Environ. 2 (1), 88–96.

Sunitha, V., Abdullah Khan, J. and Muralidhara Reddy, B., 2013. Fluoride contamination in groundwater in and around Badvel, Kadapa district, Andhrapradesh, Indian. J. Advances in Chem. Sci., 2(1), 78-82.

Sunitha, V., Abdullah Khan, J., Muralidhara Reddy, B., Prasad, M. and Ramakrishna Reddy, M., 2014.Assessment of Groundwater Quality in Parts of Kadapa and Anantapur Districts, Andhra Pradesh, India. Indian J. Advances in Chem. Sci., 3, 96-101.

Sunitha, V., Abdullah Khan, J., Prasad, M. and Ramakrishna Reddy, M., 2016. Seasonal variation of groundwater quality in parts of Kadapa and Anantapur Districts Andhra Pradesh, India. Int. J. Engineering Res. and Applications, 6(5), 05-08.

Sunitha, V., Sudharshan Reddy, Y., Suvarna, B. and Muralidhara Reddy, B., 2022. Human health risk assessment (HHRA) of fluoride and nitrate using pollution index of groundwater (PIG) in and around hard rock terrain of Cuddapah, A.P. South India. Environmental Chemistry and Ecotoxicology., 4, 113-123. https://doi.org/10.1016/j.enceco.2021.12.002.

Soltan, M.E., 1999. Evaluation of groundwater quality in Dakhla Oasis (Egyptian Western Desert). Eviron. Monit. Assess., 57, 157–168

Sawyer, C.N., 1994. Chemistry. McGraw Hill, New York, 103-104.

Sawyer, C.N., McCarthy, PL., Parkin, GF., 2003. Chemistry for environmental engineering and science. McGraw-Hill, New York. 5 –752.

Szaboles, I. and Darab, C., 1964. The influence of irrigation water of high sodium carbonate content of soils. In Proceedings of 8th international congress of ISSS, Trans, II. 803-812.

Thomas, K.B., Opoku, F., Acquaah, S.O. and Akoto, O., 2016. Groundwater quality assessment using statistical approach and water quality index in Ejisu-Juaben Municipality, Ghana. Environ. Earth. Sci., 75, 489. https ://doi.org/10.1007/s1266 5-015-5105-0.

Todd, D.K., 1980. Groundwater hydrology, 2nd Ed, New York, Wiley. 1-535.

US Geological Survey., 2000 . Classification of natural ponds and lakes. US Department of the Interior, US Geological Survey, Washington, DC.

WHO., 2011. Guidelines for Drinking Water Quality, fourth ed., WHO press. p. 564.

WHO., 1990. Environmental health criteria 81: vanadium [R]. World Health Organization, Geneva. 1–35.

Wilcox, L.V., 1955. Classification and use of irrigation water. Washington DC: US Dept. of Agriculture. Cir. No.969:19.

Received on: 28.02.2022; Revised on: 24.04.2022; Accepted on: 05.05.2022

J. Ind. Geophys. Union, 26(3) (2022), 239-244

An overview of micropalaeontological (pollen and diatom) research in endangered wetlands of Assam: Prospect for future study

Amulya Saxena[1*], Abhijit Mazumder[1], Dhruv Sen Singh[2] and Samir Kumar Bera[1]
[1] Birbal Sahni Institute of Palaeo sciences, 53 University Road, Lucknow – 226007(U.P.), India
[2] Geology Department, Lucknow University, Lucknow – 226007(U.P.), India
*Corresponding Author: amulya.saxena@bsip.res.in; amulya.bsip@gmail.com

ABSTRACT

This paper deals with the micropalaeontological (pollen and diatom) records available from Assam wetlands located in the northeastern part of India. Pollen studies reveal the changing climatic conditions (from wet to dry and vice versa) within Holocene on the basis of changing vegetational patterns of the region. On the other hand, the studies on diatom are mostly the reporting of the different recent diatom species from wetlands. Very few multiproxy researches have been done on both pollen and diatom to decipher the palaeoclimatic changes, except two studies from separate regions. Furthermore, this paper also deals with the preliminary systematic research of the surface samples collected from three different environmental set-ups of forest to establish the correlation between these environmental set-ups and its biological components. The non-arboreal pollen taxa are predominating in forest area, which is almost devoid of diatom; while open land area is characterized by arboreal pollen taxa as well as high abundance of diatom, mainly oligotrophic and pollution indicator diatom species. This study is hence used to reconstruct the shifts of environmental set-ups (due to palaeoclimatic changes) in the past after analysing the core samples collected from the same regions. This review will be a pathfinder for future researchers to study both the proxies for vegetational and climatic variations during Holocene in and around Assam wetlands.

Keywords: Pollen and diatom, Palynology, Palaeoenvironment and palaeoclimate, Assam wetlands

INTRODUCTION

The Assam wetlands located in northeast India is part of the Indo-Burma biodiversity hotspot, expanding over a vast area of southern China, Andaman and Nicobar Islands, Myanmar, Thailand till Malaysian peninsula (Myers et al., 2000; Mittermeier et al., 2004). This Eastern Himalaya hotspot is the second largest one with a total area of 23,08,815 km^2 (Myers, 1988), which include 50% of floristic population of India among which 8000 species of flowering flora along with some primitive angiosperms are recorded (Takhtajan, 1969). This hotspot sustains vast population of natural habitats due to its highly diversified geomorphology and climatic variations. This enriched biodiversity was developed as a result of its geological and evolutionary history. Due to sea-level fluctuation and alternating connection and separation of biotic assemblage from its ecosystems, the diversified speciation has occurred through a long geological time (van Dijk et al., 2004).

Wetlands constituting a fundamental part of both the terrestrial and aquatic system, are one of the most important ecosystems on the Earth surface covering almost 6% of the Earth's surface area. In India, wetlands occupy an average of 1-5% of the total area of the country (Space Applications Centre, 2011). Assam experiencing the intense drainage networks of the Brahmaputra and Barak rivers and adjoining riverine land, is the favourable place to develop wetlands. In Assam, as many as 3513 wetlands are reported with a total area of 1012 km^2, constituting 1.29% of total area of the state (Chatterjee et al., 2006). Beels, swamps and marshes were formed due to overflow of flood water in lowlands, as well as due to the presence of meandering streams with several migrating channels.

Wetlands have a vital ecological role to maintain the balance between different components of nature, to control the flood and hence the soil erosion, to sustain surface water and ground water conditions, to regulate hydrological cycle and to maintain the biological balance between flora and fauna (Kundu, 1997). Certain species of algae present in wetlands reduce the water pollution and hence improve the water quality. Due to multidimensional significance, wetlands draw attention for studying their ecological and environmental changes.

So far many significant palaeoenvironmental and palaeoclimatic researches have been carried out from the endangered wetlands of Assam mainly based on palynology (Dixit and Bera, 2011; Bera et al., 2011a,b; Basumatary et al., 2015; Basumatary et al., 2018 and few others), but very little work has been carried out based on both diatom and palynological studies inferring the palaeoclimatic reconstruction as well as assessing the degradation of the wetlands except Bera et al. (2008) and Tripathi et al. (2021). The objectives of the paper are to review the existing micropaleontological works and to indicate the scope of future research.

PREVIOUS STUDIES

Studies on pollen

Assam wetlands attracted researchers for an enriched storehouse of spore and pollen. But no coordinated research has been done to study the evolution of the palaeovagetation and palaeoclimate of these wetlands, except a few palaeoclimatic studies based on palynology from different wetlands (Figure 1; Table 1).

Table 1. Research work carried out in the study area in wetlands of Assam. Number on the map as given in this table, refer to Figure 1.

Author	Year	Area	No. on Map
Bera et al.	2008	Chatla Lake of Barak valley	6
Dixit and Bera	2011	Deosila swamp, Rangjuli reserve Forest	2
Bera and Dixit	2011	Merbeel Swamp, Dibrugarh	16
Bera et al.	2011a	DhirBeel, Dhubri District	1
Bera et al.	2011b	Mothabeel and Dangrithan reserve forest	15
Dixit and Bera	2012	Dabaka Swamp, Nagaon District	11
Phukan and Bora	2012	Different ponds, lakes, rivers of Sivasagar district	14
Dixit and Bera	2013a	Chayagaon swamp, Kamrup District	5
Dixit and Bera	2013b	Bhogdoi swamp, Kamrup District	4
Gurung et al.	2013	DeeporBeel, Kamrup District	7
Borgohain and Tanti	2014	Four places in Nagaon district	10
Basumatary et al.	2015	Subankhata swamp	3
Nahar and Tanti	2017	DeeporBeel, Kamrup District	8
Basumatary et al.	2018	Majuli River Island	13
Deb et al.	2019	DeeporBeel, Kamrup District	9
Tripathi et al.	2021	Chatla Lake, Barak valley	12

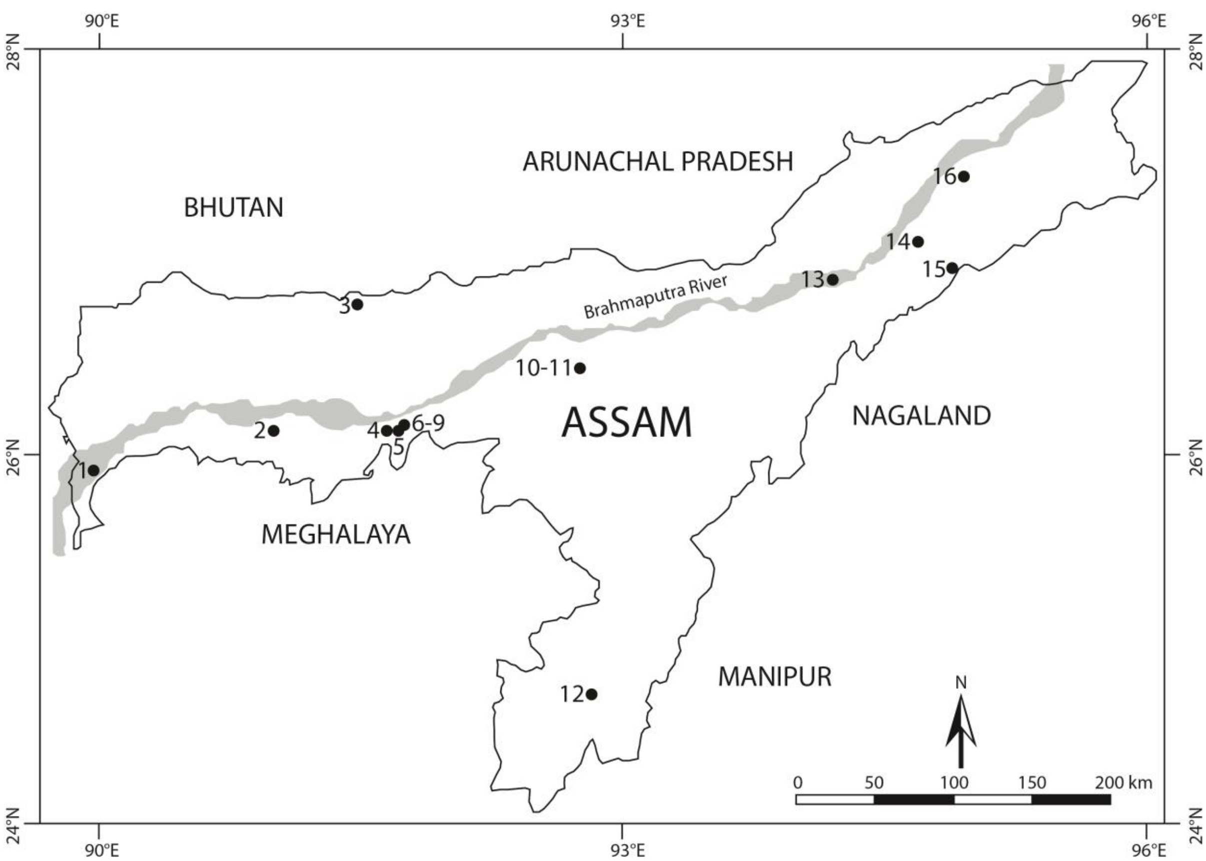

Figure 1. Locations of study areas as mentioned in Table 1

The palynology of 2.5 m long sedimentary profile collected from Deosila swamp of Rangjuli reserve forest deciphers the palaeovegetation and hence palaeoclimatic variation for last 6.3 kyr (Dixit and Bera, 2011). This study reveals that tropical trees savannah vegetation from 6.3 to 2.9 kyr BP exhibits relative less cool and dry climatic condition; while from 2.9 to 1.5 kyr BP, the presence of tropical mixed deciduous forest infers the warm and humid climate. After this period till 0.5 kyr BP, influence of active SW monsoon with the increased warm and humid climatic condition prevailed as the presence of tropical deciduous forest increased, and lastly, the climatic condition changed into warm and relatively dry with weak monsoon as forest flouristics reduced substantially.

In another study, a 1.2 m long sediment core collected from Merbeel Swamp, Dibrugarh reveals the vegetational transition from tropical mixed deciduous to semi evergreen forest under the influence of three climatic phases, namely relatively cool and dry, advent of warm and finally enhancement of warm and humid climatic condition during last 3 kyr (Bera and Dixit, 2011). Palynology in and around Dhir Beel, Dhubri District was studied to understand the relation between pollen and vegetation, and hence to infer the effect of biological degradation (including the human impact) in wetland (Bera et al., 2011a). Based on the presence of pollen from the Mothabeel and Dangrithan reserve forest, a detailed palaeovegetational succession has been prepared for last 1.76 kyr (Bera et al., 2011b), which revealed that the semi-arid and warm humid climate predominated in the region, followed by episodes of occasional flood.

Another 3.2 m long sedimentary profile from Dabaka Swamp, Nagaon District from the Lower Brahmaputra flood plain was studied for its palynological assemblages during last 14.1 kyr BP (Dixit and Bera, 2012). From 14.1 to 12.7 kyr BP, a persistent fluvial activity was recorded, while it got changed into tropical tree savannah vegetation with cooler and drier climate till 11.6 kyr BP, which corresponds to Younger Dryas; from 11.6 to 8.3 kyr BP, the presence of tropical mixed deciduous taxa reveals the relatively less cool and dry climatic condition. After this phase again, fluvial episodes regained till 7.1 kyr BP and later between 7.1 and 1.5 kyr BP, the climatic condition became warm and humid with tropical mixed deciduous vegetation which corresponds to Holocene climate optimum. In comparison, during 1.5 to 0.7 kyr BP, the enhancement of warm and humid climatic condition with tropical mixed deciduous vegetation is seen which eventually deteriorated due to human encroachment under warm and relatively dry climate from 0.7 kyr BP onwards.

Similarly, a 3.4 m long sedimentary core from Chayagaon swamp, Kamrup District has been studied to decipher the climatic and vegetational history during Late Quaternary (Dixit and Bera, 2013a). This study reveals persistent fluvial activity from 14.8 to 12.4 kyr BP which was succeeded by cool and dry climatic condition with lesser precipitation, corresponding to the Younger Dryas, which might cause the development of tropical savannah vegetation; thereafter climate changed into less cool and dry condition with the presence of tropical mixed deciduous vegetation till 7.6 kyr BP. Between 7.6 and 6.7 kyr BP, the fluvial activity increased, which was succeeded by warm and moderately humid climatic condition with enhancement of precipitation along with the tropical mixed deciduous vegetation till 1.9 kyr BP, which is well matched with Holocene climate optimum. Between 1.9 and 0.9 kyr BP, due to increase in warm and humid climate the tropical mixed deciduous vegetation proliferated, which corresponds to Medieval Warm Period; afterwards the tropical mixed deciduous vegetation got deteriorated under warm and dry climate as well as an extensive encroachment of human settlement. Another study of 1.8 m long sedimentary core from Bhogdoi swamp, Kamrup District revealed the palaeovegetational and palaeoclimatic changes during last 3.8 kyr (Dixit and Bera, 2013b). In this study, the presence of mixed deciduous forest indicates the warm and humid climate during first phase of climatic condition (from 3.8 to 2.5 kyr BP); in second climatic phase (from 2.5 to 0.6 kyr BP), the proliferation of mixed deciduous vegetation deciphers the increase of the warm and humid climatic condition with increased precipitation. In the last phase (from 0.6 kyr BP to Recent), the gradual deterioration of mixed deciduous vegetation indicates the warm and relatively drier climatic condition. An extensive study of palynoassemblage has been done from the trench sediment samples collected from Subankhata swamp of Assam to reconstruct palaeovegetational, palaeoclimatological and palaeomonsoonal variations during last 27.2 kyr (Basumatary et al., 2015). In this study, entire core was divided into five palynozones. Oldest zone, corresponding 27.2 kyr BP age, represents the open-land savannah forest vegetation due to cool and dry climatic condition with less rainfall. Next zone, corresponding to Last Glacial maximum, exhibits a transitional climatic condition with increased rainfall which produced moist forest vegetation. Succeeding zone signifies the establishment of deciduous and evergreen forest in presence of warm and humid climate with stronger monsoon, high wind activity and strong water transport. Next zone is also characterized by same type of climatic condition with strengthening of monsoon, which shows regional forest with the initiation of human activities. Topmost zone, corresponding to Holocene climate maximum, represents comparatively warm and less humid climate with the deterioration of climate and primary mixed deciduous forest vegetation along with increased human activities. Unique attempt was made to apply palynological data to decipher palaeo-flood of two wetlands from the Majuli River Island, which provides the baseline data for reconstructing palaeovegetational and palaeoclimatic variations (Basumatary et al., 2018).

Studies on diatom

Compared to pollen study from Assam wetlands, diatoms have not been studied extensively, particularly in the application of palaeoclimatic study. Few studies have been done based on surface samples to report the diatom species present in respective wetlands. Sixteen new reported species of diatom belonging to nine genus was recorded from different ponds, lakes, rivers of Sivasagar District (Phukan and Bora, 2012). In another study, 65 species (53 pinnate and 12 centric) diatom belonging to 26 genera was reported from water and soil samples from six different sites in Deepor Beel, Kamrup District (Gurung et al., 2013). In another study, the silica rich soils from aquatic to semi-aquatic habitats from four places in Nagaon District, Assam has been analysed and 103 species of 20 genera of freshwater diatoms were found, which are exclusively solitary pinnate forms (Borgohain and Tanti, 2014). Photoluminescence study of four freshwater diatoms has been carried out on the water and soil samples collected from Deepor Beel to reveal the non-uniform pore size of nanostructures in the diatom frustules (Nahar and Tanti, 2017). While investigating the algal composition, diversity and distribution in the water of Deepor Beel wetland, 27 algal species (among which 14 species are of diatom) are reported to assess the effect of pollution over the physico-chemical as well as biological properties (Deb et al., 2019).

Studies on both pollen and diatom

Though there are very few works done on multiproxy aspects (both pollen and diatom), some very unique works have been done on their palaeoclimatic implications. A preliminary attempt has been made based on multiproxy study (pollen-spores and diatom) to indicate the biological degradation in Deepor Beel, using degraded palynomorphs and fungal remains (Bera et al., 2008). A multiproxy (pollen and diatom) approach has been made from a 0.8 m long sedimentary core from Chatla Lake of Barak valley to decipher palaeovegetational and palaeoclimatic variations between 1.3 and 0.7 kyr BP (Tripathi et al., 2021). Pre-Medieval Warm Period (MWP) exhibits warm and less humid climate due to weak monsoon and during the beginning of MWP, the climatic conditions changed to warm and humid. At the peak of MWP, warm and humid climate increased and lastly, during post-MWP, less warm a humid climate continued along with some anthropogenic activities (Tripathi et al., 2021).

PRESENT INVESTIGATION

To understand the relation between the palaeoenvironmental /palaeoclimatic changes and their response on biotic components, the surface and thereafter subsurface samples from Assam wetlands have been studied methodically. The data were generated from two study locations, namely Nalapur and Sukurbaria, in Rani-Garbhanga reserve forest, Assam (Figure 2). A total of 12 modern surface sediment samples (6 from each location) were collected. In each location, three different environmental set-ups were identified, namely forest area, marginal area and open land. Around 300 diatom valves and pollen grains were separately counted from each sample. It has been observed that the number of diatom is less in forest area, while it increases highly in open land area. The open land area shows high abundance of oligotrophic diatom species, such as *Frustulia indica*, *Pinnularia amabilis*, *P. divergence* and *P. virdis* as well as the pollution indicator *Nitzschia umbonata*. On the other hand, non-arboreal (Poaceae and Asteroideae) taxa are predominant in forest area and it has been decreasing towards open area; in open area, arboreal taxa (*Largerstroemia* and *Terminalia*) is present in high abundance. The data obtained from pollen and diatom are used to establish the pattern of vegetation and nature of depositional environment of different environmental set-ups. Applying this dataset, the core samples collected from nearby regions were analysed to demarcate the shift of vegetational patterns and environmental changes (from hot/humid to cold/dry and vice versa) during Holocene. These data will be very helpful to reconstruct the palaeoclimatic scenario in and around this area during Holocene.

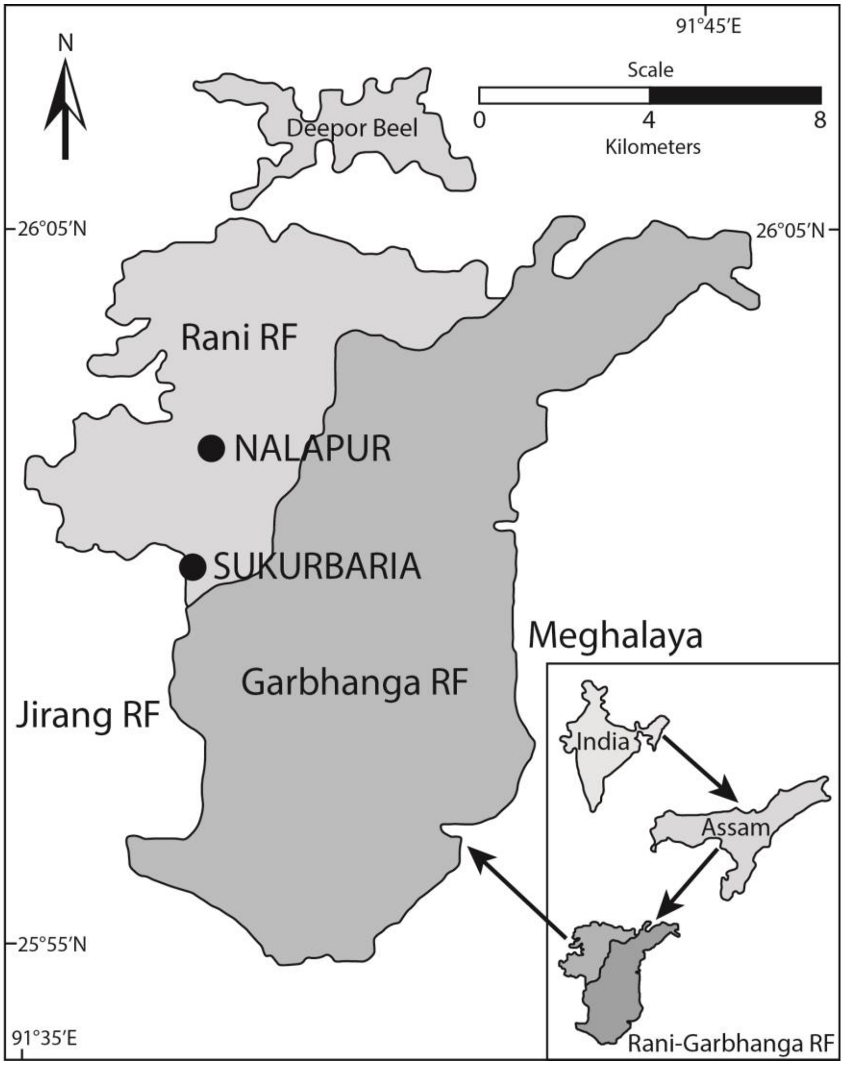

Figure 2. Location of present study area

DISCUSSION AND CONCLUSIONS

The studies of endangered wetlands, based on pollen and diatom indicate that some important palaeovegetational (hence palaeoclimatic) works has been done based on palynology from different parts of Assam to give an overview of the palaeoclimatic changes over the Holocene based on detailed study on pollen. On the other hand, ecological study of diatoms has not been extensively used to study the palaeoclimate. But there were merely two research works carried out on the basis of the scientific coordination between the study of pollen and diatom from the same region. Hence, serious attempts should be made to correlate the data obtained from pollen with accordance to the data of diatom to portray the evolutionary changes of the Assam wetlands with special reference to palaeovegetation and palaeoclimate. In view of this prospect, few surface sediment samples collected from three different environmental set-ups (forest area, marginal area and open land area) from two physically separated locations, namely Nalapur and Sukurbaria, from Rani-Garbhanga reserve forest, have been studied. The study of diatom and pollen from these samples reveals that the sediment collected from forest area contains more non-arboreal pollen taxa, while open land area contains more arboreal pollen taxa. On the other hand, open land area shows the proliferation in diatom number with the oligotrophic and pollution indicator species. This investigation is a unique approach to establish the basic dataset for the study to understand the palaeoenvironmental and palaeoclimatic changes (from wet to dry and vice versa) during Holocene while analysing the core samples from same regions. Therefore, this kind of multiproxy research based on both pollen and diatom needs to address the climatic data gaps from the endangered wetlands of Assam.

ACKNOWLEDGEMENTS

The authors wish to thank the Director, Birbal Sahni Institute of Palaeosciences, Lucknow for granting the laboratory and library facilities as well as giving permission to publish the paper. This paper is submitted under BSIP Publication no. 64/2021-22. The authors are also grateful to anonymous reviewer to provide valuable comments to improve this paper. The authors also thank to SERB-DST for sponsoring the Project File no. SERB/2014/0233.

Compliance with Ethical Standards

The authors declare no conflict of interest and adhere to copyright norms.

REFERENCES

Basumatary, S.K., Tripathi, S., Bera, S.K., Nautiyal, C.M., Devi, N. and Sarma, G.C., 2015. Late Pleistocenepaleoclimate based on vegetation of the Eastern Himalayan foothills in the Indo-Burma Range, India. Palynol., 39(2), 220-233.

Basumatary, S.K., Nautiyal, C.M., Ghosh, R. and Tripathi, S., 2018. Modern pollen deposition in wetlands of Majuli Island and its implication to decipher paleoflood episodes in northeast India. Grana, 57(4), 273-283.

Bera, S.K. and Dixit, S., 2011. Pollen Analysis of Late Holocene Lacustrine Sediment from Jeypore Reserve Forest, Dibrugarh, Assam. Geological Processes and Climate Change (D.S. Singh and N.L. Chhabra, Ed.). Macmillan Publishers India Ltd.

Bera, S.K., Dixit, S., Basumatary, S.K. and Gogoi, R., 2008. Evidence of biological degradation in sediments of Deepor BeelRamsar Site, Assam as inferred by degraded palynomorphs and fungal remains. Curr. Sci., 95(2), 178-180.

Bera, S.K., Basumatary, S.K. and Brahma, M., 2011a. Interplay between pollen and vegetationin and around DhirBeel, Dhubri District, Assam: A future potential Ramsar site. J. Ind. Bot. Soc., 90 (1&2), 159-164.

Bera, S.K., Basumatary, S.K. and Gogai, B., 2011b. Pollen analysis its implications inclimate change and vegetation succession in recent past: evidence from surfaceand subsurface fluvial sediment of tropical forests of eastern Assam, NortheastIndia. J. Frontline Res., 1, 62e74.

Borgohain, D. and Tanti, B., 2014. Diversity of freshwater diatoms from few silica rich habitats of Assam, India. J. Res. Biol., 4(1), 1162-1173.

Chatterjee, S., Saikia, A., Dutta, P., Ghosh, D. and Worah, S., 2006. Review of Biodiversity in Northeast India. Technical Report, WWF-India, Delhi.

Deb, S., Saikia, J. and Kalamdhad, A.S., 2019. Ecology of Deeporbeel wetland, a ramsar site of Guwahati, Assam with special reference to algal community. European J. Biomed. Pharma. Sci., 6(5), 232-243.

Dixit, S. and Bera, S.K., 2011. Mid-Holocene vegetation and climatic variability intropical deciduous Sal (Shorearobusta) forest of lower Brahmaputra Valley,Assam. J. Geol. Soc. Ind., 77, 419-432.

Dixit, S. and Bera, S.K., 2012. Holocene climatic fluctuations from Lower Brahmaputraflood plain of Assam, northeast India. J. Earth Syst. Sci., 121(1), 135-147.

Dixit, S. and Bera, S.K., 2013a. Pollen-inferred vegetation vis-á-vis climate dynamicssince Late Quaternary from western Assam, Northeast India: signal of globalclimatic events. Quat. Int., 286, 56-68.

Dixit, S. and Bera, S.K., 2013b. Vegetation vis a vis climate change around Bhogdoi swamp in lower Brahmaputra flood plain of Assam, Northeast India since Late Holocene. Palaeobot., 62, 19–27.

Gurung, L., Buragohain, A.K., Borah, S.P. and Tanti, B., 2013. Freshwater diatom diversity in DeeporBeel - A Ramsar site. J. Res. Plant Sci., 2(2), 182-191.

Kundu, N., 1997. Managing Wetlands, Institution of Wetland Management and Ecological Design, Calcutta.

Mittermeier, R.A., Gils, P.R., Hoffman, M., Pilgrim, J., Brooks, T., Mittermeier, C.G., Lamoreaux, J. and Da Fonseca, G.A.B., 2004. Hotspots revisited: Earth’s biologically richest and most endangered terrestrial eco-regions. Mexico City: CEMEX/Agrupación Sierra Madre.

Myers, N., 1988. Threatened Biotas: hot spots in tropical forests. Environmental., 8, 1-20.

Myers, N., Mittermeier, R.A., Mittermeier, C.G., Fonseca, G.A.B. and Kent, J., 2000. Biodiversity hotspots for conservation priorities. Nat., 403, 853–858.

Nahar. S. and Tanti. B., 2017. Freshwater Diatoms from DeeporBeel - A Ramsar Site of Assam, India Revealed Potential Photoluminescence Properties for Nanotechnological Applications. J. Mat. Sci., 5(4), 17-22.

Phukan, S. and Bora, S.P., 2012. Preliminary report of diatomsfromShivasagar District of Assam. Ind. J. Fundamental Appl. Life Sci., 2(2), 55-61.

Space Applications Centre, 2011. National Wetland Atlas. SAC, Indian Space Research Organisation, Ahmedabad.

Takhtajan, A., 1969. Flowering Plants: Origin and Dispersal. Oliver and Boyd.

Tripathi, S., Basumatary, S.K., Pandey, A., Khan, S., Tiwari, P. and Thakur, B., 2021. Palaeoecological changes from 580 to 1220 CE from the Indo-Burma region: A biotic assessment from the Barak Valley of Assam, northeast India. Catena, 206, 105487.

van Dijk, P.P., Tordoff, A.W., Fellowes, J., Lau, M. and Ma J.S., 2004. Indo-Burma (R.A. Mittermeier, P. Robles-Gil, M. Hoffmann, J. Pilgrim, T. Brooks, C.G. Mittermeier, J. Lamoreaux and G.A.B. da Fonseca, Eds.). Hotspots Revisited: Earth’s Biologically Richest and Most Endangered Terrestrial Ecoregions. CEMEX, Monterrey; Conservation International, Washington D.C. and Agrupación Sierra Madre, Mexico.

Received on: 08.12.2021; Revised on: 06.05.2022; Accepted on: 18.05.2022

GUIDE FOR AUTHORS

The Journal of Indian Geophysical Union (J-IGU), published bimonthly by the Indian Geophysical Union (IGU), is an interdisciplinary journal from India that publishes high-quality research in earth sciences with special emphasis on the topics pertaining to the Indian subcontinent and the surrounding Indian Ocean region. The journal covers several scientific disciplines related to the Earth sciences such as solid Earth geophysics, geology and geochemistry, apart from marine, atmosphere, space and planetary sciences. J-IGU welcomes contributions under the following categories:

- Research papers and short notes reporting new findings.
- Review articles providing comprehensive overview of a significant research field.

In addition, J-IGU also welcomes short communications, after communications and report on scientific activity, book reviews, news and views, etc.

The manuscript should be submitted electronically as a single word format (.doc file) including the main text, figures, tables, and any other supplementary information along with the signed "Declaration Letter". The manuscript should be submitted by email (jigu1963@gmail.com) to the Chief Editor.

After acceptance of the manuscript the corresponding author would be required to submit all source files (text and Tables in word format) and figures in high resolution standard (*.jpg, *.tiff, *.bmp) format. These files may be submitted to J-IGU as a single *.zip file along with the "Copyright Transfer Statement".

IMPORTANT INFORMATION

Ethics in publishing
J-IGU is committed to ensuring ethics in publication and takes a serious view of plagiarism including self-plagiarism in manuscripts submitted to the journal. Authors are advised to ensure ethical values by submitting only their original work and due acknowledgement to the work of others used in the manuscript. Authors must also refrain from submitting the same manuscript to more than one journal concurrently, or publish the same piece of research work in more than one journal, which is unethical and unacceptable. Editor of J-IGU is committed to make every reasonable effort to investigate any allegations of plagiarism brought to his attention, as well as instances that come up during the peer review process and has full authority to retract any plagiarized publication from the journal and take appropriate action against such authors if it is proven that such a misconduct was intentional.

Similarly, Editor and Reviewers are also expected to follow ethical norms of publishing by ensuring that they don't use any unpublished information, communicated to them for editorial or review purpose, in their own research without the explicit written consent of the author. They are also expected to keep manuscript/ data/ observations/ any other information related to the peer review confidential to protect the interest of the authors. Reviewers should refrain from reviewing the manuscripts in which they have conflicts of interest resulting from competitive, collaborative, or other relationships or connections with any of the authors, companies, or institutions connected to the manuscript.

Conflict of interest
All authors are requested to disclose any actual or potential conflict of interest including any financial, personal or other relationships with other people or organizations within three years of beginning the submitted work that could inappropriately influence, or be perceived to influence, their work.

Submission declaration
Submission of a manuscript implies that the work has not been published previously and it is not under consideration for publication elsewhere, and that if accepted it will not be published elsewhere in the same or any other form, in English or in any other language, without the written consent of the publisher. It also implies that the authors have taken necessary approval from the competent authority of the institute/organization where the work was carried out.

Copyright
After acceptance of the manuscript the corresponding author would be required to sign and submit the "Copyright Transfer Statement".

MANUSCRIPT PREPARATION

The corresponding author should be identified (include E-mail address, Phone/Mobile number). Full affiliation and postal address must be given for all co-authors.

Abstract:
An abstract of not more than 300 words must be included.

Text:
The manuscript should be structured to include a front page containing the title, Author(s) name, affiliation and address of the institute, where the work was carried out, a short title, and 5-to-6 Key words. Author(s) present address, if different from the above mentioned address, may be given in the footnote. The corresponding author should be identified with an asterisk and his/her email ID should be provided. This page should be followed by the main text consisting of Abstract, Introduction, Methods/ Techniques/ Area description, Results, Discussion, Conclusions, Acknowledgements, and References. Tables and Figures with captions should be inserted at the end of main text. It should not be inserted in the body of the text.

Figures/ Illustrations:
All figures should be provided in camera-ready form, suitable for reproduction (which may include reduction) without retouching. Figures in high-resolution (at least 300 dpi) standard formats (*.jpg, *.tiff, *.bmp) are acceptable. Figures should be numbered according to their sequence in the text. References should be made in the text to each figure. Each figure should have a suitable caption.

Tables:
Authors should take note of the limitations set by the size and layout of the journal. Table should not exceed the printed area of the page. They should be typed on separate sheets and details about the tables should be given in the text. Heading should be brief. Large tables should be avoided and may be provided as supplementary information, if required.

Equations:
Equations should be numbered sequentially with Arabic numerals and cited in the text. Subscripts and Superscripts should be set off clearly. Equation writing software that presents each equation as an object in MS Word will be accepted. Style and convention adopted for the equations should be uniform throughout the paper.

References:
All references to publications cited in the main text should be presented as a list of references in order following the text and all references in the list must be cited in the text. References should be arranged chronologically, in the text. The list of references should be arranged alphabetically at the end of the paper.

References should be given in the following form:
Kaila, K.L., Reddy P.R., Mall D.M., Venkateswarlu, N., Krishna V.G. and Prasad, A.S.S.S.R.S., 1992. Crustal structure of the west Bengal Basin from deep seismic sounding investigations. Geophys. J. Int., 111,45-66.

REVIEW PROCESS:

All manuscripts submitted to the journal are peer-reviewed. It is advisable to send the contact details of 4 potential reviewers along with the manuscript to expedite the review process. Editor has the option to select reviewers from the list or choose different reviewers. The review process usually takes about 3 months. All enquiries regarding the manuscript may be addressed to the Editor.

GALLEY PROOF:

Technical editing of manuscripts is performed by the editorial board. The author is asked to check the galley proof for typographical errors and to answer queries from the editor. Authors are requested to return the corrected proof within two days of its receipt to ensure uninterrupted processing. The editor will not accept new material in proof unless permission from the editorial board has been obtained for the addition of a "note added in proof". Authors are liable for the cost of excessive alterations to galley proof.

PUBLICATION CHARGES:

There are no page charges for publication and printing charges for b/w figures. However, in view of substantial cost involved in printing of color figures, author will be charged for printing of pages containing color figures @ Rs. 2,500/- per page. The charges may be revised at any time based on cost of printing and production. Author will receive an estimate/ invoice of the color figures reproduction cost along with the galley proof. It is the responsibility of the author to remit the color figures reproduction cost within one month of the receipt of the estimate/invoice.

The corresponding author will receive a soft copy (pdf format) of his/her published article. Should the author desire to purchase reprints of his/her publication, he/she must send the duly signed Reprint Order Form (accompanies the galley proof and contains price details) along with the corrected galley proof to the Editor. The reprint charges must be paid within one month of sending the Reprint Order Form.

Any payment related to printing of color figures and/or purchase of reprints should be made in the form of a Demand Draft in the name of Treasurer, Indian Geophysical Union, payable at Hyderabad.

You may download the pdf file from: http://www.j-igu.in/IGU-Guide-forAuthors.pdf